COLLEGE MATHS, TELECOMS
DOCTORAL INFORMATIQUE, SIGNAL
BRETAGNE SYSTEMES, ELECTRONIQUE

Université de Rennes

THÈSE DE DOCTORAT DE

L'UNIVERSITÉ DE RENNES

ÉCOLE DOCTORALE N° 601
Mathématiques, Télécommunications, Informatique, Signal, Systèmes, Électronique
Spécialité : *Informatique*

Par

Constance BOCQUILLON

Optimisation des paramètres d'acquisition en IRM de diffusion pour la reconstruction de la connectivité cérébrale

Thèse présentée et soutenue à Rennes, le 30 Juin 2026
Unité de recherche : IRISA

Rapporteurs avant soutenance :

Jing-Rebecca LI — Directrice de recherche, ENSTA Paris, France
Cyril POUPON — Directeur de recherche, CEA Neurospin, France

Composition du Jury :

Président :	Pierre MAUREL	Professeur des universités, Université de Rennes, Rennes, France
Examinateurs :	Alessandro DADUCCI	Assistant Professor, University of Verona, Italy
	Jing-Rebecca LI	Directrice de recherche, ENSTA Paris, France
	Cyril POUPON	Directeur de recherche, CEA Neurospin, France
	François ROUSSEAU	Professeur des universités, IMT Atlantique, Brest, France
	Chantal TAX	Assistant Professor, UMC Utrecht, Netherlands

Invité(s) :

Emmanuel CARUYER — Chargé de recherche, CNRS, HDR, Rennes, France (directeur de thèse)
Isabelle COROUGE — Ingénieure de recherche, Université de Rennes, Rennes, France (co-encadrante de thèse)

Acknowledgement

Je tiens à remercier toutes les personnes qui m'ont soutenue, de près ou de loin, pendant cette thèse.

Je tiens tout particulièrement à remercier Emmanuel et Isabelle pour leur accompagnement tout au long de ces années, bien avant même le début de cette thèse. Merci pour la confiance que vous m'avez accordée, pour votre disponibilité et pour votre soutien sans faille. J'ai énormément appris à vos côtés, tant sur le plan scientifique que dans ma façon d'aborder la recherche. Merci pour les discussions, les conseils, les encouragements et la bienveillance dont vous avez toujours fait preuve. Votre présence a joué un rôle essentiel dans ce parcours, et je mesure aujourd'hui la chance que j'ai eue d'être encadrée par vous.

J'adresse également toute ma reconnaissance à l'équipe Empenn pour avoir contribué à une ambiance de travail chaleureuse. Merci pour les discussions scientifiques ainsi que pour tous les moments de convivialité qui ont rythmé ces années de doctorat. Votre présence a largement contribué à rendre cette expérience aussi stimulante qu'agréable.

Je souhaite aussi remercier l'ensemble du personnel de l'IRISA qui m'a accompagnée au cours de cette thèse, qu'il s'agisse des aspects administratifs, des activités d'enseignement ou du soutien scientifique.

Je souhaite également remercier les équipes du LTS5 à l'EPFL et de DICE à l'Université de Vérone. Les collaborations développées avec vous ont été parmi les aspects les plus enrichissants de cette thèse. Merci pour votre accueil, votre disponibilité, votre bienveillance et les nombreux échanges scientifiques que nous avons partagés. Qu'il s'agisse de la relation initiée lors de mon stage à l'EPFL en 2021 puis poursuivie au cours de mon doctorat, ou de mon séjour en Italie en 2024, chacune de ces expériences m'a beaucoup apporté et a contribué à faire de cette thèse une aventure scientifique et humaine particulièrement enrichissante.

Je tiens aussi à remercier tous les chercheurs que j'ai pu rencontrer durant ces années de thèse pour nos échanges enrichissants, que ce soit lors des conférences ou en dehors. Je tiens également à remercier les membres du jury d'avoir accepté d'évaluer ce travail. Je suis honorée du temps et de l'attention que vous lui avez consacrés.

Enfin, je remercie profondément ma famille pour son soutien indéfectible malgré la

distance. Merci pour votre patience et vos encouragements, même dans les périodes les plus difficiles. Votre soutien a été une source de motivation tout au long de ce parcours.

À toutes celles et ceux qui ont contribué, directement ou indirectement, à cette aventure scientifique et humaine, j'adresse mes plus sincères remerciements.

Table of Contents

Résumé en français **9**

I Introduction 15

Introduction **17**

II Background 23

1 Principles of diffusion MRI **25**

1.1 Brownian motion and diffusion 25
1.2 MRI signal and diffusion encoding 28
1.2.1 The spin-echo sequence 28
1.2.2 The PGSE sequence 28
1.3 Artifacts and noise in dMRI 30
1.3.1 Signal to Noise Ratio in diffusion MRI 30
1.3.2 Common artifacts 31
1.4 Conclusion 32

2 Modeling white matter microstructure **35**

2.1 Brain microstructure 36
2.2 Mathematical models 39
2.2.1 Diffusion Tensor Imaging (DTI) 39
2.2.2 Diffusion Kurtosis Imaging (DKI) 41
2.2.3 Diffusion Tensor Distribution (DTD) 42
2.2.4 Mean Apparent Propagator MRI (MAPMRI) 50
2.3 Biophysical models 51
2.3.1 CHARMED: Composite hindered and restricted model of diffusion . 52
2.3.2 AxCaliber/ActiveAx 53
2.3.3 The Stick-Zeppelin-Ball model 53

2.3.4 NODDI: Neurite Orientation Dispersion and Density Imaging . . . 55
2.4 Advantages and limitations of mathematical and biophysical models 56
2.5 Signal simulation 56
2.6 Digital phantoms and mesh models 57
2.7 Grey matter microstructure models 60
2.8 Conclusion 61

3 Acquisition strategies 63
3.1 Diffusion gradient direction selection 64
3.2 Diffusion weighting and acquisition parameters 64
3.3 Advanced diffusion encoding 67
3.3.1 Generalized gradient waveforms 67
3.3.2 Multidimensional diffusion encoding 68
3.3.3 Q-space trajectory imaging (QTI) and b-tensor encoded acquisition 69
3.4 Protocol optimization strategies 74
3.4.1 Cramér-Rao lower bound (CRLB)-based optimization 74
3.4.2 Dictionary-based optimization 74
3.4.3 Machine learning-based approaches 75
3.5 Conclusion 75

4 Structural connectivity and tractography 77
4.1 Brain connectivity 78
4.2 Orientation Distribution Function (ODF) 79
4.3 Tractography algorithms 80
4.4 Filtering 82
4.5 Improving tractography using multidimensional dMRI 84
4.6 Conclusion 84

III Contributions 87

5 Optimization of acquisition schemes towards a better estimation of the microstructure parameters 89
5.1 Methods 90
5.1.1 Acquisition superset 90
5.1.2 Fingerprinting the parameter space 90

5.1.3 Selection of acquisition schemes . . . 93
5.1.4 Parameter estimation . . . 93
5.2 Results . . . 95
5.3 Extensions . . . 97
5.3.1 Adapting the number of directions in the superset . . . 99
5.3.2 Exploring another metric to discriminate between DTDs . . . 102
5.4 Discussion and conclusion . . . 106

6 Linking Diffusion Tensor Distribution (DTD) parameters with microstructure information 109
6.1 Methods . . . 110
6.1.1 Substrate generation . . . 110
6.1.2 Estimation of a ground truth orientation parameter from the substrate 111
6.1.3 Monte-Carlo simulations . . . 112
6.2 Results and discussion . . . 114
6.3 Conclusion . . . 116

7 Multidimensional dMRI on tractography 119
7.1 Generation of numerical phantoms and their associated signals: Phantomas 120
7.2 Adapting AMICO and COMMIT to b-tensor encoded acquisitions . . . 122
7.3 Testing b-tensor encoded acquisition for tractography filtering . . . 123
7.4 Discussion and conclusion . . . 124

IV Conclusion 127

Conclusion 129

Publications 133

List of Figures 135

Bibliography 141

Résumé en français

Contexte

L'imagerie par résonance magnétique (IRM) est une technique non invasive largement utilisée en clinique et en recherche pour visualiser les structures internes du corps humain, en particulier les tissus mous. Parmi les différentes modalités d'IRM, l'IRM de diffusion (IRMd) (Le Bihan and Breton 1985; Merboldt, Hanicke, and Frahm 1985) permet de sonder indirectement la microstructure des tissus en mesurant le déplacement des molécules d'eau. Cette propriété en fait un outil particulièrement pertinent pour l'étude du cerveau. Une des applications phare de l'IRM de diffusion s'appelle *tractographie*, elle vise à reconstruire la trajectoires des fibres nerveuses de la matière blanche, et par là-même permet l'étude de la connectivité cérébrale. À l'échelle microscopique, les molécules d'eau sont en mouvement permanent sous l'effet de l'agitation thermique, ce phénomène est connu sous le nom de mouvement brownien (Brown 1828; Einstein 1905). Dans un milieu sans contrainte et homogène, ce mouvement est aléatoire et isotrope. Cependant, dans les tissus biologiques, la présence de membranes, de fibres, de vaisseaux sanguins et d'autres structures crée un environement hétérogène qui restreint ou entrave ce mouvement. Ainsi, la diffusion des molécules d'eau devient dépendante de la microstructure locale, ce qui permet à l'IRM de diffusion de fournir des informations sur l'organisation des tissus, leur densité ou encore leur orientation.

Le principe de l'IRM de diffusion repose sur la sensibilité du signal IRM aux déplacements des spins nucléaires lorsqu'ils sont soumis à des gradients de champ magnétique. En introduisant des gradients de diffusion au sein des séquences IRM, il est possible d'encoder le déplacement des molécules d'eau dans le signal mesuré. Ce processus se traduit par une atténuation du signal dont l'amplitude dépend de l'intensité de la diffusion dans la direction du gradient appliqué. L'utilisation de plusieurs gradients permet ainsi de caractériser la diffusion dans l'espace en trois dimension et de mettre en évidence des propriétés telles que l'anisotropie de la diffusion, particulièrement marquées dans les faisceaux de fibres de la matière blanche.

Historiquement, les premières approches en IRM de diffusion se sont appuyées sur des

schémas d'acquisition relativement simples resposant sur des gradients appliqués selon une seule direction à la fois et sur un nombre limité de valeurs de pondération en diffusion, généralement caractérisées par le paramètre appelé *b-value*. Ces acquisitions ont permis le développement de modèles largement utilisés tels que le tenseur de diffusion (DTI) (P. Basser, Mattiello, and LeBihan 1994; Le Bihan and Breton 1985), qui fournit une description gaussienne de la diffusion et permet d'extraire des métriques comme l'anisotropie ou la diffusivité moyenne. Cependant, ces approches présentent des limitations importantes. En particulier, elles reposent sur des hypothèses simplificatrices qui ne sont pas toujours vraies dans les tissus biologiques, notamment en présence de géométries complexes comme les croisements de fibres ou la présence de plusieurs compartiments. De plus, la description de la diffusion par un simple tenseur ne permet pas de capturer toute la richesse des phénomènes microscopiques sous-jacents. Ces limitations ont motivé le développement de schémas d'acquisition plus avancés visant à enrichir l'information contenue dans le signal. Dans le reste de la thèse, nous utiliserons indifférement schéma d'acquisition, protocole d'acquisition ou acquisition pondérées en diffusion pour décrire l'ensemble des gradients de diffusion appliqués afin d'obtenir les signaux IRM.

Parmi ces différents développements se trouvent les acquisitions multi-shell qui combinent plusieurs b-valeurs et qui permettent d'échantillonner la diffusion à plusieurs échelles. Elles permettent donc d'utiliser des modèles plus complexes tels que le kurtosis de diffusion (Jensen, Helpern, et al. 2005) ainsi que les modèles multi-compartiments (Assaf and P. J. Basser 2005; Scherrer et al. 2016; Assaf, Blumenfeld-Katzir, et al. 2008; Zhang et al. 2012). Des encodages multidimensionnels ont aussi été proposés. Ils permettent d'introduire des schémas d'encodage plus riches que les gradients linéaires utilisés jusque là. Ces techniques incluent notamment les encodages à l'aide de tenseur de diffusion (b-tenseurs) (C.-F. Westin, Szczepankiewicz, et al. 2014; C.-F. Westin, Hans Knutsson, et al. 2016) ainsi que les acquisitions à double ou triple encodages (DDE, TDE) (Cory 1990; Jensen and Helpern 2018). Ces techniques permettent notamment de sonder des propriétés de la microstructure jusque-là inatteignables telles que l'anisotropie microscopique.

Si ces approches offrent un potentiel accru pour la caractérisation des tissus, elles posent également de nouveaux défis en terme de conception des schémas d'acquisition. En effet, le choix des paramètres d'acquisition (directions des gradients, valeurs de b, formes de gradients, temps de diffusion, temps d'écho) influence directement la sensibilité du signal aux propriétés de la microstructure. Par ailleurs, des contraintes pratiques importantes doivent être prises en compte. Le temps d'acquisition est limité, en particulier

en contexte clinique, ce qui impose des restrictions sur le nombre de mesures. Les limitations matérielles des systèmes IRM telles que l'amplitude maximale des gradients ou leur vitesse de commutation restreignent également l'espace des acquisitions possibles.

Dans ce contexte, la conception d'un protocole d'acquisition ne peut pas être dissociée des objectifs de l'étude ni des modèles utilisés pour l'analyse. L'optimisation des schémas d'acquisition est devenue un enjeu central en IRM de diffusion, il s'agit de concevoir des protocoles capables de maximiser l'information pertinente contenue dans le signal tout en respectant les contraintes expérimentales.

Structure du manuscript

Le manuscript est divisé en deux grande parties. La première partie est composée des chapitres 1, 2, 3 et 4. Elle permet de poser les éléments de contexte de la thèse. Ils permettent notamment d'aborder quelques notions de base de l'IRM de diffusion, des modèles de microstructure, des schémas d'acquisition ainsi que de la tractographie. Dans la seconde partie, composée des chapitres 5, 6 et 7, nous détaillons les trois principales contributions de la thèse.

Chapitre 1 : Ce chapitre permet d'introduire les principes fondamentaux de l'IRM de diffusion. Dans un premier temps, nous présentons le mouvement brownien et son rôle dans les tissus biologiques ainsi que sur la manière dont l'IRM de diffusion permet d'en extraire des informations microstructurelles. Nous contextualisons ensuite le lien entre le signal IRM et l'encodage de la diffusion en décrivant comment les gradients du champ magnétique permettent de rendre sensible le signal aux déplacements des molécules d'eau. Enfin, nous abordons les aspects pratiques liés à l'acquisition en particulier le rapport signal à bruit et les principaux artefacts qui influencent la qualité des données et leur interprétation.

Chapitre 2 : Ce chapitre est consacré aux modèles utilisés en IRM de diffusion pour relier le signal mesuré aux propriétés microstructurelles des tissus. Nous présentons dans un premier temps les modèles fondés sur des représentations mathématiques du signal suivis des modèles biologiques qui introduisent des hypothèses sur l'organisation des tissus. Nous discutons ensuite des avantages et des limites de ces différentes approches. Dans un second temps, nous abordons les outils nécessaires à l'étude et la validation de ces modèles en introduisant les méthodes de simulation du signal ainsi que l'utilisation de fantômes numériques et de modèles géométriques. Enfin, nous ouvrons sur les développe-

ments récents autour de la caractérisation de la microstructure dans la matière grise.

Chapitre 3 : Ce chapitre est consacré aux schémas d'acquisition en IRM de diffusion et à leur rôle dans la caractérisation de la microstructure des tissus. Nous présentons dans un premier temps les principes de sélection des directions de gradients, en considérant les acquisitions mono et multi-shell, afin d'assurer un échantillonnage angulaire adapté. Nous nous intéressons ensuite au choix des autres paramètres d'acquisition tels que les valeurs de b, les temps de diffusion ou encore les temps d'écho, qui conditionnent la sensibilité du signal aux propriétés microstructurales. Enfin, nous introduisons les stratégies d'optimisation des protocoles d'acquisition visant à concilier la richesse de l'information et les contraintes pratiques notamment en terme de temps d'acquisition.

Chapitre 4 : Ce chapitre est focalisé sur la tractographie. Pour commencer, nous présentons la connectivité cérébrale. Nous décrivons ensuite les différentes étapes de la tractographie en commençant par l'estimation des fonctions de distribution d'orientation des fibres (fODF) qui permettent de caractériser les directions de diffusion au sein de chaque voxel. Ces informations sont ensuite utilisées pour reconstruire les trajectoires des faisceaux de fibres. Nous présentons ensuite les principales familles d'algorithmes de tractographie. Étant donné que la tractographie génère de nombreux faux positifs, nous avons décrit les méthodes de filtrages de tractogrammes. Enfin, nous discutons des apports récents de l'IRM de diffusion multidimensionnelle sur la tractographie.

Chapitre 5 : Dans ce chapitre est présentée la première contribution de cette thèse, qui porte sur la sélection de schémas d'acquisitions optimisés pour l'estimation des paramètres d'intérêt d'un modèle donné, ici les distributions de tenseurs de diffusion (DTD). Pour faire cela, nous avons créé un cadre dans lequel on choisit un ensemble de b-tenseurs, correspondant chacun à une mesure, nous avons utilisé pour chaque tenseur un ensemble de directions. Cela forme un ensemble dans lequel nous sélectionnons les acquisitions finales. Nous avons ensuite généré une partition de l'espace des paramètres de notre modèle (ici les DTD) en fonction de la précision atteignable. En utilisant ces modèles pour nos colonnes et les acquisitions pour les lignes, nous avons généré un dictionnaire de signaux que nous avons utilisé pour sélectionner les acquisitions qui permettent au mieux de distinguer parmi les modèles. Nous avons présenté une première partie de résultats avant de discuter d'améliorations possibles, par exemple en changeant le nombre de directions sélectionnées ou encore en changeant la métrique utilisée pour distinguer les modèles afin d'améliorer les résultats obtenus. Nous avons donc montré les résultats obtenus en utilisant ces modifications avant de conclure sur d'autres pistes d'améliorations et de discussion.

Chapitre 6 : Étant donné que les modèles comme la distribution de tenseurs de diffusion (DTD) reposent sur une représentation mathématique du signal de diffusion, il est parfois complexe de traduire les paramètres de ces modèles en terme de microstructure. Afin de mieux comprendre ces liens, nous avons étudié dans ce chapitre le lien entre le paramètre de dispersion d'orientation dans les DTD et la dispersion angulaire de nos substrats numériques. Pour cela, nous avons utilisé des simulations de Monte-Carlo (Rafael-Patino et al. 2020) dans des substrats numériques de matière blanche généré avec CACTUS (Villarreal-Haro et al. 2023).

Chapitre 7 : Dans ce chapitre, nous abordons le developpement d'une modification de Phantomas (Caruyer, Daducci, et al. 2014), qui génère des fantômes numériques pour la validation, afin de pouvoir générer des fantômes numériques qui correspondent plus à ce qui est attendu pour pouvoir tester l'impact de b-tenseurs sur la tractographie. Plus particulièrement, nous avons ajouté des changements de densité dans le substrat ainsi que la possibilité d'avoir des faisceaux de fibres dont le diamètre varie. Nous avons ensuite implémenté les outils nécessaires pour tester les b-tenseurs dans COMMIT (Daducci, Dal Palù, et al. 2015). Nous pouvons maintenant tester plus en détails les effets des acquisitions encodées par des b-tenseurs sur le filtrage de tractogramme.

Conclusion : Finalement, nous rappelons les trois contributions de la thèse et discutons de leurs relations. Ces différentes contributions s'inscrivent dans l'étude des b-tenseurs et de leur impact en IRM de diffusion, que ce soit sur le choix du schéma d'acquisition utilisé, ou sur l'application de la tractographie. Nous avons aussi étudié le lien entre un paramètre du modèle de la distribution de tenseurs et de sa signification physique sur la microstructure. Nous profitons également de cette conclusion pour évoquer des perspectives, des futurs travaux ainsi que des pistes de réflexion pour continuer ce travail en dehors de cette thèse.

Part I

Introduction

INTRODUCTION

Context

Magnetic resonance imaging (MRI) is a non-invasive technique widely used in clinical practice and research to visualize the internal structures of the human body, particularly soft tissues. Among the different MRI modalities, diffusion MRI (dMRI) (Le Bihan and Breton 1985; Merboldt, Hanicke, and Frahm 1985) enables indirect probing of tissue microstructure by measuring the displacement of water molecules. This property makes it a particularly relevant tool for studying the brain. One of the flagship applications of diffusion MRI is *tractography*, which aims to reconstruct the trajectories of white matter nerve fibers, thereby enabling the study of brain connectivity. At the microscopic scale, water molecules are in constant motion due to thermal agitation; this phenomenon is known as Brownian motion (Brown 1828; Einstein 1905). In a homogeneous and unconstrained environment, this motion is random and isotropic. However, in biological tissues, the presence of membranes, fibers, blood vessels, and other structures creates a heterogeneous environment that restricts or hinders this motion. As a result, water diffusion becomes dependent on the local microstructure, allowing diffusion MRI to provide information about tissue organization, density, and orientation.

The principle of diffusion MRI relies on the sensitivity of the MRI signal to the displacement of nuclear spins when subjected to magnetic field gradients. By introducing diffusion gradients into MRI sequences, it is possible to encode the displacement of water molecules into the measured signal. This results in signal attenuation whose magnitude depends on the intensity of diffusion in the direction of the applied gradient. Using multiple gradients allows diffusion to be characterized in three-dimensional space and highlights properties such as diffusion anisotropy, which is particularly pronounced in white matter fiber bundles.

Historically, early approaches in diffusion MRI relied on relatively simple acquisition schemes based on gradients applied in a single direction at a time and a limited number of diffusion weightings, typically characterized by the parameter known as the b-value. These acquisitions enabled the development of widely used models such as diffusion tensor

imaging (DTI) (P. Basser, Mattiello, and LeBihan 1994; Le Bihan and Breton 1985), which provides a Gaussian description of diffusion and allows extraction of metrics such as anisotropy or mean diffusivity. However, these approaches have significant limitations. In particular, they rely on simplifying assumptions that are not always valid in biological tissues, especially in the presence of complex geometries such as fiber crossings or multiple compartments. Moreover, describing diffusion with a single tensor does not capture the full richness of the underlying microscopic phenomena. These limitations have motivated the development of more advanced acquisition schemes aimed at enriching the information contained in the signal. Throughout the rest of this thesis, we will use the terms acquisition scheme, acquisition protocol, or diffusion-weighted acquisition interchangeably to describe the set of diffusion gradients applied to obtain MRI signals.

Among these developments are multi-shell acquisitions, which combine multiple b-values and enable sampling diffusion at different scales. These approaches allow the use of more complex models such as diffusion kurtosis (Jensen, Helpern, et al. 2005) and multi-compartment models (Assaf and P. J. Basser 2005; Scherrer et al. 2016; Assaf, Blumenfeld-Katzir, et al. 2008; Zhang et al. 2012). Multidimensional encoding schemes have also been proposed, enabling richer encoding strategies than the previously used linear gradients. These techniques include diffusion tensor encoding (b-tensors) (C.-F. Westin, Szczepankiewicz, et al. 2014; C.-F. Westin, Hans Knutsson, et al. 2016) as well as double or triple diffusion encoding (DDE, TDE) (Cory 1990; Jensen and Helpern 2018). These methods make it possible to probe microstructural properties that were previously inaccessible, such as microscopic anisotropy.

While these approaches offer increased potential for tissue characterization, they also introduce new challenges in designing acquisition schemes. Indeed, the choice of acquisition parameters (gradient directions, b-values, gradient shapes, diffusion times, echo times) directly influences the sensitivity of the signal to microstructural properties. Additionally, important practical constraints must be considered. Acquisition time is limited, especially in clinical settings, which restricts the number of measurements. Hardware limitations of MRI systems, such as maximum gradient amplitude and slew rate, also constrain the space of feasible acquisitions.

In this context, the design of an acquisition protocol cannot be separated from the objectives of the study or the models used for analysis. Optimizing acquisition schemes has become a central issue in diffusion MRI: the goal is to design protocols that maximize the relevant information contained in the signal while respecting experimental constraints.

Structure of the manuscript

The manuscript is divided into two main parts. The first part consists of Chapters 1, 2, 3, and 4, which establish the background of the thesis. These chapters cover fundamental concepts in diffusion MRI, microstructure models, acquisition schemes, and tractography. The second part, composed of Chapters 5, 6, and 7, details the three main contributions of the thesis.

Chapter 1: This chapter introduces the fundamental principles of diffusion MRI. It begins by presenting Brownian motion and its role in biological tissues, as well as how diffusion MRI can extract microstructural information from it. It then contextualizes the relationship between the MRI signal and diffusion encoding by describing how magnetic field gradients make the signal sensitive to water molecule displacement. Finally, practical aspects of acquisition are discussed, including signal-to-noise ratio and the main artifacts affecting data quality and interpretation.

Chapter 2 : This chapter focuses on models used in diffusion MRI to relate measured signals to tissue microstructure. It first presents signal-based mathematical models, followed by biological models that incorporate assumptions about tissue organization. The advantages and limitations of these approaches are then discussed. The chapter also introduces tools for studying and validating these models, including signal simulations, digital phantoms, and geometric models. Finally, it opens on recent developments in characterizing gray matter microstructure.

Chapter 3 : This chapter is dedicated to acquisition schemes in diffusion MRI and their role in characterizing tissue microstructure. It first presents principles for selecting gradient directions, considering both single-shell and multi-shell acquisitions to ensure adequate angular sampling. It then examines other acquisition parameters such as b-values, diffusion times, and echo times, which determine sensitivity to microstructural properties. Finally, it introduces optimization strategies for acquisition protocols aimed at balancing information richness with practical constraints, particularly acquisition time.

Chapter 4 : This chapter focuses on tractography. It begins with an overview of brain connectivity, followed by a description of the different steps in tractography, starting with the estimation of fiber orientation distribution functions (fODFs), which characterize diffusion directions within each voxel. These are then used to reconstruct fiber bundle trajectories. The main families of tractography algorithms are presented. Given that tractography produces many false positives, tractogram filtering methods are also

described. Finally, recent contributions of multidimensional diffusion MRI to tractography are discussed.

Chapter 5 : This chapter presents the first contribution of the thesis, which focuses on selecting optimized acquisition schemes for estimating parameters of interest in a given model, here diffusion tensor distributions (DTD). To achieve this, a framework was developed in which a set of b-tensors, each corresponding to a measurement, is defined, and a set of directions is used for each tensor. This forms a pool from which the final acquisitions are selected. A partition of the model parameter space (here DTDs) was then generated based on achievable precision. Using models as columns and acquisitions as rows, a signal dictionary was constructed to select acquisitions that best distinguish between models. Initial results are presented, followed by a discussion of possible improvements, such as modifying the number of selected directions or changing the metric used to distinguish models. Results obtained with these modifications are then shown, and further directions for improvement are discussed.

Chapter 6 : Since models such as diffusion tensor distributions (DTD) rely on mathematical representations of the diffusion signal, translating their parameters into microstructural meaning can be challenging. To better understand these relationships, this chapter investigates the link between the orientation dispersion parameter in DTDs and the angular dispersion of numerical substrates. Monte Carlo simulations (Rafael-Patino et al. 2020) were performed in digital white matter substrates generated with CACTUS (Villarreal-Haro et al. 2023).

Chapter 7 : This chapter presents the development of a modification of Phantomas (Caruyer, Daducci, et al. 2014), a tool used to generate digital phantoms for validation. The goal was to create phantoms better suited for studying the impact of b-tensor encoding on tractography. Specifically, variations in substrate density and fiber bundle diameter were introduced. The necessary tools were then implemented to test b-tensors within COMMIT (Daducci, Dal Palù, et al. 2015). This now enables more detailed investigation of the effects of b-tensor-encoded acquisitions on tractogram filtering.

Conclusion : Finally, the three main contributions of the thesis are summarized and their relationships discussed. These contributions all relate to the study of b-tensors and their impact in diffusion MRI, whether in acquisition design or tractography applications. The relationship between a model parameter of diffusion tensor distributions and its physical interpretation in terms of microstructure is also examined. The conclusion also outlines future perspectives and directions for continuing this work beyond the scope of

the thesis.

Part II

Background

Chapter 1

Principles of diffusion MRI

Magnetic resonance imaging (MRI) is a widely used non-invasive imaging technique that provides detailed images of the anatomy. It is commonly employed in clinical setting to detect and monitor a variety of conditions such as tumors, some traumatic injuries or neurodegenerative diseases. While MRI provides high-quality images, it conventionally describes tissues at the millimeter level and may not fully capture the tissue microstructure. To gain additional insight, other modalities of MRI can be used as diffusion MRI (dMRI). In dMRI, the motion of water molecules within the tissue is measured (Johansen-Berg and T. E. Behrens 2009; D. K. Jones 2010). This provides indirect information about cellular structures like membranes and fibers. More generally, diffusion MRI aims to extract parameters from the signal enabling a more precise characterization of tissues properties at the microscopic scale.

In this chapter, we first describe the physical basis of diffusion, including the motion of water molecules in free and restricted environments. We then introduce the spin-echo sequence and explain how diffusion sensitization is achieved. Finally, we discuss noise and common artifacts that affect diffusion MRI data.

1.1 Brownian motion and diffusion

9 In 1827, the botanist Robert Brown reported a random displacement of pollen suspended in water without apparent cause (Brown 1828) (see Figure 1.1). While Einstein was aiming to prove the existence of atoms, he provided an explanation for Brown's observations, later called *Brownian motion* in 1905 (Einstein 1905).

Brownian motion refers to the random movement of particles resulting from collisions with surrounding molecules. At temperatures above absolute zero, water molecules constantly move in the medium. The collective effect of this random microscopic motion leads to *diffusion*, which describes how particles spread over time.

If the molecules are not restricted by any obstacle, this Brownian motion can be

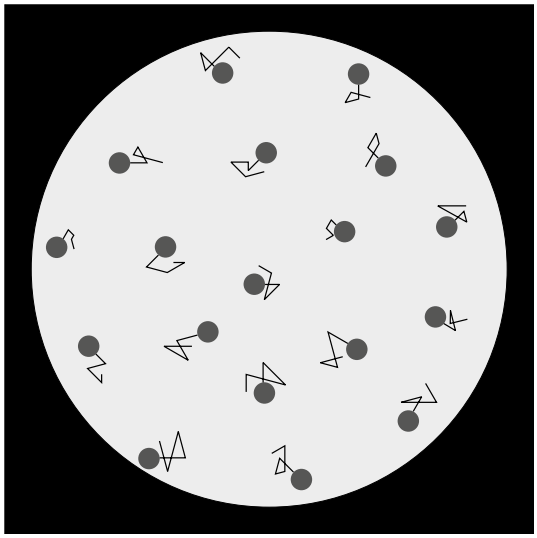

Figure 1.1 – Displacement of pollen particles suspended in water. Illustration extracted from (Johansen-Berg and T. E. Behrens 2009).

quantified by the mean squared displacement:

$$\langle r^2(t) \rangle = 2nDt \tag{1.1}$$

where r is the displacement, $n = 3$ is the spatial dimension, D is the diffusion coefficient (for pure water at body temperature, D is approximately 3.0×10^{-3} mm^2/s) and t is the diffusion time.

In biological tissues, diffusion is strongly influenced by the microstructure. The brain is composed of neurons, glial cells, blood vessels, extracellular matrix and cerebrospinal fluid (CSF). Depending on the environment, different diffusion regimes can be identified:

— **Free diffusion**: occurs in regions such as CSF, where molecules move without any restriction. In this case, the mean squared displacement $\langle r^2(t) \rangle$ increases linearly with time, following a Gaussian distribution.

— **Restricted diffusion**: occurs within bounded structures such as axons, where membranes trap molecules (Assaf and P. J. Basser 2005). Here, $\langle r^2(t) \rangle$ initially increases with time but progressively deviates from linearity and may reach a plateau as molecules are confined within a limited space.

— **Hindered diffusion**: occurs in the extra-cellular space, where surrounding structures slow down molecules without confining them. In this case, $\langle r^2(t) \rangle$ remains

approximately linear with time but the apparent diffusion coefficient (ADC) is reduced compared to free diffusion.

It is important to note that whenever the membranes are permeable, some exchange is possible between compartments, which further complicates the description of diffusion in biological tissues. The diffusion in diverse microscopic environments is shown in Figure 1.2.

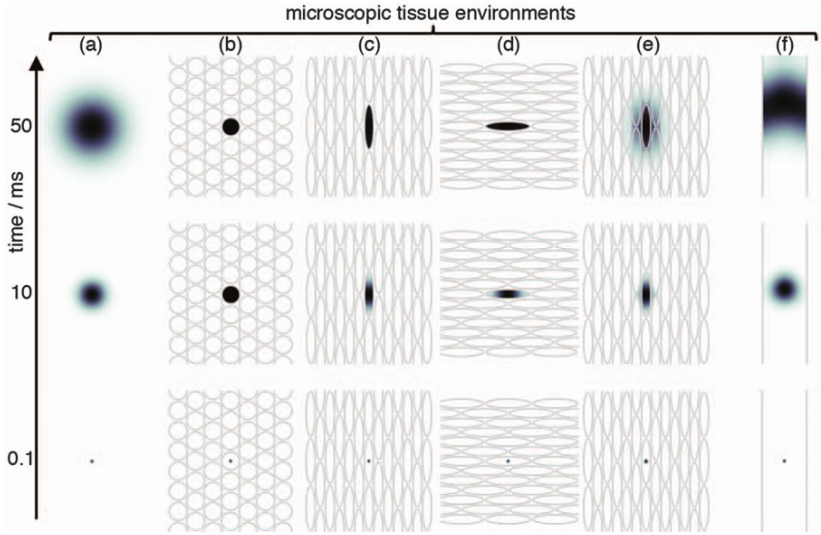

Figure 1.2 – Diffusion in free water (a) and in different plausible microscopic environments over time. (e) shows an example of diffusion in tissue where membranes are permeable. Figures from (Topgaard 2020).

In diffusion MRI, these effects are observed over diffusion times typically ranging from a few tens to several hundreds of milliseconds, during which water molecules travel distances comparable to cellular dimensions. At short diffusion time, the displacement distribution is often approximated as Gaussian, however, as diffusion time increases and interactions with structural barriers become more significant, deviations from this ideal behaviour are emerging.

Depending on the organization of the tissue, diffusion can be either *isotropic* or *anisotropic*. In isotropic environments such as CSF, diffusion is identical in all directions. In contrast, in structured tissues like white matter, diffusion is anisotropic as it is facilitated along fiber directions and restricted in the perpendicular directions.

1.2 MRI signal and diffusion encoding

The magnetization dynamics are generally described by the Bloch equations (Bloch 1946), which account for precession and relaxation. For diffusion MRI, Torrey extended these equations to include molecular motion, yielding the Bloch-Torrey equations (Torrey 1956). This introduces a diffusion term that accounts for the random motion of spins in the presence of gradients. This makes the MR signal sensitive to both relaxation and molecular motion, which underlies the principle of diffusion-weighted imaging.

1.2.1 The spin-echo sequence

The study of diffusion in MRI has its roots in spin-echo experiments. In 1950, Hahn showed that after excitation of water molecules, the MR signal decays due to dephasing of spins caused by magnetic field inhomogeneities (Hahn 1950). To compensate for this effect, the spin-echo sequence was introduced, in which a 90° RF pulse is followed by a 180° refocusing pulse at time $t = \frac{TE}{2}$. This second pulse reverses the phase dispersion of spins caused by static field inhomogeneities, leading to the formation of an echo at time $t = TE$. Carr and Purcell later provided a formal description of this sequence (Carr and Purcell 1954). A schematic representation is shown in Figure 1.3.

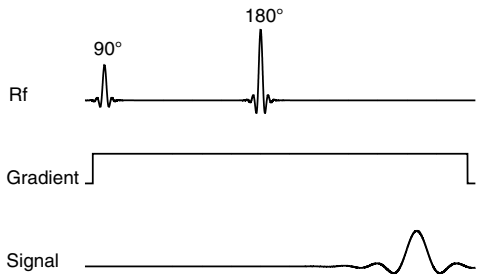

Figure 1.3 – Schematic representation of a spin-echo sequence presented by Carr and Purcell. Figure from Johansen-Berg and T. E. Behrens (2009)

.

1.2.2 The PGSE sequence

Stejskal and Tanner introduced the pulsed gradient spin-echo (PGSE) squence in 1965 (Stejskal and Tanner 1965), which explicitly sensitizes the MR signal to diffusion. As

shown in Figure 1.4, two diffusion-sensitizing gradients are applied symmetrically around the refocusing pulse. The first gradient encodes the positions of spins along the direction of the gradient, while the second attempts to refocus them. If spins move between the two gradients due to diffusion, the refocusing is incomplete, producing a measurable signal attenuation that reflects water molecules displacement along the direction of the gradient.

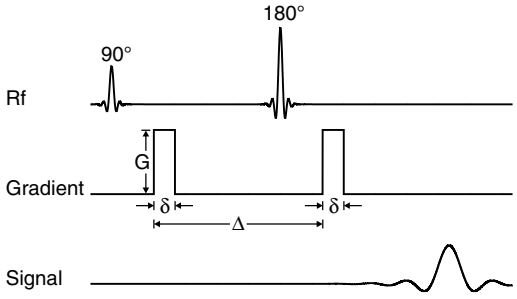

Figure 1.4 – Schematic representation of a pulsed gradient spin-echo sequence presented by Stejskal and Tanner. Figure from Johansen-Berg and T. E. Behrens (2009).

In the case of an isotropic Gaussian diffusion, the resulting diffusion-weighted signal is well described using the Stejskal-Tanner equation:

$$S(b) = S_0 \exp(-bD) \tag{1.2}$$

where S_0 is the signal without diffusion weighting, D is the apparent diffusion coefficient (ADC) and b is the *b-value*, a diffusion weighting factor, defined as:

$$b = \gamma^2 G^2 \delta^2 (\Delta - \frac{\delta}{3}) \tag{1.3}$$

where G is the gradient amplitude, δ is the duration of the gradient pulse, Δ is the time between the two gradients and γ is the gyromagnetic ratio. The b-value encodes the sensitivity of the sequence to diffusion: larger values increase sensitivity but reduce the signal-to-noise ratio. Typical clinical values range from 0 to 1000 $\mathrm{s\,mm^{-2}}$, while research studies may use up to several thousand $\mathrm{s\,mm^{-2}}$.

Diffusion gradients can be applied along multiple directions to capture the anisotropy of molecular motion. In an isotropic environment, the gradient orientation has little to no impact, whereas in anisotropic tissues like white matter, water preferentially diffuses along axons. Acquiring signals along multiple gradient directions enables the estimation of directional diffusion properties.

Finally, the PGSE signal can be expressed as:

$$S(b, TE) = S_0 \exp(-bD) \exp(-\frac{TE}{T_2}) \tag{1.4}$$

where TE is the echo-time and T_2 is the transverse relaxation time.

1.3 Artifacts and noise in dMRI

In dMRI, the measured signal is affected by various sources of noise and artifacts that can significantly impact image quality and the reliability of quantitative measurements. These alterations arise from multiple factors including thermal noise, hardware imperfection, subject motion or magnetic field inhomogeneities (Gudbjartsson and Patz 1995; D. K. Jones and P. J. Basser 2004; Koay and P. J. Basser 2006; C. M. Tax et al. 2022). Understanding their origin and effects is essential for the design of acquisition protocols as well as the interpretation of diffusion-derived metrics.

In this section, we first focus on noise as it plays a central role in parameter estimation and model fitting, which are important parts of the work presented in the second part of the manuscript. We then review the most common artifacts encountered in diffusion MRI acquisitions such as motion, eddy currents and geometric distortions.

1.3.1 Signal to Noise Ratio in diffusion MRI

The signal-to-noise ratio (SNR) quantifies the strength of the measured signal relative to the noise and is defined as:

$$SNR = \frac{\langle S \rangle}{\sigma} \tag{1.5}$$

where $\langle S \rangle$ is the mean signal and σ is the standard deviation of the noise. Assuming the signal was acquired on the full k-space, the noise in the complex image (for both the real and the imaginary signals) can be modeled by a Gaussian distribution with a zero mean and a standard deviation σ. Based on this distribution, the signal in the magnitude image is distributed following a Rician distribution.

The diffusion sequence strongly impacts the SNR. From the Stejskal-Tanner equation:

$$S(b) = S_0 \exp(-bD) \tag{1.6}$$

the signal decays exponentially with increasing b-value. Compared to non-diffusion-weighted acquisitions ($b = 0$), diffusion-weighted signals are therefore substantially attenuated. As a consequence, at higher b-values, the SNR decreases which can degrade the precision and accuracy of estimated quantities such as diffusion coefficients or parameters of microstructural models.

In practice, clinical diffusion MRI typically uses b-values up to 1000 $\mathrm{s\,mm^{-2}}$, while research often require higher b-values, around a few thousands. Those higher b-values come at the cost of reduced SNR. The echo-time (TE) also affects the SNR through transverse relaxation. As introduced in the previous section, the signal can be expressed as:

$$S(b, TE) = S_0 \exp(-bD) \exp(-\frac{TE}{T_2}) \tag{1.7}$$

Increasing TE leads to additional decay due to T_2 relaxation, further reducing the SNR. In practice, diffusion-weighted sequences often require longer TE due to the diffusion gradients.

Finally, acquisition parameters such as the magnetic field strength and voxel size also influence the SNR. Higher field strengths generally increase the signal, leading to an improved SNR. Similarly, increasing the voxel size can also increase SNR by averaging over a larger volume, although this comes at the cost of spatial resolution.

1.3.2 Common artifacts

In addition to noise, several artifacts can alter diffusion MRI data and affect the reliability of analyses. These artifacts originate from subject motion, hardware limitations and imperfections in the acquisition and reconstruction processes. In this section, we briefly describe some of the most common artifacts encountered in diffusion MRI.

Motion

Diffusion MRI acquisitions typically require the acquisition of multiple diffusion-weighted images with different gradient directions and/or b-values, resulting in relatively long scan times. As a consequence, subject motion during the acquisition is difficult to avoid.

Motion between successive acquisitions can lead to misalignment between images, while intra-volume motion can cause signal drops or slice-wise inconsistencies. These ef-

fects accumulate over the acquisition and can significantly bias the estimation of diffusion-related quantities if not corrected during preprocessing.

Magnetic field inhomogeneities

MRI assumes a homogeneous magnetic field B_0. However in practice, spatial variations arise due to scanner imperfections and susceptibility differences at tissues interfaces.

In diffusion MRI, these inhomogeneities can lead to geometric distortions, particularly in echo-planar imaging (EPI), which is commonly used for diffusion acquisitions. They may also cause signal loss locally.

Eddy currents

The rapid switching of strong diffusion gradients induces eddy currents in the conductive components of the MRI system or in the patient. These currents can results in shifts in the magnetic field or unwanted gradients.

As a result, eddy currents can introduce geometric distorsions, scaling effects, blurring and shearing in the images. They can also lead to misalignment between diffusion-weighted images acquired with different gradient directions, ultimately biasing the estimation of diffusion metrics such as the apparent diffusion coefficient.

Gibbs ringing

The Gibbs ringing artefact appears as oscillatory patterns near sharp intensity transitions, such as tissue boundaries (Gibbs 1898). It arises from the truncation of high-frequency components in k-space, which corresponds to an incomplete sampling of the Fourier domain.

This artifact manifests as ripples around edges and can affect quantitative analyses.

1.4 Conclusion

Diffusion MRI provides a unique window into tissue microstructure by encoding the random motion of water molecules into the MR signal. Sequences such as spin-echo and pulsed gradient spin-echo allow this motion to be measured but the resulting signal is influenced by acquisition parameters, relaxation effects and inherent noise. Various artifacts

and signal distortions can further influence the data, requiring careful preprocessing and quality control.

Chapter 2

Modeling white matter microstructure

Understanding the underlying structure of white matter is crucial to study various disorders, including degenerative diseases and traumatic injuries. The study of white matter *in vivo* relies on imaging techniques such as diffusion MRI, which provides a signal that indirectly reflects the microstructure through the displacement of water molecules. Due to the complexity of this signal, it is necessary to model the tissue microstructure and the diffusion process in order to interpret the signal in terms of tissue properties. Since the early days of diffusion MRI, the question of how best to represent microstructure and diffusion models has been a central topic within the research community.

In this chapter, we will start by describing the brain microstructure, focusing on white matter. Then, we will go over models that are widely used within the community. First, we will look into *mathematical models*, they aim to represent the signal with mathematical objects. These models are fairly simple, robust and are efficient when it comes to computational power, however, they lack meaning that can be easily translated into tissue parameters. Then, we will present very common *biophysical models*. These models aim to represent the tissues which provide more biologically interpretable parameters but they tend to be very expensive computationally as well as lacking robustness in parameter estimation. Then, we will comment on the two types of models presented as well as hybrid models. Afterward, we will review the tools available for simulating diffusion signals, as well as the phantoms used for these simulations. These include phantoms representing microstructure within a voxel and those used to simulate signals for tractography, often employing simplified white matter structures to mimic whole-brain connectivity patterns. Finally, we will open on a fairly recent area in the field: grey matter microstructure models.

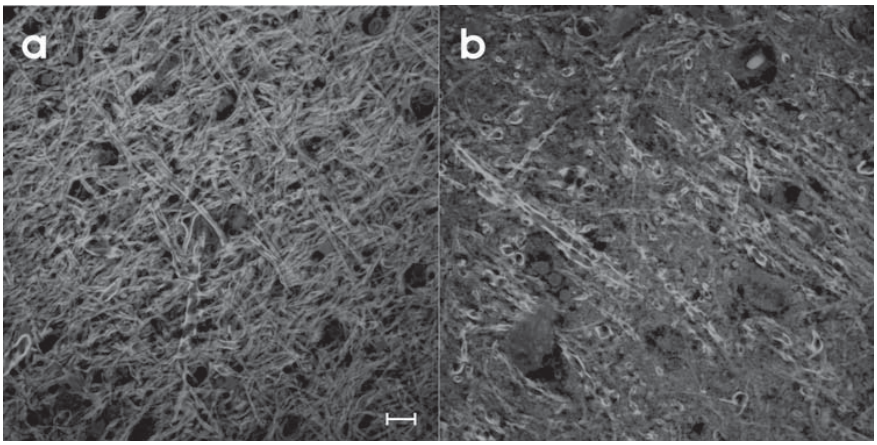

Figure 2.1 – Sections of the human brain where myelin sheaths are stained with fluorescent dye DiI, visualized with confocal laser scanning microscopy. The scale bar represent 20μm. (a) Slice of subcortical white matter. (b) Slice of lateral thalamus. Figure from D. K. Jones (2010).

2.1 Brain microstructure

The study of the brain and its connections dates back to the 17th century when anatomist Thomas Willis performed postmortem dissection of the brain (Willis 1664). Although anatomists were able to see distinctions between white and grey matter, it was not until the popularization of light microscopy that they were able to look at the tissues in more details. When chemical staining was introduced in histology during the 19th century, the organization and morphology of white matter became visible. Histology is the gold standard of *ex vivo* techniques to get ground-truth microstructure information. However, this technique is very destructive as tissues need to be fixed, stained and cut to be studied. During the treatment of the tissue, it is also altered as the diameter of axons or the densities cannot be preserved. Over the years, new techniques have been developed and used to improve the scan of microscopic tissues. This techniques can been used to scan slices of white matter. Such tissues can be seen in Figure 2.1 where confocal laser scanning was used on stained tissue. Recently, 3D synchrotron X-ray nano-holomography has also be used to acquire images of white matter samples from the corpus callosum of a monkey brain (Andersson et al. 2020). These images allowed for a 3D reconstruction of the axons (cf Figure 2.2).

Studies on the brain over the years have allowed for a better understanding of the

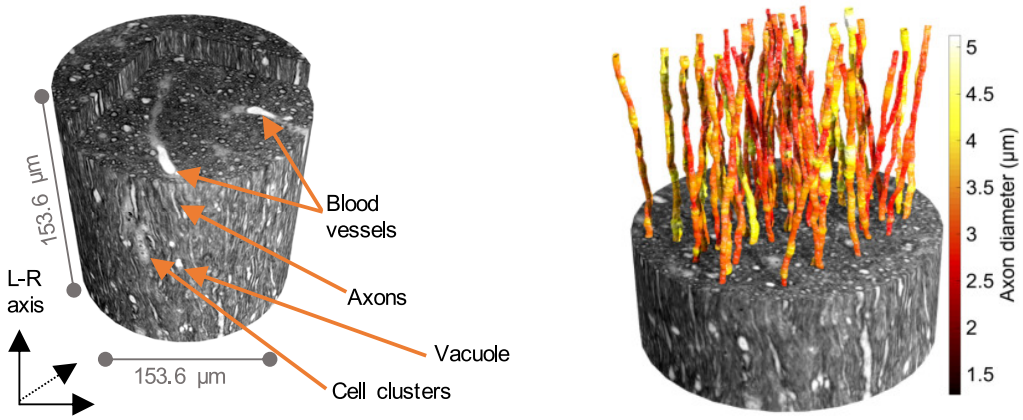

Figure 2.2 – White matter sample from the corpus callosum of a monkey brain using 3D synchrotron X-ray nano-holomography. (left) Acquired volume where blood vessels, axons, vacuole and cell clusters are highlighted. (right) Segmented axons extracted from the sample. Figure adapted from Andersson et al. (2020).

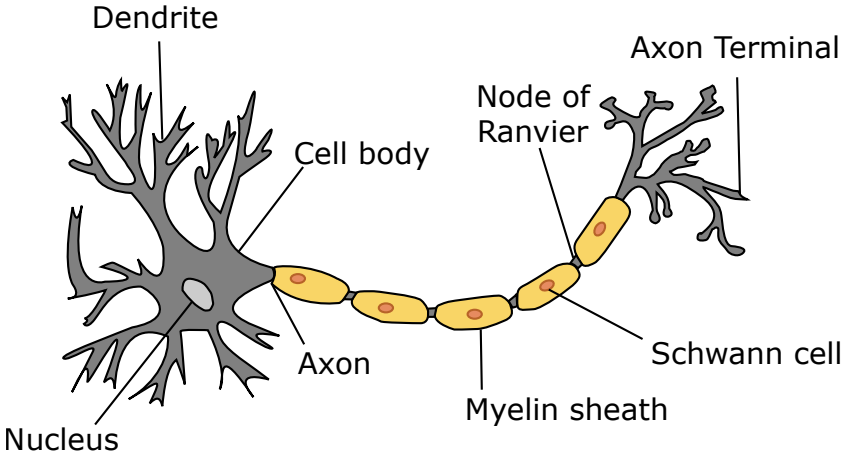

Figure 2.3 – Diagram of a neuron. Figure from US National Cancer Institute's Surveillance, Epidemiology and End Results (SEER) Program.

microstructure within the brain, on both white and grey matter as well as the brain functions. Advances in understanding microstructure lead to the description of neurons the way it is shown in Figure 2.3. In this diagram, both grey and white matter can be seen. The cell body, dendrites and nucleus are constituant of grey matter whereas axon, myelin sheath, Schwann cell and nodes of Ranvier are constituant of white matter. Axon terminals connect the axon in the white matter to the cell body or dendrites in the grey matter. We have also gained insights of some exchange dynamics. These exchanges occur in various components of both grey and white matter, as cell membranes are partially permeable. They primarily involve the transfer of ions, metabolites, and other small molecules between cells and the extracellular space, which is not visible in the diagram. This space is the space between cells that is filled with fluid that serves as the soluble carrying proteins or neurotransmitters for example.

The microstructure of the brain can be categorized into distinct compartments based on how they influence the diffusion MRI signal. For white matter, which is the area of interest for almost all models that will be presented in this chapter, three main compartments are considered: the *intra-axonal* compartment, the *extra-axonal* compartment and the *cerebrospinal fluid (CSF)* compartment. The intra-axonal compartment is constituted of the axon where the diffusion is anisotropic, and can be described as *restricted diffusion*. Its properties can be quantified by microstructural parameters such as axon density, axon diameter distribution, and orientation dispersion, which reflect the underlying tissue architecture. The extra-axonal compartment is, as described previously, the space between axons, filled with fluid. In this compartment, the diffusion is described as *hindered*, due to the restrictions created by the axons. The last compartment, CSF, is where the diffusion can be considered as *isotropic*, just like free water. This compartment is generally found in ventricles. This compartmentalization of the microstructure based on their respective diffusion properties is the foundation for *biophysical modelling* and reflects the underlying tissue microstructure, which determines the diffusion behavior of water molecules. The diffusion properties in each compartment (restricted, hindered and isotropic) then shape the MRI signal that is measured. In other words, the signal is an indirect readout of microstructural features.

2.2 Mathematical models

Understanding brain microstructure through diffusion MRI is challenging, as it requires modelling to relate the measured diffusion-weighted signal to the underlying tissue microstructure. In other words, the goal is not just to describe the signal itself, but to interpret how diffusion properties estimated from the signal reflect microstructural features. As mentioned earlier, there are two main modelling approaches. The first one is to represent mathematical constructs without directly linking them to tissue biology. In this section, we will focus on this first approach, more specifically, on some commonly used models and historically relevant models. We will first describe Diffusion Tensor Imaging (DTI) as the first model in Diffusion MRI, still extremely used today. Then, we will present Diffusion Kurtosis Imaging (DKI) as one of the most important extension of DTI that accounts for non-Gaussian diffusion in tissues through the measure of *kurtosis*. Then/diffusion , we will describe in details the Diffusion Tensor Distribution (DTD) as the model used in the contributions of this thesis. This model can be seen as a generalization of DTI or even DKI, describing a voxel by a mixture of microenvironments. Finally, we will also go over MAPMRI, as well as its extension MAPL more quickly as it is an important model used by many in the community but will not be used later in this manuscript.

2.2.1 Diffusion Tensor Imaging (DTI)

The most commonly used mathematical model to represent the diffusion in the voxel is the diffusion tensor (P. Basser, Mattiello, and LeBihan 1994). In the case of anisotropy, the diffusion happens mainly following the principal axis of the anisotropy. Thus, the diffusion can be seen as an ellipsoid or a sphere in case the diffusion is isotropic.

The diffusion tensor captures the displacement of water molecules in all directions during the diffusion time, under the assumption of Gaussian diffusion. The diffusion tensor $\mathbf{D}$ takes the form of a 3×3 symmetric, positive-definite matrix:

$$\mathbf{D} = \begin{pmatrix} D_{xx} & D_{xy} & D_{xz} \\ D_{xy} & D_{yy} & D_{yz} \\ D_{xz} & D_{yz} & D_{zz} \end{pmatrix} \tag{2.1}$$

This definition of the diffusion tensor $\mathbf{D}$ is in the axis space of the scanner, meaning the diffusion tensor in this form is not aligned principal direction of anisotropy. We can diagonalize the diffusion tensor to express it in the basis of its eigenvectors. The eigenvector

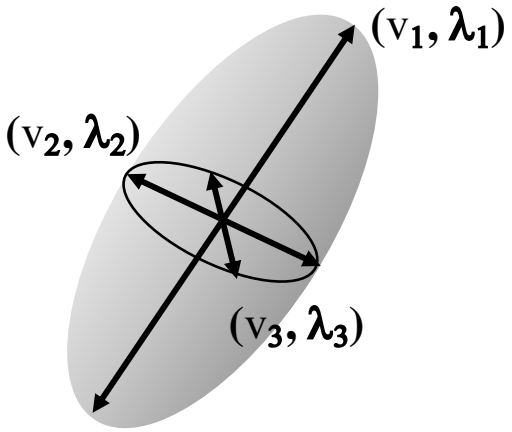

Figure 2.4 – Schema of a diffusion tensor. Here, the eigenvalues are given by λ_1, λ_2 and λ_3, their associated eigenvectors are given by v_1, v_2 and v_3.

associated with the largest eigenvalue indicates the principal diffusion direction, which can then be used to assess anitropy and isotropy. This diffusion tensor can be seen in Figure 2.4.

For this model, the signal S is given by:

$$S = S_0 \exp(-b\mathbf{g}^T\mathbf{D}\mathbf{g}) \tag{2.2}$$

where S_0 is the signal without diffusion and b is the b-value defined in the previous chapter, $\mathbf{g}$ is a unit vector representing the direction of the applied diffusion-sensitizing magnetic field gradient and $\mathbf{D}$ is the diffusion tensor. Using a sufficient number of measurements along non-collinear gradient directions (at least six), we obtain a system of linear equations that can be solved to estimate the elements of $\mathbf{D}$.

From this tensor, several features of interest called diffusion properties can be extracted (P. J. Basser and Pierpaoli 1996). Let's review the most commonly used.

Mean diffusivity (MD)

The mean diffusivity gives a measure of how much diffusion happened in the voxel during the acquisition. This mean diffusivity is computed from the trace of the diffusion tensor $\mathbf{D}$ as:

$$MD = \frac{Tr(\mathbf{D})}{3} = \frac{\lambda_1 + \lambda_2 + \lambda_3}{3} = \langle\lambda\rangle \tag{2.3}$$

The mean diffusivity is higher when water can diffuse more freely and smaller when the diffusion is more restricted.

Fractional Anisotropy (FA)

The fractional anisotropy (FA) is a scalar measure, between 0 and 1, that quantifies the anisotropy within the voxel. This metric is defined as:

$$FA = \sqrt{\frac{3}{2}} \frac{\sqrt{(\lambda_1 - \langle\lambda\rangle)^2 + (\lambda_2 - \langle\lambda\rangle)^2 + (\lambda_3 - \langle\lambda\rangle)^2}}{\sqrt{\lambda_1^2 + \lambda_2^2 + \lambda_3^2}} \tag{2.4}$$

When the FA is close to 1, the diffusion is highly anisotropic and corresponds to well-aligned axons along a dominant direction. When the FA approaches 0, diffusion becomes more isotropic, which may occur in cerebrospinal fluid or grey matter. However, low FA values may also arise from other situations, such as fiber crossings within a voxel, demyelination or a large extra-axonal contribution. This illustrates that FA is not specific to a single microstructural configuration as different tissue organizations can produce similar FA values, which limits the direct interpretability of this parameter in terms of underlying microstructure.

Tensor Orientation

The tensor orientation can be determined from the eigenvectors of the estimated diffusion tensor. In the case of anisotropic diffusion, the main diffusion direction corresponds to the eigenvector associated with the largest eigenvalue, which indicates the direction of maximal diffusivity. More details on its usage will be given in Chapter 4.

2.2.2 Diffusion Kurtosis Imaging (DKI)

Although DTI performs well in many situations for the study of white matter, it fails to capture complex tissue configurations and intra-voxel heterogeneity. One of the main assumptions of DTI is that diffusion is Gaussian. However, in biological tissues, this assumption is only valid under specific conditions. In particular, for very short diffusion times the distribution of water molecule displacements may remain close to Gaussian, whereas for diffusion times on the order of tens of milliseconds, the complex cellular organization of tissues leads to deviations from Gaussian behaviour. These deviations

arise from barriers such as cell membranes, myelin and other structures that hinder or restrict molecular motion.

To account for this non-Gaussian diffusion, Diffusion Kurtosis Imaging (DKI) was introducted (Jensen, Helpern, et al. 2005). DKI extends DTI by quantifying the deviation of the diffusion displacement from Gaussianity using a cumulant expansion (a Taylor expansion of the logarithm of the signal). The diffusion-weighted signal can be written as:

$$\ln \frac{S}{S_0} = -b\mathbf{g}^T\mathbf{D}\mathbf{g} + \frac{1}{6}b^2(\mathbf{g}^{\otimes 4} : \mathbb{W}) \tag{2.5}$$

where $\mathbf{D}$ is the diffusion tensor, $\mathbf{g}$ is the unit diffusion gradient and $\mathbb{W}$ is the kurtosis tensor, The apparent kurtosis depends on the gradient direction because diffusion restrictions vary with tissue orientation. This directional dependance is described by the fourth-order kurtosis tensor $\mathbb{W}$, which possesses 15 independant components and can be defined from cumulants of the molecular displacement vector $\mathbf{s}$ as:

$$\mathbb{W}_{ijkl}(t) = 9\frac{\langle s_i s_j s_k s_l\rangle - \langle s_i s_j\rangle\langle s_k s_l\rangle - \langle s_i s_k\rangle\langle s_j s_l\rangle - \langle s_i s_l\rangle\langle s_j s_k\rangle}{\langle \mathbf{s}.\mathbf{s}\rangle^2} \tag{2.6}$$

where s_i is a component of the net displacement vector $\mathbf{s}$.

Using this signal representation, the parameters such as MD and FA obtained in DTI can still be recovered, while additional measures describing non-Gaussian diffusion can be defined. The most commonly used metric is the mean kurtosis (MK), defined as the orientation of the directional kurtosis (Hansen et al. 2013):

$$MK = \frac{1}{4\pi}\int_{|n|=1} < \mathbb{W}, \mathbf{n}^{\otimes 4} > dS \tag{2.7}$$

2.2.3 Diffusion Tensor Distribution (DTD)

For most of this manuscript, we will focus on the Diffusion Tensor Distribution (DTD) model introduced in (Jian et al. 2007). In this framework, the diffusion-weighted signal within a voxel is represented as arising from a distribution of microscopic diffusion environments, rather than from a single diffusion tensor. Each microenvironment is characterized by its own diffusion tensor $\mathbf{D}$ (see Figure 2.5). The DTD therefore describes the variability of local diffusion properties within the voxel, allowing the model to account for increased tissue complexity.

Averaging over this DTD within the voxel yields the mean diffusion tensor $\langle\mathbf{D}\rangle$, which

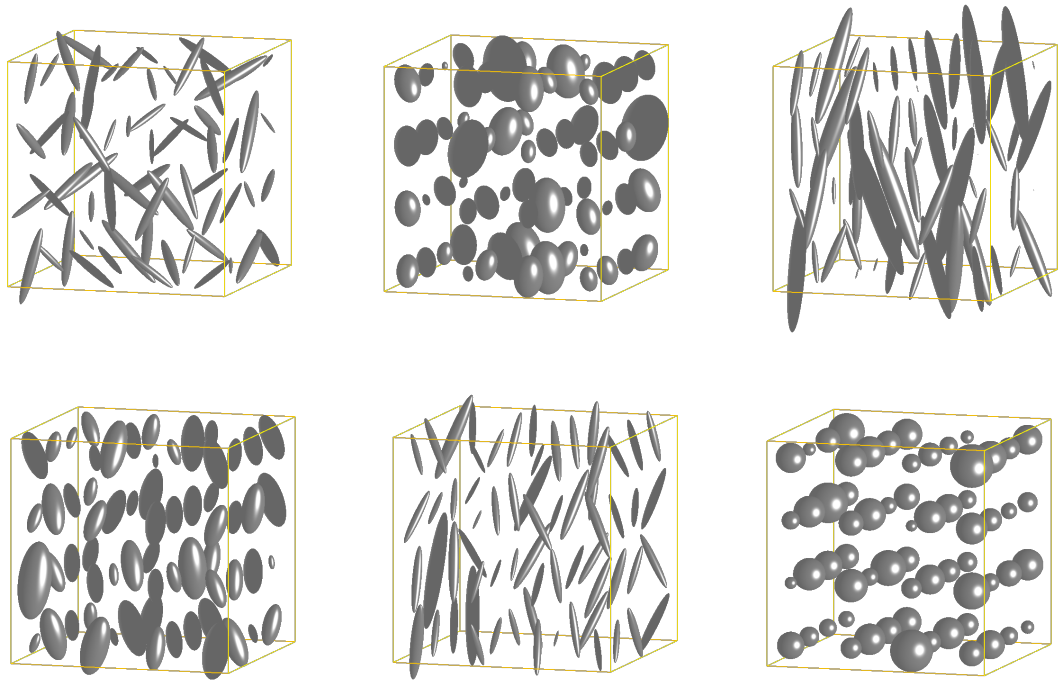

Figure 2.5 – Examples of diffusion tensor distributions (DTD) with different parameters.

corresponds to the effective tensor estimated in earlier models such as Diffusion Tensor Imaging. The covariance of $\mathbf{D}$ is a fourth-order tensor $\mathbb{C}$ (P. J. Basser and Pajevic 2007) given by:

$$\mathbb{C} = \langle \mathbf{D}^{\otimes 2} \rangle - \langle \mathbf{D} \rangle^{\otimes 2} \tag{2.8}$$

where $\mathbf{D}^{\otimes 2}$ is the outer product of $\mathbf{D}$ with itself. This product is computed using the Voigt notation $\mathbf{d}$ of a symmetric 3×3 tensor D containing its six distinct components as follows:

$$\mathbf{d} = \begin{pmatrix} d_{xx} & d_{yy} & d_{zz} & \sqrt{2}d_{yz} & \sqrt{2}d_{xz} & \sqrt{2}d_{xy} \end{pmatrix}^T \tag{2.9}$$

Then, the outer product is computed by:

$$\langle \mathbf{D}^{\otimes 2} \rangle = \langle \mathbf{d}\mathbf{d}^T \rangle = \langle d_i d_j \rangle \tag{2.10}$$

with $i, j \in \{xx, yy, zz, yz, xz, xy\}$.

$\langle \mathbf{D} \rangle^{\otimes 2}$ is defined by:

$$\langle \mathbf{D} \rangle^{\otimes 2} = \langle \mathbf{d} \rangle \langle \mathbf{d} \rangle^T = \langle d_i \rangle \langle d_j \rangle \tag{2.11}$$

This covariance matrix can also be expressed as:

$$c_{ij} = \langle d_i d_j \rangle - \langle d_i \rangle \langle d_j \rangle \tag{2.12}$$

or as:

$$\mathbb{C} = \begin{pmatrix} c_{xx,xx} & c_{xx,yy} & c_{xx,zz} & \sqrt{2}c_{xx,yz} & \sqrt{2}c_{xx,xz} & \sqrt{2}c_{xx,xy} \\ c_{yy,xx} & c_{yy,yy} & c_{yy,zz} & \sqrt{2}c_{yy,yz} & \sqrt{2}c_{yy,xz} & \sqrt{2}c_{yy,xy} \\ c_{zz,xx} & c_{zz,yy} & c_{zz,zz} & \sqrt{2}c_{zz,yz} & \sqrt{2}c_{zz,xz} & \sqrt{2}c_{zz,xy} \\ \sqrt{2}c_{yz,xx} & \sqrt{2}c_{yz,yy} & \sqrt{2}c_{yz,zz} & 2c_{yz,yz} & 2c_{yz,xz} & 2c_{yz,xy} \\ \sqrt{2}c_{xz,xx} & \sqrt{2}c_{xz,yy} & \sqrt{2}c_{xz,zz} & 2c_{xz,yz} & 2c_{xz,xz} & 2c_{xz,xy} \\ \sqrt{2}c_{xy,xx} & \sqrt{2}c_{xy,yy} & \sqrt{2}c_{xy,zz} & 2c_{xy,yz} & 2c_{xy,xz} & 2c_{xy,xy} \end{pmatrix} \tag{2.13}$$

This covariance matrix has two symmetries: the major symmetry ($c_{ab,cd} = c_{cd,ab}$) and the minor symmetry ($c_{ab,cd} = c_{ba,cd}$). This results in 21 unique coefficients out of 36.

In this thesis, we position ourselves within the Q-space trajectory imaging (QTI)

framework (C.-F. Westin, Hans Knutsson, et al. 2016). The first component of this framework is the modeling step, in which the diffusion signal within a voxel is represented using a DTD model, rather than directly modelling the tissue itself. The second component concerns the acquisition encoding. QTI uses generalized gradient waveforms, which can be described using the formalism of b-tensor, a second-order tensor that we will note $\mathbf{B}$ in the following. This encoding scheme will be described in details in the next chapter.

Signal expression

In the QTI framework, the signal S can be expressed as:

$$S(\mathbf{B}) = S_0\langle\exp(- < \mathbf{B}, \mathbf{D} >)\rangle \tag{2.14}$$

where S_0 is the non-diffusion weighted signal, $\langle . \rangle$ averages the signal over all microenvironments in the voxel and $< \mathbf{B}, \mathbf{D} >$ is the inner product of $\mathbf{B}$ with $\mathbf{D}$ defined as:

$$< \mathbf{B}, \mathbf{D} >= \mathbf{b}^T\mathbf{d} = \sum_{i=1}^{3}\sum_{j=1}^{3} B_{ij}D_{ij}, \tag{2.15}$$

where $\mathbf{b}$ and $\mathbf{d}$ are the Voigt notation of $\mathbf{B}$ and $\mathbf{D}$, respectively.

The signal can be approximated using the cumulant expansion of S with its first two moments as:

$$S(\mathbf{B}) \approx S_0 \exp(- < \mathbf{B}, \langle\mathbf{D}\rangle > + \frac{1}{2} < \mathbb{B}, \mathbb{C} >) \tag{2.16}$$

where $\langle\mathbf{D}\rangle$ is the mean diffusion tensor, $\mathbb{B} = \mathbf{B}^{\otimes 2}$ and $\mathbb{C}$ is the covariance matrix of DTD.

Invariants definition

From the mean tensor $\langle\mathbf{D}\rangle$ and the covariance matrix $\mathbb{C}$ of the DTD, several scalar invariants can be defined. The DTI invariants such as the mean diffusivity (MD), can be computed as:

$$MD(\langle\mathbf{D}\rangle) =< \langle\mathbf{D}\rangle, \mathbf{E}_{iso} > \tag{2.17}$$

$$= \frac{1}{3}(d_{xx} + d_{yy} + d_{zz}) \tag{2.18}$$

where $\mathbf{E}_{iso}$ is the isotropic second-order identity tensor defined by:

$$\mathbf{E}_{iso} = \frac{1}{3}\mathbf{I} = \frac{1}{3}\begin{pmatrix} 1 & 0 & 0 \\ 0 & 1 & 0 \\ 0 & 0 & 1 \end{pmatrix} \tag{2.19}$$

and d_{xx}, d_{yy} and d_{zz} are the diagonal elements of $\langle \mathbf{D} \rangle$.

Two other scalar invariants, V_{MD} and V_{shear}, can be derived from the covariance matrix $\mathbb{C}$ of the tensor distribution. Let $\mathbb{E}_{iso}$ be the isotropic fourth-order defined as:

$$\mathbb{E}_{iso} = \frac{1}{3}\begin{pmatrix} 1 & 0 & 0 & 0 & 0 & 0 \\ 0 & 1 & 0 & 0 & 0 & 0 \\ 0 & 0 & 1 & 0 & 0 & 0 \\ 0 & 0 & 0 & 1 & 0 & 0 \\ 0 & 0 & 0 & 0 & 1 & 0 \\ 0 & 0 & 0 & 0 & 0 & 1 \end{pmatrix} \tag{2.20}$$

with its bulk modulus $\mathbb{E}_{bulk}$ and shear modulus $\mathbb{E}_{shear}$ defined as:

$$\mathbb{E}_{bulk} = \mathbf{E}_{iso}^{\otimes 2} = \frac{1}{9}\begin{pmatrix} 1 & 1 & 1 & 0 & 0 & 0 \\ 1 & 1 & 1 & 0 & 0 & 0 \\ 1 & 1 & 1 & 0 & 0 & 0 \\ 0 & 0 & 0 & 0 & 0 & 0 \\ 0 & 0 & 0 & 0 & 0 & 0 \\ 0 & 0 & 0 & 0 & 0 & 0 \end{pmatrix} \tag{2.21}$$

$$\mathbb{E}_{shear} = \mathbb{E}_{iso} - \mathbb{E}_{bulk} = \frac{1}{9}\begin{pmatrix} 2 & -1 & -1 & 0 & 0 & 0 \\ -1 & 2 & -1 & 0 & 0 & 0 \\ -1 & -1 & 2 & 0 & 0 & 0 \\ 0 & 0 & 0 & 3 & 0 & 0 \\ 0 & 0 & 0 & 0 & 3 & 0 \\ 0 & 0 & 0 & 0 & 0 & 3 \end{pmatrix} \tag{2.22}$$

then V_{MD} and V_{shear} are obtained by projection of $\mathbb{C}$:

$$V_{MD} =< \mathbb{C}, \mathbb{E}_{bulk} > \tag{2.23}$$

$$V_{shear} =< \mathbb{C}, \mathbb{E}_{shear} > \tag{2.24}$$

The invariant V_{MD} can be expressed as the variance in mean diffusivities and reflects the size variation of the tensors in the DTD:

$$V_{MD} = \langle MD^2 \rangle - \langle MD \rangle^2 \tag{2.25}$$

In contrast, V_{shear} captures the variance associated with anisotropic deviations from isotropy and is therefore linked to the dispersion in shape and orientation of the tensors within the distribution. The total isotropic variance V_{iso} is obtained as the sum of V_{MD} and V_{shear} and provides a global measure of variability within the DTD.

Definition of new features of interest

From these, normalized parameters from the model, ranging from 0 to 1, are defined. The first one is the normalized size variance of the tensors defined as:

$$C_{MD} = \frac{< \mathbb{C}, \mathbb{E}_{bulk} >}{< \langle \mathbf{D}^{\otimes 2} \rangle, \mathbb{E}_{bulk} >} \tag{2.26}$$

Microscopic and macroscopic fractional anisotropies, measuring the shape of microenvironments, can be defined. The microscopic anisotropy reflects the anisotropy of the microscopic diffusion within compartments whereas the macroscopic anisotropy captures both microscopic anisotropy and orientation dispersion at the voxel scale. When they approach 1, they corresponds to high anisotropy. They can be computed by:

$$C_\mu = \frac{3}{2} \frac{< \langle \mathbf{D}^{\otimes 2} \rangle, \mathbb{E}_{shear} >}{< \langle \mathbf{D}^{\otimes 2} \rangle, \mathbb{E}_{iso} >} = \mu FA^2 \tag{2.27}$$

$$C_M = \frac{3}{2} \frac{< \langle \mathbf{D} \rangle^{\otimes 2}, \mathbb{E}_{shear} >}{< \langle \mathbf{D} \rangle^{\otimes 2}, \mathbb{E}_{iso} >} = FA^2 \tag{2.28}$$

Finally, a measure to quantify the orientation coherence of microenvironments, inspired by the "order parameter" in liquid crystals, can be defined. This orientational order parameter (OP), which approaches 1 when the dispersion of orientations within the voxel is very low and decreases as orientations become more dispersed, is defined as:

$$OP^2 = \frac{< \langle \mathbf{D} \rangle^{\otimes 2}, \mathbb{E}_{shear} >}{< \langle \mathbf{D}^{\otimes 2} \rangle, \mathbb{E}_{shear} >} \tag{2.29}$$

The effect of the size variance (C_{MD}), the microscopic anisotropy (μFA) and the orientation parameter (OP) on the distribution of diffusion tensors are illustrated in Figure

2.6. This framework could also be linked with DKI parameters using the fourth moment of the approximation for the signal expression as shown in C.-F. Westin, Hans Knutsson, et al. (2016).

Parameters estimation

To estimate these features of interest, we need to estimate $\langle \mathbf{D} \rangle$ and $\mathbb{C}$. As we see in Equation 2.14, we also need to estimate S_0. In order to do so, the following equation system is to be solved:

$$\begin{pmatrix} \log S_1 \\ . \\ . \\ . \\ \log S_m \end{pmatrix} = \begin{pmatrix} 1 & -\mathbf{b}_1^T & \frac{1}{2}\mathbb{b}_1^T \\ . & . & . \\ . & . & . \\ . & . & . \\ 1 & -\mathbf{b}_m^T & \frac{1}{2}\mathbb{b}_m^T \end{pmatrix} \begin{pmatrix} \log S_0 & \langle \mathbf{d} \rangle & \mathbb{c} \end{pmatrix}^T \tag{2.30}$$

where $\mathbb{b}$ (resp. $\mathbb{c}$) is the Voigt notation (vector of size 21) of $\mathbb{B}$ (resp. $\mathbb{C}$), m is the number of acquisitions and β is the vector of size 28 containing the model parameters. This system can be written as:

$$\mathbf{s} = \mathbf{X}\beta \tag{2.31}$$

The parameter vector β can be estimated using its pseudoinverse β^*:

$$\beta^* = \left(\mathbf{X}^T\mathbf{X}^{-1}\right)\mathbf{X}^T\mathbf{s}. \tag{2.32}$$

The QTI framework was later improved in QTI+ framework (Herberthson et al. 2021) by adding positivity constraints in order to improve the accuracy and precision of measured parameters by enforcing physical plausibility. Those constraints are the following positivity constraints on $\mathbf{D}$ and $\mathbb{C}$:

1. The mean diffusion tensor needs to be positive semi-definite:

$$\langle \mathbf{D} \rangle \geq 0 \tag{2.33}$$

2. The covariance matrix needs to be positive semi-definite:

$$\mathbb{C} \geq 0 \tag{2.34}$$

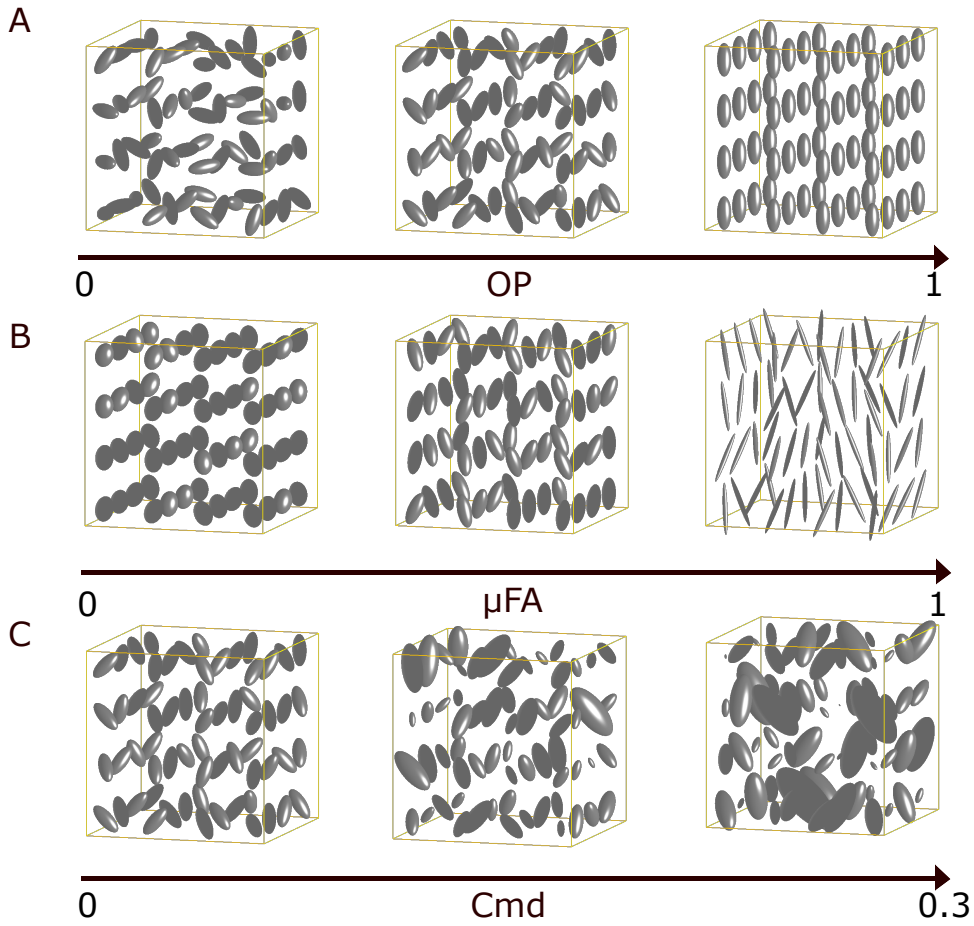

Figure 2.6 – Effects of the orientation parameter (A), the microscopic anisotropy (B) and the size variance (C) on diffusion tensors distributions. (A) Effect of the orientation parameter with μFA set at 0.5 and C_{MD} at 0. (B) Effect of the microscopic anisotropy with C_{MD} set at 0 and OP at 0.8. (C) Effect of the size variance on DTDs with μFA fixed at 0.5 and OP at 0.5.

3. The mean of the outer product of diffusion tensors also needs to be positive semi-definite:

$$\langle \mathbf{D}^{\otimes 2} \rangle \geq 0 \tag{2.35}$$

2.2.4 Mean Apparent Propagator MRI (MAPMRI)

Over the years, several representations of the signal have been proposed. Some extend the tensor-based approach of DTI, while other model the signal using alternative frameworks. For example, in MAPMRI (Özarslan et al. 2013), the authors fit the signal in a specific basis. Many models assume the signal is Gaussian, although this assumption is often violated in brain tissue. Here, the authors relaxed this assumption and aimed at reconstructing an apparent propagator from the diffusion signal. This allows to capture non-Gaussian diffusion as well as features from heterogenous tissues. Such a propagator $P(\mathbf{r})$ gives the probability of a water molecule to be displaced by $\mathbf{r}$ during the diffusion time as:

$$P(\mathbf{r}) = \int \frac{S(\mathbf{q})}{S_0} \exp\left(2\pi i \mathbf{q}\mathbf{r}\right) d\mathbf{q} \tag{2.36}$$

where $S(\mathbf{q})$ is the diffusion-weighted signal, S_0 is the measured signal without diffusion and $\mathbf{q}$ is defined as:

$$\mathbf{q} = \frac{\gamma \delta \mathbf{g}}{2\pi} \tag{2.37}$$

where γ is the gyromagnetic ratio, δ is the diffusion time and $\mathbf{g}$ is the diffusion gradient applied.

The framework can be seen as a two-part signal representation. The first part is the anisotropic Gaussian attenuation of the signal, as found in DTI ; the second part is the expansion modelling non-Gaussian deviation from the Gaussian attenuation. The diffusion signal can then be seen as:

$$S(\mathbf{q}) = S_{DTI}(\mathbf{q}) S_{residual}(\mathbf{q}) \tag{2.38}$$

In Özarslan et al. (2013), this second term is a linear combinaison of basis functions relying on Hermite functions and spherical harmonics and can be defined as:

$$S(\mathbf{q}) = S_0 \sum_{N=0}^{N_{max}} \sum_{\{n_1,n_2,n_3\}} a_{n_1n_2n_3} \Phi_{n_1n_2n_3}(\mathbf{A}, \mathbf{q}) \tag{2.39}$$

where $n_1 + n_2 + n_3 = N$, $\Phi_{n_1n_2n_3}$ are the basis function in q-space and $\mathbf{A}$ is a matrix defining anisotropy, the shape and orientation of the basis functions.

Using this model, parameters are extracted from the reconstructed apparent propagator. The first one is a zero displacement probability, ie the return-to-the-origin probability (RTOP) defined as:

$$RTOP = P(\mathbf{r} = 0) \tag{2.40}$$

Similarly, a return-to-the-axis probability (RTAP), reflecting the radial confinement, is defined as:

$$RTAP = \int P(r_x = 0, r_y = 0, r_z) dr_z \tag{2.41}$$

and a return-to-the-plane probability (RTPP), reflecting confinement in the direction of the fiber orientation as:

$$RTPP = \int P(r_x = 0, r_y, r_z) dr_y dr_z \tag{2.42}$$

Two other parameters are defined by comparing the propagator and a conterpart: the propagator anisotropy (PA) and the non-gaussianity (NG). The propagator anisotropy measure the similarity between the anisotropic Gaussian propagator and the isotropic Gaussian propagator, whereas the non-gaussianity index quantifies the dissimilarity between the propagator and its gaussian part.

Extensions of this framework have been proposed over the years to improve it such as the addition of a Laplacian regularization term (Fick et al. 2016) in order to reduce overfitting, improve the estimation of several microstructure parameters or even reduce the number of acquisitions.

2.3 Biophysical models

While mathematical models provide a convenient way to represent the diffusion signal, interperting their parameters in terms of underlying tissue microstructure is not straigthforward, since these parameters are often indirect and lack specificity for particular tissue

features. In contrast, biophysical models aim to represent the tissue microstructure itself rather than just the signal, which allows for a more biologically meaningful interpretation of the model parameters (Jelescu and Budde 2017; Jelescu, Palombo, et al. 2020). The key idea is to model the different tissue environments relevant to diffusion in order to capture their specific diffusion properties more accurately. In practice, three main environments are usually considered: the *intra-axonal* compartment, the *extra-axonal* compartment and the *CSF* compartment (cf Section 2.1).

In this section, we will go over some very commonly used models in the community focusing more on the Stick-Zeppelin-Ball model as it is one of the most common as well as the model used for the filtering of tractograms with COMMIT in Chapter 7. We will quickly go over CHARMED, AxCaliber, ActiveAx and NODDI as they are highly relevant in the community but will not be used later in this manuscript.

2.3.1 CHARMED: Composite hindered and restricted model of diffusion

In (Assaf and P. J. Basser 2005), the authors democratized biophysically informed diffusion models that aim to explain the diffusion within tissues based on the physical features, laying the foundation for a new generation of models. More specifically, they introduced capturing non-Gaussian diffusion effects by distinguishing *restricted* and *hindered* diffusion compartments. To model the restricted diffusion happening inside the axons, they used sticks, i.e. tensors with negligible radial diffusivity. The modeling of the hindered compartment, corresponding to the diffusion of water molecules around the axons in the extra-axonal space, was performed using a zeppelin, which represents anisotropic Gaussian diffusion. This model captures the direction-dependent hindered diffusion in the extra-axonal space without explicitly modeling each axon individually.

The signal corresponding to a voxel with a volume fraction f for the intra-axonal compartment is then defined by:

$$S(b, \mathbf{g}) = S_0(fS_{restricted}(b, \mathbf{g}) + (1 - f)S_{hindered}(b, \mathbf{g})) \tag{2.43}$$

where S_0 corresponds to the signal without diffusion-weighting, b the b-value, $\mathbf{g}$ the diffusion-sensitizing gradient applied and $S_{restricted}$ (resp. $S_{hindered}$) is the signal generated by the restricted (resp. hindered) compartment. For this model, we can consider more than one restricted or hindered compartments to better fit the underlying microstructure

of the voxel.

2.3.2 AxCaliber/ActiveAx

In Assaf, Blumenfeld-Katzir, et al. (2008), the authors extended CHARMED to include the ability to vary axon diameters. In doing so, they retained the two compartments assumption: an intra-axonal compartment, describing restricted diffusion within axons, modeled as impermeable cylinders of fixed radius in CHARMED, or following a distribution of cylinder radii in AxCaliber, and an extra-axonal compartment, modelling hindered diffusion between axons. The overall signal attenuation is still given by Equation 2.43. However, the intra-axonal signal is now computed as a weighted sum of signals from cylinders of different radii, reflecting the distribution of axon sizes in the tissue, and can be resolved by:

$$S_{restricted}(b, \mathbf{g}) = \int_0^\infty P(r) S_{cylinder}(b, \mathbf{g}, r) dr \tag{2.44}$$

where $S_{cylinder}(b, \mathbf{g}, r)$ is the signal generated by a cylinder of radius r and $P(r)$ is the distribution of axon diameter.

Extensions of this model have been developed over the years like ActiveAx (Alexander et al. 2010) where an additional compartment to model isotropic diffusion, accounting for CSF, was considered, another modeling diffusion in small compartment like glial cells as well as several optimizations were made, especially on the acquisition protocol.

2.3.3 The Stick-Zeppelin-Ball model

T. Behrens et al. (2003) proposed an alternative to the diffusion tensor model with the Stick-Ball model that can account for more than one fiber direction within the voxel and for isotropic diffusion. This model was also able to accommodate for a fraction of the voxel where the diffusion is assumed to be isotropic. Similarly, Assaf and P. J. Basser (2005) proposed a biophysically informed model, CHARMED, presented previously, that allowed for describing both restricted and hindered diffusion, connecting the signal directly to the tissue features. This idea behind these models was extended in Panagiotaki et al. (2012) to 47 different models, including the Stick-Zeppelin-Ball model.

For the Stick-Zeppelin-Ball model, three types of compartments are considered. The signal is then modelled by:

$$S(b, \mathbf{g}) = S_0(f_{stick}S_{stick}(b, \mathbf{g}) + f_{zeppelin}S_{zeppelin}(b, \mathbf{g}) + f_{ball}S_{ball}(b)) \tag{2.45}$$

with

$$f_{stick} + f_{zeppelin} + f_{ball} = 1 \tag{2.46}$$

where b is the b-value, $\mathbf{g}$ is the gradient direction, f_{stick}, $f_{zeppelin}$ or f_{ball} correspond to the volume fraction of the compartment and S_{stick}, $S_{zeppelin}$ or S_{ball} correspond to the signal from the associated compartment.

In this model, the three compartments considered are the intra-axonal compartment, the extra-axonal compartment and an isotropic diffusion compartment. For the intra-axonal compartment, the diffusion is considered highly anisotropic in the direction of the fiber. Here, the intra-axonal compartment is modeled using the stick model from T. Behrens et al. (2003). Its signal is given by:

$$S_{stick} = \exp\left(-b\mathbf{g}^T\mathbf{D}_{stick}\mathbf{g}\right) \tag{2.47}$$

where b is the b-value, $\mathbf{g}$ is the diffusion gradient and D_{stick} is the diffusion tensor associated for the stick, given by:

$$\mathbf{D}_{stick} = d\mathbf{n}\mathbf{n}^T \tag{2.48}$$

where d is the diffusivity and $\mathbf{n}$ is the fiber direction. The extra-axonal compartment, an environment with hindered diffusion, is here modelled by a zeppelin (Alexander 2008). The signal is given by:

$$S_{zeppelin} = \exp\left(-b\mathbf{g}^T\mathbf{D}_{zeppelin}\mathbf{g}\right) \tag{2.49}$$

where b is the b-value, $\mathbf{g}$ is the diffusion gradient and $\mathbf{D}_{zeppelin}$ is the diffusion tensor associated with the zeppelin defined by:

$$\mathbf{D}_{zeppelin} = ((d_{||} - d_{\perp})\mathbf{n}\mathbf{n}^T + d_{\perp}I) \tag{2.50}$$

where $d_{||}$ (resp. $d_{\perp}$) is the diffusivity parallel (resp. perpendicular) to the principal direction $\mathbf{n}$. The third compartment allows for isotropic diffusion in the tissue which can happen in the cerebrospinal fluid for example. Here, it is modelled by a ball for which the

signal is given by:

$$S_{ball} = \exp\left(-b\mathbf{g}^T\mathbf{D}_{ball}\mathbf{g}\right) \tag{2.51}$$

where b is the b-value, $\mathbf{g}$ is the diffusion gradient and $\mathbb{D}_{ball}$ is the diffusion tensor associated with the ball and is defined by:

$$\mathbf{D}_{ball} = d\mathbf{I} \tag{2.52}$$

where d is the diffusivity and $\mathbf{I}$ is the identity matrix.

2.3.4 NODDI: Neurite Orientation Dispersion and Density Imaging

In Zhang et al. (2012), the authors presented a similar model using three compartments with their acquisition protocol. This model aims at estimating the complexity of dendrites and axons using markers other than the standard fractional anisotropy (FA). For this model, the intra-cellular compartment is still defined by a set of sticks, defined as cylinders with null-radius. For this compartment, sticks can go from highly parallel to highly dispersed allowing for a distribution of orientation that will be useful to define an orientation dispersion index (OD) that is used as a parameter of interest when processing the data. The extra-cellular compartment is used to model the hindered diffusion in the space surrounding neurites. The last compartment allows for the modeling of isotropic Gaussian diffusion to account for the cerebrospinal fluid (CSF). The general equation of the signal is given by:

$$S(b, \mathbf{g}) = S_0(v_{ic}S_{ic}(b, \mathbf{g}) + v_{ec}S_{ec}(b, \mathbf{g}) + v_{iso}S_{iso}(b)) \tag{2.53}$$

with

$$v_{ic} + v_{ec} + v_{iso} = 1 \tag{2.54}$$

where v_{ic} (resp. v_{ec} and v_{iso}) is the volume fraction associated with the intra-cellular (resp. extra-cellular and isotropic) compartment and S_{ic} (resp. S_{ec} and S_{iso}) is the signal originated from the intra-cellular (resp. extra-cellular and isotropic) compartment. In this model, four main parameters of interest can be studied. The first is the fractional anisotropy (FA), the second is the orientation dispersion index OD and the last two are

the volume fraction associated with the intra-cellular compartment v_{ic} and the isotropic compartment v_{iso}.

2.4 Advantages and limitations of mathematical and biophysical models

Both types of models presented exhibit strengths as well as drawbacks. While mathematical representations of the signal allow efficient estimation of several parameters of interest while keeping little to no assumption about brain tissue microstructure, they are unable to directly relate these parameters to the underlying tissues. On the other hand, biophysical models are designed to estimate parameters directly related to the tissue microstructure, such as the neurite density or orientation dispersion. However, they rely heavily on numerous and often strict assumptions about the microstructure, which can lead to biased or misleading information when these assumptions are violated.

In light of those limitations, hybrids models like DIAMOND (Scherrer et al. 2016) are designed. They aim at combining the flexibility and reliability of signal representations from mathematical models with the interpretability of compartment models by modeling mixture of microstructural environments, with different orientations, anisotropies or volume fractions. These methods can capture intra-voxel heterogeneities better than biophysical models with more flexibility but remain parameter-heavy with potentially more needs in terms of acquisition constraints and their interpretability are still somewhat abstract compared to biophysical models.

2.5 Signal simulation

While models get more precise and allow for a better description of brain tissue, the question of validation should not be overlooked and the question of ground truth is prevalent. Obtaining a ground truth for *in vivo* MRI is impossible, hence, numerical simulations with known ground truth is needed for validation. Two main methods are used for the simulation, one uses Bloch-Torrey equations, the other uses Monte-Carlo simulations.

In the case of Monte-Carlo simulations, such as those in Camino (Cook et al. 2006) or the Monte-Carlo Diffusion and Collision simulator (MCDC) (Rafael-Patino et al. 2020),

the random walk of water particles inside a digital tissue is modelled. It starts with thousands or millions of *spins* corresponding to K particles. These particles undergo a diffusion gradient, $\mathbf{g}(t)$, then the accumulated phase, ϕ_k, for each spin is computed:

$$\phi_k = \gamma \int_0^{TE} \mathbf{r}_k(t) \cdot \mathbf{g}(t) \mathrm{d}t, \tag{2.55}$$

where $\mathbf{r}_k(t)$ is the trajectory of particle k. The estimated signal is computed as the resulting contribution:

$$S = \frac{1}{K} \sum_{k=1}^{K} \exp(-i\phi_k). \tag{2.56}$$

These simulations can be used for any geometry and can be relatively easy to interpret in terms of physical effect. However, Monte-Carlo simulations can be quite expansive in terms of computational resources and time.

Another way to perform diffusion-weighted simulations is to solve the Bloch-Torrey equation in specific cases, such as with SpinDoctor (Li et al. 2019) or MISST (Drobnjak, Siow, and Alexander 2010). In these approaches, the equation is solved under very specific and restricted conditions that make a numerical solution feasible. These conditions typically include simplified geometries like cylinders or spheres, homogeneous diffusion coefficients and relaxation times within each compartment, well-defined boundary conditions such as impermeable membranes and simplified gradient waveforms. The equation is discretized in space and time using strong numerical solvers to approximate the solution. While this method is highly precise for simple geometries, it is computationally demanding and cannot be applied directly to more complex or realistic tissue structures, such as anatomically detailed white matter models.

2.6 Digital phantoms and mesh models

When using simulation, the ground truth can be fixed and perfectly known. Several methods can be used to generate these ground truths depending on the user's needs. Some methods aim at understanding brain's microstructure hence need to be more realistic, while some aim at investigating brain connectivity and focus more on describing fiber bundles than detailed microstructures.

To validate connections at the scale of the whole brain, digital phantoms can be created using diverse methods. Phantomas (Caruyer, Daducci, et al. 2014) and FiberFox

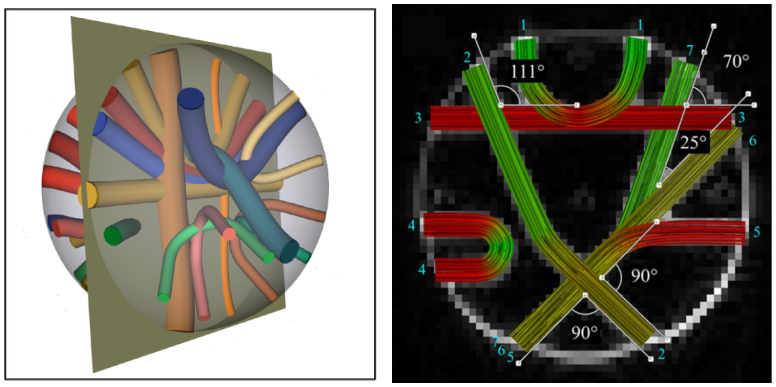

Figure 2.7 – Examples of digital phantoms describing whole-brain connectivity between regions of interest. (left) Digital phantom generated using Phantomas (Caruyer, Daducci, et al. 2014) for the 2nd HARDI reconstruction challenge at ISBI 2013. (right) Example of the FiberCup phantom generated using FiberFox in (Peter F. Neher et al. 2014).

(Peter F. Neher et al. 2014) are examples of methods that allow the easy generation of structurally realistic digital phantoms that can be used for whole-brain-scale simulations. These methods allow for the simple definition of bundles configuration that can be hard to discriminate such as bending, crossing or even kissing fibers. Examples of phantoms generated using these methods can be found in Figure 2.7. In Phantomas, each bundle of fibers is represented by a tube in three-dimensional (3D) space using waypoints to define points of the centerline and the bundle is interpolated using these points. In FiberFox, the authors keep this idea of having a tube containing the bundle, however, they define their waypoints as 2D ellipses in order to allow for fanning configuration. Then, they use the generated bundle as boundaries to generate a number of fibers in the bundle. The generated phantom is not represented by the collection of fiber bundles generated but rather by their fibers.

While a fairly simple description of fiber bundles can be enough to validate results at the scale of the whole brain, when trying to understand microstructure configurations, phantoms need to rely heavily on histology results to describe as accurately the microstructure. Several methods have been developed in the last few years. Here, we will only present three of them starting with the one used later in Chapter 6, CACTUS (Villarreal-Haro et al. 2023), then MEDUSA (Ginsburger et al. 2019) and finally ConFiG (Callaghan et al. 2020). Examples of mesh models and digital phantoms generated by these three methods can be found in Figure 2.8.

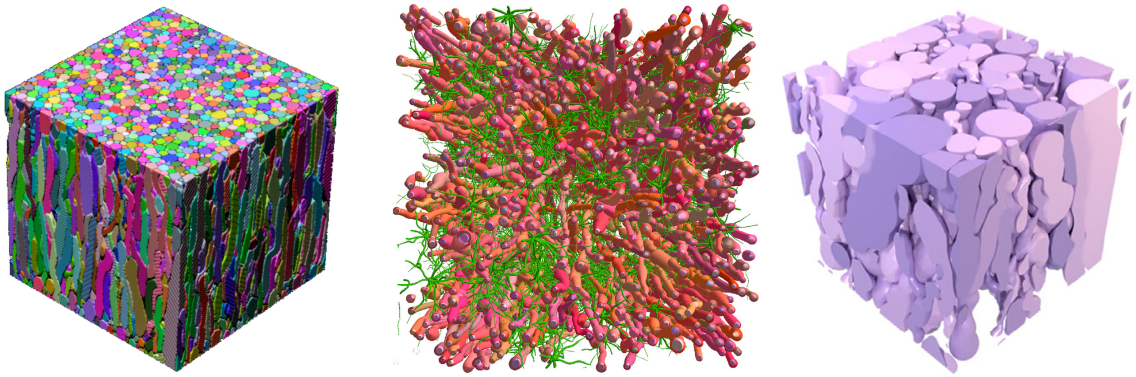

Figure 2.8 – Examples of digital phantoms describing complex and realistic microstructure at the size of a voxel or under. (left) Figure from (Villarreal-Haro et al. 2023) of a digital phantom generated using CACTUS. (middle) Figure from (Ginsburger et al. 2019) of one phantom generated using MEDUSA. (right) Figure from (Callaghan et al. 2020) of one phantom generated using ConFiG.

CACTUS (Villarreal-Haro et al. 2023) aims at defining mesh models representing a voxel of very realistic white matter microstructure with properties of interest. This method is a three-step process that allows for the generation of three dimensional substrates with a very high intra-axonal volume fraction that can go up to 95% while maintaining fiber complexity. The first step is an initialisation step where bundles of fibers are created within the voxel with specific angular dispersion and bundle crossings. The second step, called *joint fiber optimization*, aims to remove overlapping by adapting fiber trajectories and by inducing radii variation locally. The third step is a growth step that allows for very high fiber densities while maintaining the radius distribution specified by the user.

MEDUSA (Ginsburger et al. 2019) uses the representation of each microstructural item as a sphere to generate a substrate. More specifically, the first step of the method is to generate a set of overlapping spheres to generate microstructure of interest such as fibers, astrocytes, oligodendrocytes, neurons. Taking the example of a fiber, the starting point is randomly selected on a sphere and the fiber grows in the direction selected according to parameters given by the user. Then, the second step of this method is to add features of interest such as tortuosity, variation of radii or even a myelin sheath. Once every microstructural item of interest is created, they are fed to a collision solver that uses repulsion force to displace the items until they no longer overlap or are stopped by a user-defined criterion to resolve impossible convergence. This method can also adapt to grey matter microstructures.

In the case of ConFiG (Callaghan et al. 2020), the authors aim to generate the substrate by growing fibers one by one mimicking their biological development using a cost function to give cues similar to those given through chemical cues in biology. The first step of this method is to generate a starting point for every fiber while respecting user-defined targets in terms of diameter distribution and density on a face of a cube. Then, associated end-points are generated following the guidelines of the user in terms of orientation distribution. Then, nodes called *growth nodes* are placed in the space to encode the information of occupation in their associated regions in order to avoid having a collision detection mechanism later in the process. The growth of fibers can now start. Fibers are grown one by one and are randomly selected in the set of remaining fibers to grow. The fiber grows in a direction that is given by a cost function inspired by biological cues. At each step of the growth, fibers avoid already existing ones and nodes are updated to match the trajectory of the growth. Once every fiber is grown, a 3D fiber mesh is generated and can then be used for simulations.

Many teams work on improving phantoms to create more complex and realistic ground truth, thereby improving our understanding of the human brain. Many challenges undermine our ability to create extremely realistic ground truth, whether it is for microstructure models at the voxel size or brain-sized models with microstructural information. Those challenges include very high computational cost when doing the simulation, lesser known brain microstructures depending on the region due to histology challenges, providing only tiny volumes of brain tissue at a time or even physical and biological challenges due to the complexity of brain tissue including exchanges between compartments, heterogeneities, myelin effects or even pathological tissues.

2.7 Grey matter microstructure models

Thanks to many innovations over the years, grey matter can now be studied in much more details. Studying grey matter microstructure in the brain is critical for several disorders such as Alzeimer's disease or some psychological disorders as they could provide several biomarkers for diagnosis, progression or treatment response.

This leads to a growing need in modelling grey matter. Understanding grey matter present many challenges, some very different from white matter, including a much more complex organisation in terms of alignement, the presence of many different structures like cell body or dendrites, or even a greater amount of water exchanges between structures.

Many assumptions used for the modelling of white matter cannot be used when working with grey matter. Specific biophysical models have been proposed, including more compartments as well as exchanges mechanisms such as SANDI (Palombo et al. 2020) or NEXI (Jelescu, de Skowronski, et al. 2022). To study grey matter, there is also the need to develop phantoms or mesh models, just as was done for white matter in order to validate results. Models such as ConCeG (Aird-Rossiter et al. 2024), inspired by ConFiG (Callaghan et al. 2020) have been proposed to fill that need.

2.8 Conclusion

Modeling white matter microstructure in the brain is a very large and complex problem. Several models describing white matter brain tissues have been proposed over the years, some relying on mathematical representation of the signal while others rely on more complex biophysical assumptions of the brain tissue. While both have advantages, they have several limitations such as the difficulty to interpret results from signal representation in terms of tissue properties or violated assumptions from biophysical models leading to misinterpretation of parameters. Some hybrid models as well as several improvements and new models have been proposed in the last few years to alleviate some of these limitations.

On top of this, to properly validate results on white matter, the need for proper ground truth has been prevalent, leading to the use of realistic simulations as well as the development of numerous digital phantoms and mesh models. More recently, studying grey matter microstructure has started, creating the need for similar tools either as model, as phantom or even developing adapted simulators.

Chapter 3

Acquisition strategies

The choice of the acquisition scheme in diffusion MRI is critical as it directly determines the type of quality of information that can be extracted from the measured signal. In this context, an acquisition scheme refers to the set of parameters defining the diffusion-weighted measurements, including the diffusion gradient directions, the b-values and the timing parameters of the sequence such as the echo-time (TE). Different diffusion models and analysis methods rely on specific features of the signal and therefore require different types of acquisitions. For example, diffusion tensor imaging (DTI) relies on measurements at moderate b-values and multiple gradient directions to estimate anisotropy while more advanced approaches such as diffusion kurtosis imaging (DKI) require multiple b-values, often including higher b-values, to capture non-Gaussian diffusion effects. Other techniques may also rely on specific gradient waveforms to probe additional microstructural properties. As a result, the acquisition scheme must be carefully designed to provide sufficient sensitivity to the quantities of interest. At the same time, practical constraints such as the total acquisition time and the signal-to-noise ratio must be taken into account. This is particularly important in clinical and in vivo settings where scan duration is limited. Designing an acquisition scheme therefore requires balancing sensitivity to microstructural features with feasibility and robustness of the measurement.

In this chapter, we aim to describe acquisition protocols and their ability to capture microstructural information about tissue, as well as to introduce optimization strategies. We first focus on the selection of the diffusion-weighting gradient directions and strategies for uniform sampling on a single shell. Then we turn to the design of multishell acquisition schemes, which allow for richer exploration of diffusion behavior across multiple b-values. We then present the evolution from classical acquisition schemes like PGSE (Stejskal and Tanner 1965) to more advanced acquisition strategies such as double or triple diffusion encoding and describe the specific schemes used in this work: b-tensor encoded acquisition which is a part of the Q-space trajectory imaging (QTI) framework. Finally, we review commonly used methods to optimize the acquisition design, including the Cramér-Rao

lower bound (CRLB). These techniques aim to maximize the information content of the acquisition while remaining compatible with practical constraints.

3.1 Diffusion gradient direction selection

In diffusion MRI, diffusion-sensitizing gradients can be applied along different spatial directions. Each measurement probes the displacement of water molecules along the direction of the applied gradient, resulting in a direction-dependent signal attenuation. Acquiring measurements along multiple directions is therefore essential to capture the anisotropy of diffusion in biological tissues and the selection of these gradient directions is critical. An inadequate sampling on the sphere can introduce an angular bias, meaning that some orientations are preferentially sampled while others are under-represented (D. Jones, Horsfield, and A. Simmons 1999). This can lead to biased estimation of directional quantities such as fiber orientations or scalar metrics derived from the signal like the fractional anisotropy (FA).

A common objective is to obtain a uniform distribution of directions on the unit sphere. Several strategies have been proposed to achieve this. One widely used approach is based on *electrostatic repulsion*, where each direction is modeled as a charged particle that repels the others until a stable configuration is reached (D. Jones, Horsfield, and A. Simmons 1999). These numerical optimizations can however be computationally expensive and too time consuming when trying to generate a great number of directions (typically several tens to hundreds directions). Deterministic sampling schemes have also been proposed, such as latitude-based constructions, which are more efficient for generating large numbers of directions (Koay 2011).

3.2 Diffusion weighting and acquisition parameters

In addition to the selection of the diffusion-sensitizing gradient directions, the design of a diffusion MRI acquisition scheme relies on several parameters that control the strength and timing of diffusion encoding. Among these the diffusion weighting, commonly summarized by the b-value, plays a central role. The b-value depends on the properties of the diffusion gradients, namely their amplitude G, their duration δ and their time-interval Δ (Stejskal and Tanner 1965). This b-value determines the sensitivity of the MR signal to water molecule displacement. Low b-values, which are generally below 1000 $\mathrm{s\,mm^{-2}}$,

emphasize signal contributions from relatively free diffusion, such as in cerebrospinal fluid, whereas higher b-values increase sensitivity to hindered and restricted diffusion in complex tissue environments, such as fiber crossings (D. K. Jones 2010).

Early diffusion MRI acquisition typically relied on a single non-zero b-value in addition to a $b = 0$ image, corresponding to an image without diffusion weighting. These are known as *single-shell* acquisitions. Such acquisitions are sufficient for techniques like diffusion tensor imaging (DTI), which assume a Gaussian diffusion process. However, they are limited in their ability to capture more complex diffusion behaviors such as non-Gaussian effects or the presence of multiple compartments or fiber populations. To overcome these limitations, *multishell* acquisition schemes have been introduced. In those schemes, measurements are acquired at multiple non-zero b-values, each defining a shell in q-space. These acquisition schemes support more advanced analysis of the signal using techniques like DKI (Jensen, Helpern, et al. 2005) or NODDI (Zhang et al. 2012).

The multishell acquisitions also require an optimized choice of the diffusion gradient directions. While selecting directions for a single shell acquisition focuses on the generation of uniformly distributed directions on the shell, multishell acquisition benefits from optimizing those directions across shells. This can be achieved using geometric constructions using the vertices of regular polyhedra like an icosahedron or dodecahedron, which provide approximately uniform sampling of the sphere (C. Westin, Pasternak, and H. Knutsson 2012). An example of a set of directions selected using this method can be seen in Figure 3.1. More flexible methods rely on numerical optimization where the set of directions is obtained by minimizing a cost function that enforces uniformity on the sphere and across multiple shells, ensuring uniform sampling within each shell (Caruyer, Lenglet, et al. 2013). An example of a set of directions on three shells using this approach can be seen in Figure 3.2.

In addition to the b-value and gradient directions, other acquisition parameters also influence the measured signal. In particular, the diffusion time Δ determines the spatial scale over which molecules are probed while the gradient duration δ and amplitude G affect both the achievable b-value and temporal structure of the encoding. The echo time (TE) also plays an important role as it affects the signal attenuation. The link between the signal and the TE is given by this equation:

$$S(b, TE) = S_0 \exp(-bD) \exp(-\frac{TE}{T_2}) \tag{3.1}$$

where b is the b-value and D is the diffusion coefficient. Longer TE leads to increased

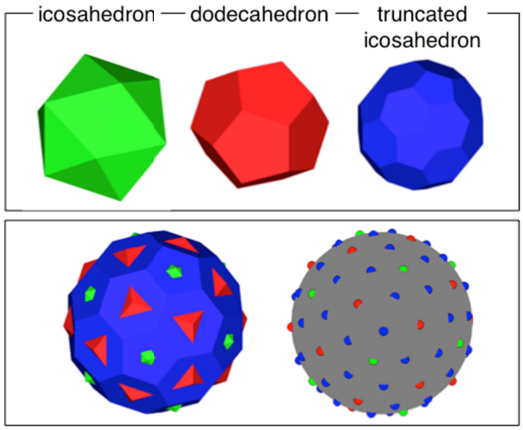

Figure 3.1 – The top row shows an icosahedron, a dodecahedron and a truncated icosahedron. The bottom row shows how they can be combined to form a uniform distribution of points on the sphere. Figure from C. Westin, Pasternak, and H. Knutsson (2012).

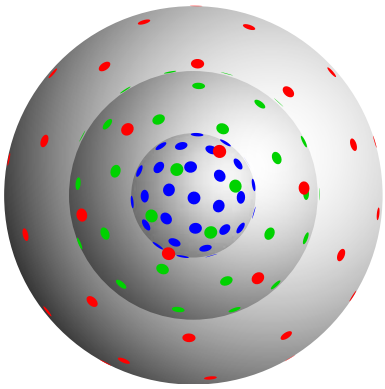

Figure 3.2 – Set of directions generated using the method presented in Caruyer, Lenglet, et al. (2013) with 30 points per shell and 3 shells. Figure from Caruyer, Lenglet, et al. (2013).

signal attenuation due to T_2 relaxation, impacting the signal-to-noise ratio. In practice, diffusion-weighted sequences often require a long TE due to diffusion gradients.

3.3 Advanced diffusion encoding

The diffusion-weighting gradients are at the very heart of the evolution of diffusion MRI over the years. Many improvements and new designs have been developed for 40 years thanks to both hardware improvements and the growing need of more expressive gradients to fit modeling needs, including for example Oscillating Gradient Spin Echo (OGSE) or multidimensional encoding.

3.3.1 Generalized gradient waveforms

The classical diffusion scheme is the Pulsed Gradient Spin Echo (PGSE) introduced by Stejskal and Tanner (1965). As described in Subsection 1.2.2, this sequence is based on the spin-echo sequence, to which a pair of diffusion-sensitizing gradients is added. Although still very used, the PGSE sequence is limited to rather long diffusion times - its *effective diffusion time* being $\Delta - \frac{\delta}{3}$ (see Figure 1.4 for the definition of δ and Δ). This led to the development of Oscillating Gradient Spin Echo (OGSE) which consists in sinusoidal or cosine gradient waveforms instead of rectangular gradient pulses. This effectively reduces the effective diffusion time τ to:

$$\tau \approx \frac{1}{\omega} \tag{3.2}$$

where ω is the frequency of the gradient. This gradient can be defined by:

$$g(t) = G \sin(\omega t) \tag{3.3}$$

where G is still the gradient amplitude. For the OGSE sequence, the expression of the diffusion weighted signal and the b-value changes slightly as follows:

$$b = \gamma^2 G^2 \frac{N\pi}{\omega^3} \tag{3.4}$$

where N is the number of oscillation cycles and:

$$S(b) = S_0 \exp(-bD(\omega)) \tag{3.5}$$

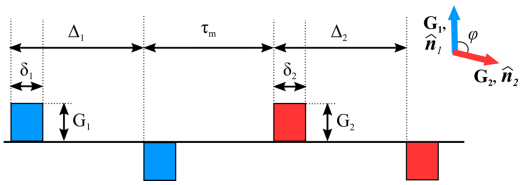

Figure 3.3 – Schematic representation of a double diffusion encoding sequence. Figure adapted from Henriques et al. (2021).

These gradients allow for a shorter effective diffusion time with higher oscillation frequency, leading to an improved sensitivity to restricted diffusion such as found in cells or axons. However, they require scanner with stronger and fast-switching gradients to be feasible. For both PGSE and OGSE, the diffusion-sensitizing gradient is applied in only one direction per measurement, these can also be referred to as single diffusion encoding (SDE) acquisitions. While OGSE allows for additional information to be extracted thanks to smaller effective diffusion times, it is still limited to resolve complex microstructures.

3.3.2 Multidimensional diffusion encoding

To overcome the limitation of SDE, more advanced strategies have been developed that rely on multiple diffusion encoding periods. One such appoach is *Double Diffusion Encoding* (DDE) introduced by Cory (1990). In this technique, two successive diffusion encoding blocks are applied, separated by a mixing time. Importantly, the corresponding gradients can be oriented along different directions, allowing the measurement of correlation between displacements along distinct axes. A schematic representation is shown in Figure 3.3. These acquisitions provide access to quantities that are not measurable with SDE alone such as the microscopic anisotropy that was presented in the previous chapter. They can also be sensitive to exchange processes between compartments for example due to membrane permeability (Henriques et al. 2021).

This concept can be further extended to *Triple Diffusion Encoding* (TDE), where three successive diffusion encoding periods are applied (Jensen and Helpern 2018). Such a sequence can be seen in Figure 3.4. These acquisitions provide increased sensitivity to complex microstructural geometries particularly in regions where multiple fiber populations coexist within a voxel.

The development of these multidimensional encoding strategies has been enabled by advances in MRI hardware, particularly in terms of maximum gradient amplitude and

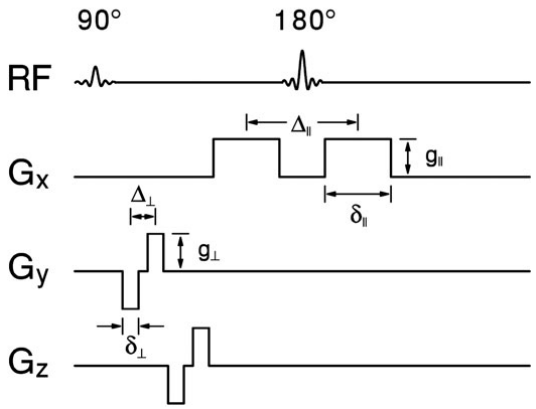

Figure 3.4 – Schematic representation of a triple diffusion encoding sequence. Figure adapted from Jensen and Helpern (2018).

slew rate. These improvements allow for more flexible and informative acquisition schemes providing better sensitivity to microstructure.

3.3.3 Q-space trajectory imaging (QTI) and b-tensor encoded acquisition

For most of this thesis, we will be using the Q-space trajectory imaging (QTI) framework introduced by C.-F. Westin, Hans Knutsson, et al. (2016). This framework is divided in two parts: modeling and encoding. The model used here is the Diffusion Tensor Distribution (DTD) model presented in the previous chapter (cf. 2.2.3). We will now focus on the second part, the encoding of the acquisitions.

In C.-F. Westin, Szczepankiewicz, et al. (2014) and Eriksson et al. (2015), the authors extended the framework of diffusion encoding by generalizing the b-value to the concept of b-tensor. The b-tensor, to be seen as a "diffusion measurement tensor", enable to represent arbitrary gradient waveforms. For instance, conventional diffusion encoding based on SDE corresponds to linear (or rank-1) b-tensors, while DDE corresponds to planar (or rank-2) b-tensors (Topgaard 2017).

Gradient waveforms can be represented in 3D using the gradient trajectory in space $\mathbf{g}(t)$ as seen in the second column of Figure 3.5. Using the gradient trajectory $\mathbf{g}(t)$, the time-dependent gradient waveform $\mathbf{q}(t)$ can be defined in q-space (cf. column 3 of Figure 3.5) as:

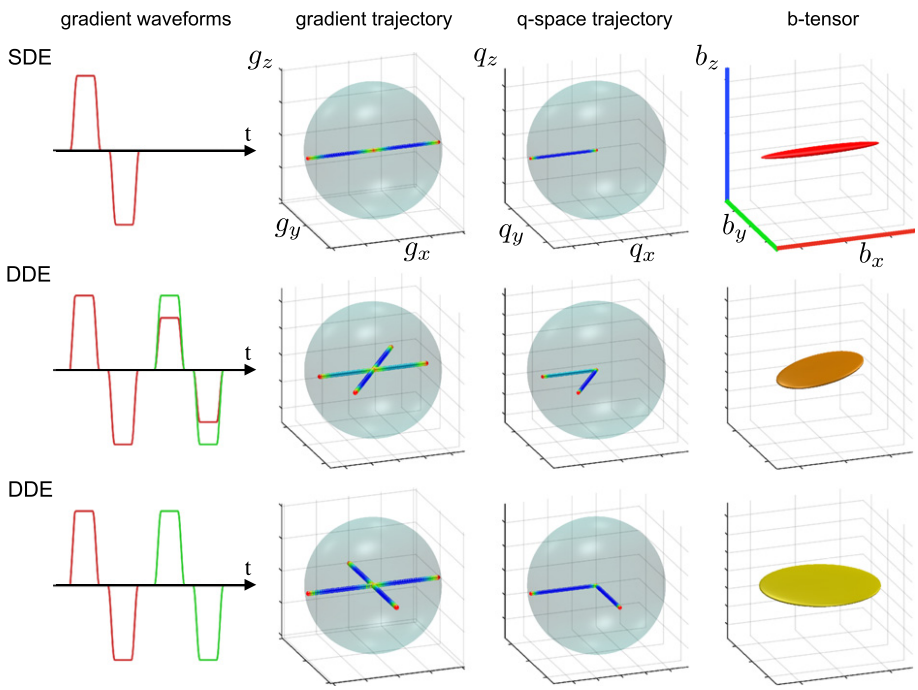

Figure 3.5 – Examples of three acquisitions with their gradient waveform in the first column, their trajectories in the gradient space in the second column and in q-space in the third, and their associated b-tensor in the fourth column. The first line corresponds to an acquisition using SDE. The second and third line correspond to two acquisitions using DDE. Figure from C.-F. Westin, Hans Knutsson, et al. (2016)

$$\mathbf{q}(t) = \gamma \int_0^t \mathbf{g}(t')dt' \tag{3.6}$$

where γ is the gyromagnetic ratio. From this, the b-tensor, also called b-matrix $\mathbf{B}$, can be defined as:

$$\mathbf{B} = \int_0^\tau \mathbf{q}(t)^{\otimes 2} dt \tag{3.7}$$

where τ is the echo-time and $\mathbf{q}(t)^{\otimes 2}$ is the outer product of $\mathbf{q}(t)$ with itself.

The b-value can be re-defined as the trace of the b-tensor, $b = Tr(\mathbf{B})$. In its principal axis system, the b-matrix can be represented by its three eigenvalues as:

$$\mathbf{B} = \begin{pmatrix} b_1 & 0 & 0 \\ 0 & b_2 & 0 \\ 0 & 0 & b_3 \end{pmatrix} \tag{3.8}$$

In the rest of the thesis, we will focus on b-tensors with cylindrical symmetry. In this can, the b-tensor can be described by two independent eigenvalues. In the principal axis system where the b-tensor is diagonal with eigenvalues b_1, b_2, and b_3, cylindrical symmetry corresponds to two of these eigenvalues equal such as $b_2 = b_3$. Here, $b_{||} = b_1$ and $b_\perp = b_2 = b_3$, where $b_{||}$ denotes the component of the b-tensor along its principal axis and $b_\perp$ the components in the orthogonal directions.

Using these eigenvalues, different b-tensor shapes can be defined as illustrated in Figure 3.6. When $b_\perp = 0$, they are called *linear b-tensor*. These can also be generated by classical SDE acquisitions. When $b_{||} > b_\perp > 0$, they are called *prolate b-tensor*. When $b_{||} = b_\perp$, they are called *spherical b-tensor* and can also be generated by TDE acquisitions. When $b_\perp > b_{||} > 0$, they are called *oblate b-tensor*. Finally, when $b_{||} = 0$, they are called *planar b-tensor*, which can also be generated by DDE acquisitions.

In order to implement b-tensor acquisitions, we need to design a gradient waveform to be played by the scanner. Several waveforms can generate the same b-tensor, hence going from a b-tensor to a waveform is not immediate. One method to generate an acquisition scheme with b-tensor encoding is to generate one waveform for a spherical b-tensor and rescale it anisotropically in order to generate any b-tensor shape of interest. The first step is to generate an efficient isotropic diffusion encoding. In Sjölund et al. (2015), the authors solve an optimization problem to generate efficient waveforms for any desired shape of the b-tensor. They maximize the b-value as it amounts in their framework to maximize

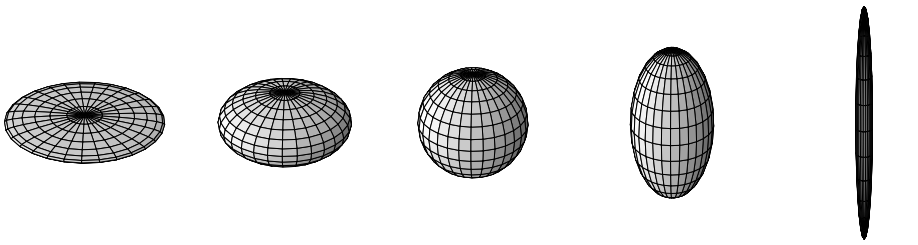

planar $b_{||} = 0$ | oblate $b_\perp > b_{||}$ | spherical $b_\perp = b_{||}$ | prolate $b_\perp < b_{||}$ | linear $b_\perp = 0$

Figure 3.6 – Examples of b-tensors with a cylindrical symmetry, showing an example for each of the five shapes defined by the relation between its eigenvalues.

the diffusion weighting under some sequence and hardware constraints:

$$
\begin{aligned}
\underset{\mathbf{q}, b}{\text{maximize}} \quad & b \\
\text{subject to} \quad & \int_0^\tau \mathbf{q}(t)\mathbf{q}(t)^T dt = b\hat{\mathbf{B}}, \\
& \mathbf{q}(0) = \mathbf{q}(\tau) = 0, \\
& \left.\frac{d\mathbf{q}}{dt}\right|_{t \in I_t} = 0, \\
& \left\| \frac{d\mathbf{q}}{dt} \right\| \leq \gamma G_{\max}, \\
& \left\| \frac{d^2\mathbf{q}}{d^2t} \right\|_\infty \leq \gamma R_{\max}, \\
& \int_0^\tau \left(\frac{dq_\alpha}{dt} \right)^2 dt \leq \nu \gamma^2 G_{\max}^2 \tau, \alpha = x, y, z
\end{aligned}
\tag{3.9}
$$

where $\mathbf{q}$ is the q-space trajectory, b is the conventional b-value, $\hat{\mathbf{B}}$ is a dimensionless, normalized b-tensor, τ is the desired echo time, γ is the gyromagnetic ratio, $G_{\max}$ is the maximal gradient amplitude, $R_{\max}$ is the maximum slew rate and ν is a scalar between 0 and 1 used to balance heat dissipation against diffusion encoding.

This method is the one used to generate waveforms for a spherical b-tensor when needed in this thesis work. Once this waveform is generated, it is modified by changing the amplitude of each direction to create the desired b-tensor shape (C.-F. Westin, Hans Knutsson, et al. 2016). An example of such modifications can be found in Figure 3.7.

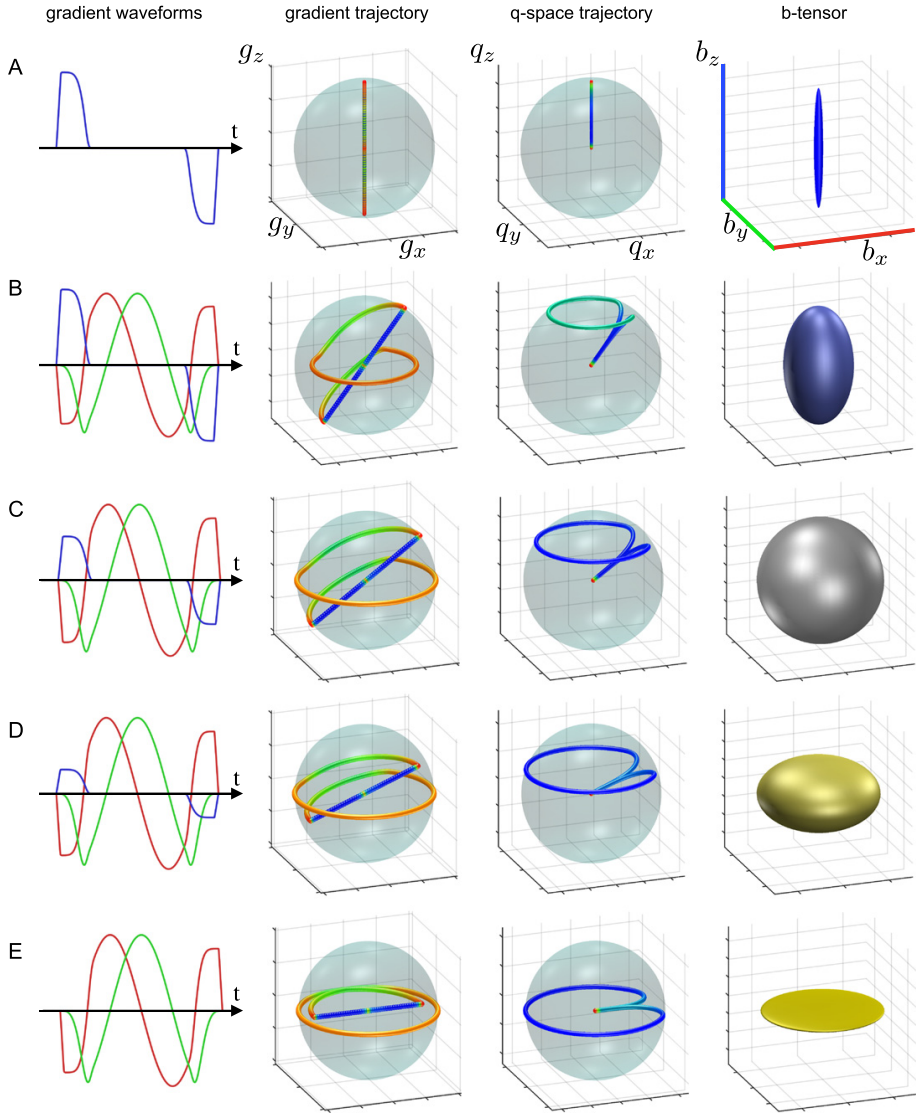

Figure 3.7 – Examples of gradient waveforms for each shape of b-tensor generated from an efficient isotropic diffusion encoding gradient (C). The first column shows the gradient waveforms. The second the associated gradient trajectory with color coding slew rate. The third is the associated gradient trajectory in q-space. The last one represents the associated b-tensor. On line (A) is an example of linear b-tensor, line (B) an example of a prolate b-tensor, line (C) shows an example of a spherical b-tensor, line (D) corresponds to an oblate b-tensor and finally line (E) illustrates a planar b-tensor. Figure from C.-F. Westin, Hans Knutsson, et al. (2016)

3.4 Protocol optimization strategies

The strategy for optimizing a dMRI acquisition protocol goes beyond selecting the diffusion gradients directions as presented in Section 3.1 and includes the configuration of a set of parameters ranging from Echo Time (TE) to gradient waveforms. Indeed, this is critical to ensure that the acquisition is as short as possible while still providing enough information on the microstructure based on the models and data analysis used to extract patient-related information. This need to optimize the acquisition scheme is reflected by the many works in the community addressing the problem. This is also the goal of my contribution in Chapter 5. This effort has also motivated community-driven benchmarks aimed at comparing different acquisition strategies under controlled conditions such as the MUDI challenge (Pizzolato et al. 2020). In this section, we will introduce the main methods that are currently used to propose optimized acquisition schemes tailored for the user need in term of sensitivity to models and applications.

3.4.1 Cramér-Rao lower bound (CRLB)-based optimization

A commonly used framework for acquisition optimization is based on the Cramér-Rao lower bound (CRLB), which provides a theoretical lower bound on the variance of any unbiased estimator. This framework can be used in diffusion MRI to predict the precision with which model parameters can be estimated from a given acquisition scheme. By computing the Fisher information matrix associated with the signal model, it is possible to evaluate how different acquisition parameters can affect the expected estimation uncertainty. The acquisition protocol can be optimized using several criteria such as the product of the variances or the determinant of the CRLB. This approach has been widely used for the design of MRI acquisition including in the context of tensor-valued encoding and q-space trajectory imaging (Morez et al. 2023).

3.4.2 Dictionary-based optimization

An alternative class of methods relies on dictionary-based strategies inspired by fingerprinting (Rensonnet et al. 2019; Truffet, Barillot, and Caruyer 2019). In this framework, a large set of signals is simulated for different parameter combinations, forming a dictionary. The acquisition scheme is then designed such that different parameter set produce distinct signal signatures. This can be achieved by minimizing correlations between dic-

tionary entries or by maximizing sensitivity to specific parameters. Such approaches can be particularly useful for complex models where analytical tools such as the CRLB may be difficult to apply.

3.4.3 Machine learning-based approaches

More recently, machine learning methods have been proposed to optimize diffusion MRI acquisition schemes. These approaches aim to learn optimal sampling strategies directly from data. For instance, recent work (Planchuelo-Gómez et al. 2024) is exploring the use of physics-informed learning frameworks to optimize the acquisition parameters selection procedure. These methods can be used to reconstruct missing measurements and predict non-measured signals. While these methods offer promising results, they typically require large training datasets and may be less interpretable than previously mentioned approaches. The use of physical models in the learning process can however improve this interpretability or its robustness.

3.5 Conclusion

Designing diffusion MRI acquisition schemes is a complex problem that involves multiple interacting factors. Several acquisition strategies have been proposed, ranging from simple single diffusion encoding approaches to more advanced multidimensional encoding schemes. While these methods provide increasing sensitivity to microstructural features, they also introduce challenges related to acquisition design, signal interpretation and practical constraints. As the choice of the acquisition parameters directly influences the information contained in the measured signal, the development of optimized acquisition strategies selection became significant in the community. This lead to the study of several approaches to generate acquisition schemes balancing sensitivity to the brain microstructure and practical constraints such as the acquisition time.

Chapter 4

Structural connectivity and tractography

The human nervous system is an extremely complex network with a great number of neurons, estimated at around 87 billions and an important number of connections, estimated at about a thousand trillions. The study of the human brain and its connections started in the 18th century with the dissection of fixed tissues. Major breakthroughs in the understanding of the connectivity of the human brain have been possible more recently with diffusion MRI, over the past 40 years. Using diffusion MRI allows for the extraction of information on the *connectome* as well as microstructure in vivo. When tractography algorithms were introduced, the connections of the human brain network started being described as an entire map of reconstructed white matter fiber pathways called *tracts*. These tractograms are used to describe the *structural connectivity* of the brain. As such, the goal is to get an accurate description of the network. To this end, approaches known as *quantitative tractography* have recently emerged. These incorporate microstructural information into tractography in order to produce accurate and reliable tractograms (Daducci and Schiavi 2025)

In this chapter, we will start by describing brain connectivity and how it is structured. Then, we will present how tractography is performed, starting by the estimation of the orientation distribution function (ODF). The ODFs are used to describe the principal directions of the diffusion within the voxel (Tuch et al. 2003; Tuch 2004; Wedeen et al. 2005). In continuation, we will briefly introduce the main types of tractography algorithms used in the community. Then, we will present filtering methods developed to adress the problem of false positive fibers while keeping as much accurate connections as possible. Finally, we will open to the use of multidimensional diffusion MRI in order to add microstructural information to improve tractography results.

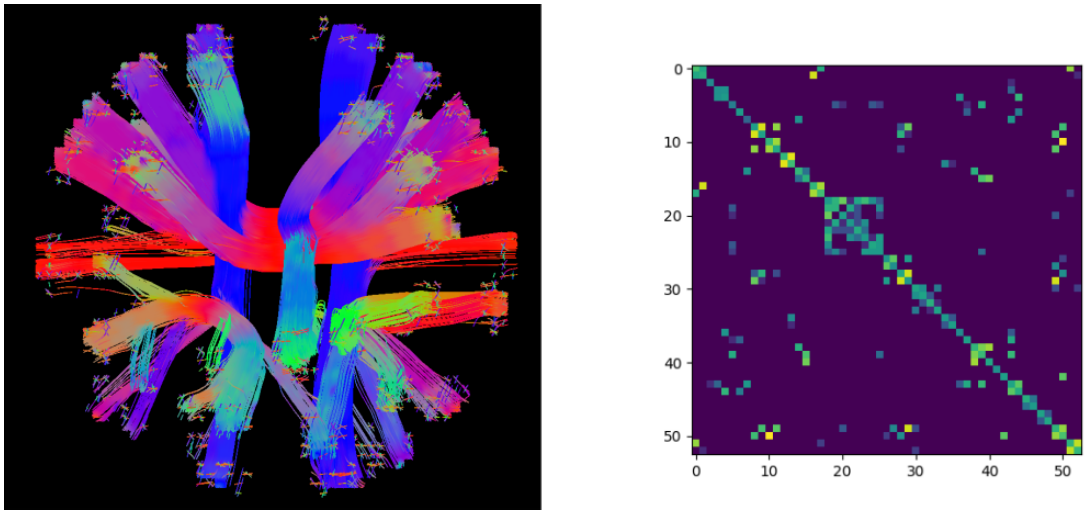

Figure 4.1 – (left) Tractogram generated with MRtrix3 of a digital phantom created with Phantomas (Caruyer, Daducci, et al. 2014). (right) Associated connectivity matrix where each region of interest corresponds to the starting or ending point of a bundle of the digital phantom.

4.1 Brain connectivity

In this chapter, we will focus on the description of the *structural connectivity* in the brain. This corresponds to the anatomical wiring of white matter fibers, axons and synaptic connections linking grey matter regions in the brain. The study of structural connectivity allows for a better understanding of the anatomical relation between regions of interest in the brain. In contrast, we can also study the *functional connectiviy*, relying on the synchrony of activation of brain regions, to understand its spontaneous activity.

The study of structural connectivity is useful to better understand brain development as well as neurological diseases, disorders or traumatic injuries. Indeed, changes in structural connectivity due to these medical conditions have been associated with several damages or degeneration over the course of the pathology. This structural connectivity can be seen as a network where the regions of interest in the grey matter can be represented by nodes and the white matter fibers can be represented by edges. Results are often represented as a connectivity matrix (cf Figure 4.1) where each value can correspond to an existing connection (binary connectivity) or a strength of connection (weighted connectivity) between two regions of interest.

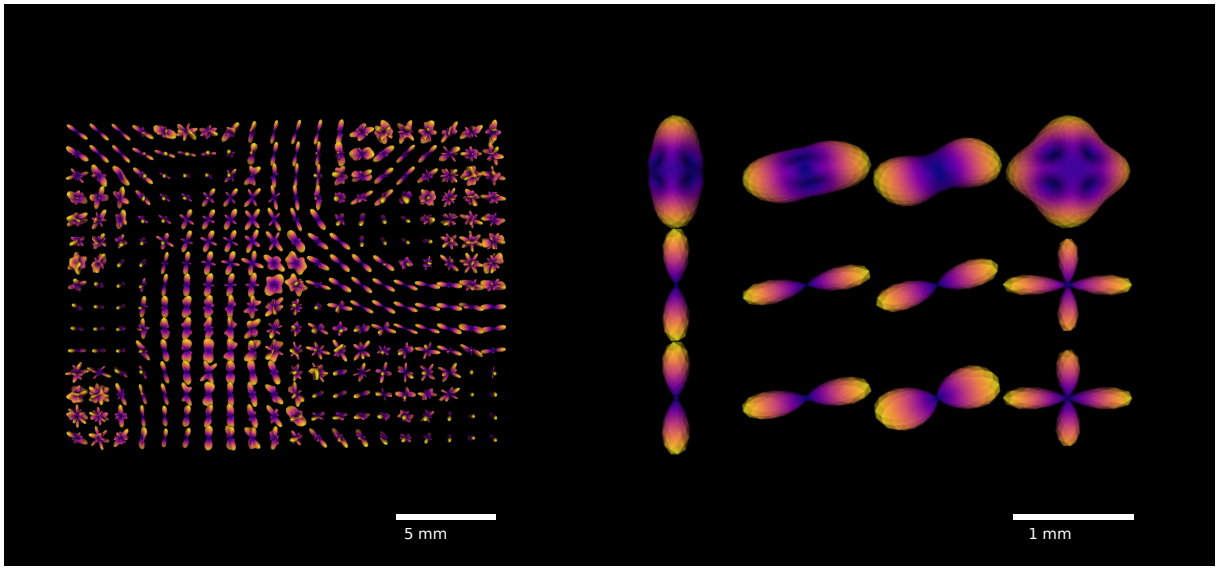

Figure 4.2 – Examples of dODFs estimated with the open-source library "Diffusion Imaging In Python" (DIPY) (Garyfallidis et al. 2014).

4.2 Orientation Distribution Function (ODF)

Studying the brain's structural connectivity with diffusion MRI implies relying on tractography algorithms to reconstruct tracts and bundles. As an input to the tractography algorithm, we need an estimate of the orientation distribution function (ODF) for each voxel. There exist two types of ODF: the diffusion orientation distribution function (dODF) and the fiber orientation distribution function (fODF).

The dODF (Tuch et al. 2003; Tuch 2004; Wedeen et al. 2005) is a description over the sphere of how likely water molecules are to diffuse in a given direction and is defined by:

$$dODF(\theta, \phi) = \int_0^\infty P(r, \theta, \phi) r^2 dr \tag{4.1}$$

where $P(r, \theta, \phi)$ is the diffusion propagator, which measures the probability of displacement of water molecules to a distance r in the direction given by θ and ϕ.

The second type of ODF, the fODF is a function describing the distribution of fiber density over the sphere. When using fODF, the diffusion signal can be expressed as:

$$S = fODF \otimes R \tag{4.2}$$

where R is the response function, representing the diffusion signal from a single coherent

fiber bundle, and $\otimes$ is the convolution operation. To estimate the fODF, a spherical deconvolution approach such as constrained spherical deconvolution (CSD) (Tournier, Calamante, and Connelly 2007) is used; alternatively, multi-compartments models and multishell data can be used with MSMT-CSD (Jeurissen et al. 2014).

Several improvements in the estimation of ODFs have been proposed, including sharpening methods to improve the angular resolution of peaks (Descoteaux, Deriche, et al. 2009; Erick Jorge Canales-Rodríguez et al. 2010) as well as encoding addition informations such as details of neighboring voxels (C. M. W. Tax et al. 2014) or anatomical priors (Wasserthal, Peter F Neher, and Maier-Hein 2018; Rheault et al. 2019; Durantel et al. 2025). Asymetrical ODFs (Cetin Karayumak, Özarslan, and Unal 2018; Poirier and Descoteaux 2024) have also started to be used in order to distinguish local configurations in complex areas such as intravoxel crossing, bending or kissing fibers, with the aim of improving tractography.

4.3 Tractography algorithms

Once ODFs are estimated, tractography algorithms can be used to estimate the trajectory of major fiber bundles. The resulting map of streamlines in the brain is referred to as a *tractogram* as illustrated in Figure 4.3. This process aims at identifying connections between regions of interest (ROI) defined by user, which may correspond to grey matter regions described in anatomical atlases (Desikan et al. 2006; Destrieux et al. 2010). In general, seeds points are used for the process as origin points of the algorithm, for instance placed at the interface between grey and white matter or in the white matter. From one seed, several fibers can be propagated, following the orientation given by ODFs. The construction of a fiber stops when a termination criterion is met, for instance when leaving white matter, or when the curvature exceeds a user-defined threshold.

The tractography algorithm can be *deterministic* or *probabilistic*; there also exist geodesic or global tractography, which we will not cover in the manuscript. For *deterministic* tractography (D. K. Jones, Andrew Simmons, et al. 1999; P. J. Basser, Pajevic, et al. 2000; Poupon et al. 2001), *seed* points are selected. They correspond to predefined positions in the brain from which *streamlines*, reconstructed fibers, are computed. These points can be either at the interface between white and grey matter, or can also be generated thorough all white matter voxels. All streamlines are computed step by step, following the direction given by ODFs in the white matter, until a stopping criterion is

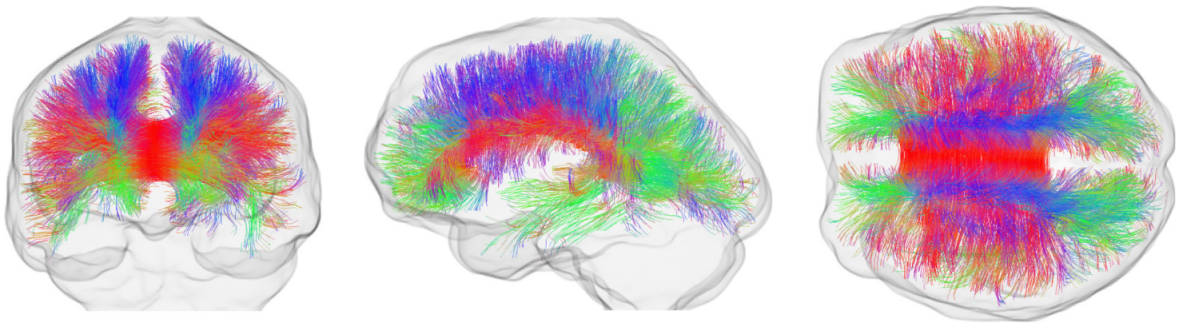

Figure 4.3 – Example of a tractogram of the human brain where the local streamline orientation is encoded by a color: red for left-right, green for antero-posterior and blue for superior-inferior.

met. In practice, from one point in white matter, the main direction of diffusion is followed to select the next voxel and direction of the streamline. Stopping criteria can be of different nature: for example, if a streamline enters a voxel containing grey matter or CSF but no white matter, or if the angle of the fiber is above a threshold, as it could correspond to the interface between grey and white matter.

In the case of *probabilistic* tractography (Parker, Haroon, and Wheeler-Kingshott 2003; T. Behrens et al. 2003), the computation of the path is different from the deterministic approach as it no longer relies on a single direction per voxel but it rather samples a distribution. The algorithm follows a similar pattern, starting with the selection of seed points. Then, a direction is randomly sampled from the distribution of potential directions within that voxel. This direction is followed into the next voxel. This process is repeated until one of the stopping criteria is met. One of the main difference with this tractography algorithm is the number of streamlines generated for each seed points, as here, one seed point can generate several streamlines.

These two algorithmic approaches produce different tractograms and have strengths and weaknesses. In the case of deterministic tractography, the tractogram is reproductible with very little variability in the fiber paths, however it is easily affected by noise and often misses tracts, especially in bottlenecks, fanning or crossing regions. On the other hand, probabilistic algorithms perform significantly better in those configurations but generate lots of false positive tracts and are very sensitive to tracking hyper-parameters and models (Maier-Hein et al. 2017).

4.4 Filtering

One of the main issue of tractography is the amount of false positive fibers reconstructed in the final tractogram. Several methods have been developed over the years to try to filter those false positives. One method is to use priors, especially anatomic priors to inform tractography in order to reduce these false positives. However, these methods are in general bundle-specific; besides the priors are in general inferred from a population of healthy volunteers, which limits their applicability for diffusion MRI in patients. Another approach is to filter the tractograms once generated, to keep only the streamlines that explain the signal. Such methods include COMMIT (Daducci, Dal Palù, et al. 2015; Schiavi et al. 2020), LiFE (Pestilli et al. 2014) and SIFT (Smith et al. 2013; Smith et al. 2015).

The core idea behind those techniques is to start with a direct model, predicting the diffusion MRI signal from a tractogram. Then, from a very large tractogram with millions of streamlines, streamlines are selected or weighted to match more closely the observed signal. In the case of SIFT, it is not directly the signal that is predicted, but rather the fODF amplitude in different directions. For the original method (Smith et al. 2013), streamlines over-representing fODF amplitudes are removed whereas the extension SIFT2 (Smith et al. 2015) weights them.

In COMMIT, the model explains the intra and extra axonal signal through the contribution of each streamline and relies on a dictionary, $\mathbf{A}$ (cf Figure 4.4). As the signal in each voxel is modeled a linear combination of the contribution of each compartment, namely the streamlines intersecting the voxel as well as additional components such as the extra-axonal space and cerebrospinal fluid (CSF), the signal can be expressed as a system of linear equations as follows:

$$\mathbf{y} = \mathbf{A}\mathbf{x} + \eta \tag{4.3}$$

where $\mathbf{A}$ is the dictionary encoding each potential contribution of each streamline or CSF compartment, $\mathbf{y}$ is the measured signal, η is a noise contribution and $\mathbf{x}$ encodes the weight for each potential streamline and CSF compartment. The filtering consists in estimating $\mathbf{x}$, providing a set of weighted streamlines and CSF compartments that explain the observed signal.

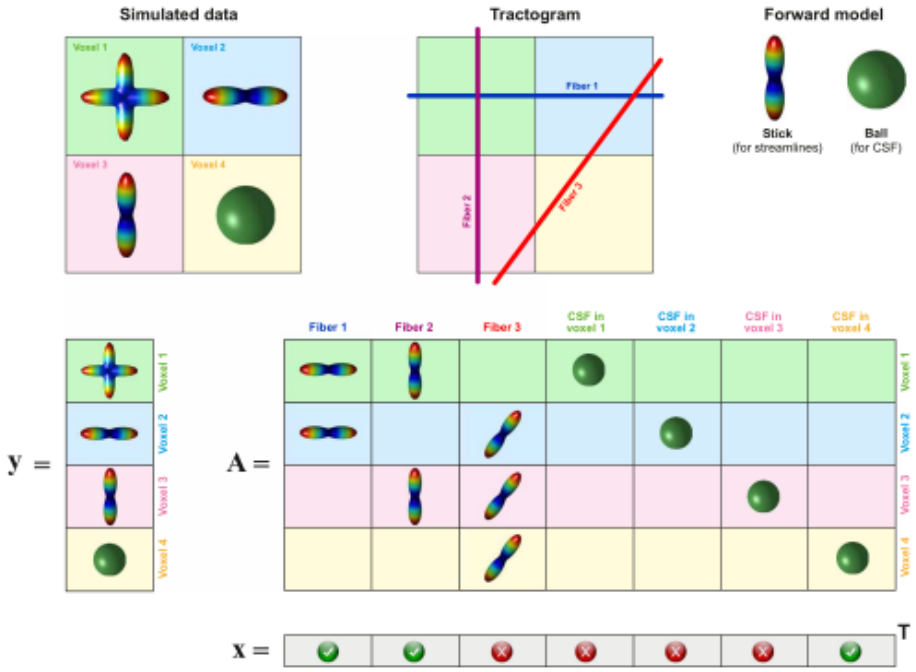

Figure 4.4 – Synthetic example to understand the principle of COMMIT using four voxels and a starting tractogram. The selected models are a stick for each streamline and a ball for each CSF compartment. y corresponds to the measured signal. Each value correspond to one voxel. A is the dictionary encoding each potential contribution for each streamline or CSF compartment. Each column corresponds to a potential contribution and each line to each voxel. x is the binary vector holding the information of which contribution is kept in the filtered tractogram. Figure from Schiavi et al. (2020)

.

4.5 Improving tractography using multidimensional dMRI

Tractography algorithms are improving rapidly, aiming at understanding more precisely the underlying structures within the brain as well as improving the detection of fiber tracts in complex regions. In order to hopefully increase the sensitivity to microstructure information, one of the proposed improvement is the creation of μ-ODFs (K. Magdoom et al. 2021; K. N. Magdoom et al. 2023). Theses new ODFs are derived from Diffusion Tensor Distributions (see subsection 2.2.3) and corresponds to the ensemble average of the FA and ODF over each micro-diffusion tensor within the voxel. These μ-ODFs show more peaks than regular ODFs (cf. Figure 4.5), improving reliability in complex configurations such as crossing or kissing regions (K. N. Magdoom et al. 2023). Tractography results reported by the authors indicate that these μ-ODFs can enhance the detection of fiber pathways in such challenging regions.

4.6 Conclusion

Describing the structural connectivity in the brain is a complex problem as the voxels are much larger than the fibers. Studying the connectivity is often done through the lens of tractography, such as deterministic or probabilistic tractography. These algorithms rely on orientation distribution function, characterizing the diffusion within the voxel. Over the years, tractography evolved to better disentangle complex structures such as kissing fibers, bending or fanning. On top of several complications to detect complex fiber pathways, tractography algorithms tend to generate a lot of false positive streamlines that need to be filtered. Several methods have been developed and improved over the last decade, relying on explaining either the signal or the ODFs profile by the measured signal, in order to reduce the amount of non-realistic false positive streamlines.

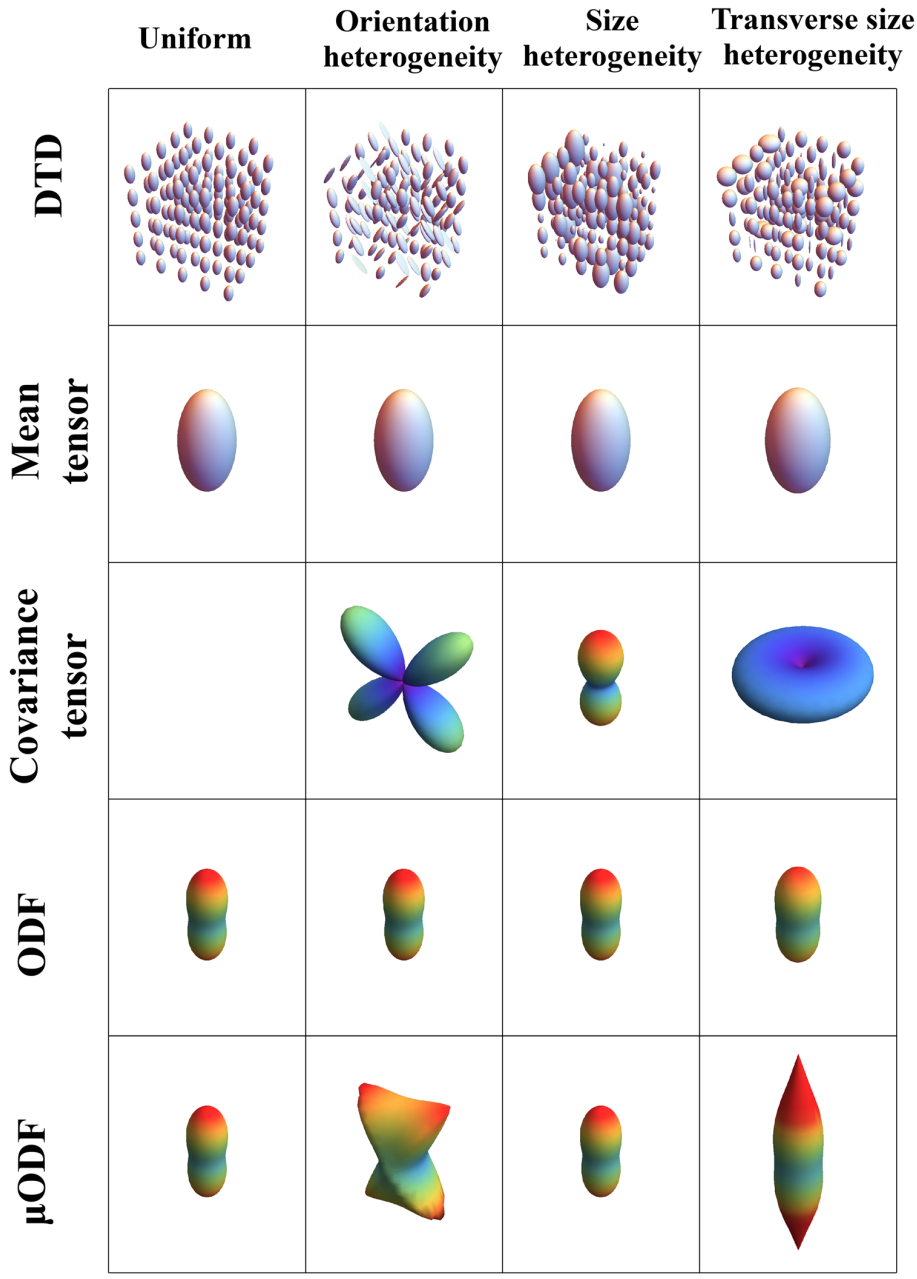

Figure 4.5 – Diffusion Tensor Distributions (first line) with their associated mean tensor (second line), covariance tensor (third line) and their ODF (fourth line) and μODF generated for different features of the DTD. Figure from K. Magdoom et al. (2021).

Part III

Contributions

Chapter 5

Optimization of acquisition schemes towards a better estimation of the microstructure parameters

Multidimensional diffusion MRI captures detailed properties such as anisotropy, kurtosis and orientation dispersion. This allows for the differentiation of microstructural features like fiber crossings, cellularity, and membrane permeability. Multidimensional dMRI has emerged as a powerful tool for studying complex biological tissues, offering valuable insights into neural connectivity, tumor microenvironments, and other structural properties in both research and clinical settings. Specifically, Q-space trajectory imaging (QTI) (C.-F. Westin, Hans Knutsson, et al. 2016) aims at reconstructing the parameters of diffusion tensor distribution (DTD) using b-tensor encoded acquisitions.

Acquisition optimization aims at improving the accuracy, precision, and efficiency of microstructural parameter estimation. By carefully selecting the MRI acquisition parameters—such as b-tensors and diffusion encoding directions—we can enhance the sensitivity of the measured signals to the underlying tissue features. The Cramer-Rao lower bound has been used as a measure of reference to evaluate the estimation accuracy when optimizing acquisition schemes (Alexander 2008; Truffet, Rafael-Patino, et al. 2020). This strategy has been recently extended to multidimensional dMRI (Morez et al. 2023).

One drawback of the Cramer-Rao lower bound is that it is computed locally, with respect to one point in the parameter space. In this chapter, we propose an alternative method inspired by fingerprinting (Rensonnet et al. 2019; Daducci, Erick J. Canales-Rodríguez, et al. 2015). This method is based on a dictionary of signals where each column corresponds to a DTD and each line to a b-tensor. From a predefined superset of acquisitions, our objective is to select the subset of b-tensors that best preserves the sep-

arability of the columns of the dictionary. We used simulations to assess the ability of the selected subset to yield accurate estimations of the microstructural parameters of interest: the microscopic anisotropy, the tensor size variance and the orientation parameter. Until section 5.3, the results presented correspond to those published in Bocquillon, Corouge, and Caruyer (2025c). In section 5.3 are the modifications we tested on the framework, namely adapting the number of directions in the superset to fit the b-tensor and testing a second metric to discriminate between our models.

5.1 Methods

In order to optimize the sensitivity of the acquisition to the microstructural parameters of interest, we designed an approach in several steps. The overview can be seen in Figure 5.1. First, we generated a superset of acquisitions from which we will select the best subset of b-tensors. Then, we generated a collection of DTD parameterized by the orientation parameter OP, the microscopic anisotropy μFA and the tensor size variance C_{MD}. The signal vector corresponding to each of these DTD constitutes the columns of our dictionary. Next, we optimized the choice of a subset of acquisitions to maximize the separability of the columns in our dictionary. Finally, we evaluated the accuracy of the reconstructed parameters from the acquisitions associated with the selected subset.

5.1.1 Acquisition superset

We constructed a superset of b-tensors, $\mathcal{S}$, containing every axisymmetric b-tensor shape with $b_{||}$ and $b_{\perp}$ in the range [0, 2000] $\mathrm{s\,mm^{-2}}$ divided into 60 intervals. We kept only those with a b-value under 2000 $\mathrm{s\,mm^{-2}}$ and ensuring a step of 100 in b-values. The principal axis of each b-tensor shape was rotated into 30 directions uniformly spread over the unit sphere, generated from D. Jones, Horsfield, and A. Simmons (1999). This results in a superset, $\mathcal{S}$, containing $n = 331$ unique b-tensor shapes, each rotated into 30 directions. The repartition of this superset on the two eigenvalues of the b-tensor can be seen in Figure 5.2.

5.1.2 Fingerprinting the parameter space

We generated a dictionary of signals, inspired by fingerprinting methods (Rensonnet et al. 2019), where each row corresponds to a b-tensor $\mathbf{B} \in \mathcal{S}$ and each column corresponds

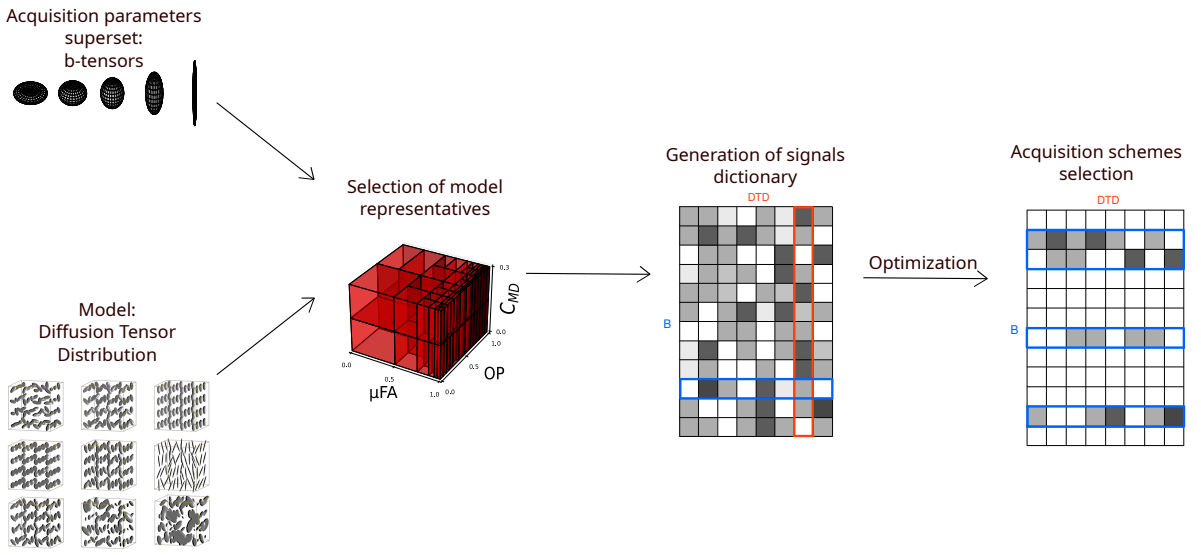

Figure 5.1 – Overview of the different steps of the method, starting from the definition of the superset of acquisitions and the collection of DTD to the selection of the optimized acquisition set.

to a DTD, more precisely, each column is the signal vector generated by the superset $\mathcal{S}$ for that DTD. Each DTD can be parameterized by three parameters: μFA, OP and C_{MD}. The range of values is [0, 1] for μFA and OP, and [0, 0.3] for C_{MD}. We restricted ourselves to DTD solely containing axisymmetric micro-tensors. We sampled 10000 micro-tensors for each DTD; the shape, size and orientation of each micro-tensor are sampled independently. The corresponding signal is simply computed according to the following equation:

$$s(\mathbf{B}) = s_0 \int p(\mathbf{D}) \exp(-\mathbf{B} : \mathbf{D}) d\mathbf{D} = s_0 \langle \exp(- < \mathbf{B} : \mathbf{D} >) \rangle \tag{5.1}$$

where s_0 is the non-diffusion weighted signal, $p(\mathbf{D})$ is the diffusion tensor distribution, $\mathbf{B} : \mathbf{D}$ is the inner product of $\mathbf{B}$ with $\mathbf{D}$, $\mathbf{D}$ is the diffusion tensor and $\langle . \rangle$ represents the averaging over the distribution.

Instead of dividing the parameter space on a regular grid, such as commonly done in fingerprinting (Rensonnet et al. 2019; Daducci, Erick J. Canales-Rodríguez, et al. 2015), we locally adapted the granularity of the subdivision to the resolution permitted by the superset $\mathcal{S}$. More precisely, in a construction inspired by octrees, we started from the initial cube representing the whole space of parameters. At each step, and for each parameter, we tried to divide the cube into two half-cubes; the division was kept only if it could discriminate the pair of newly created DTDs using our superset of acquisitions, $\mathcal{S}$.

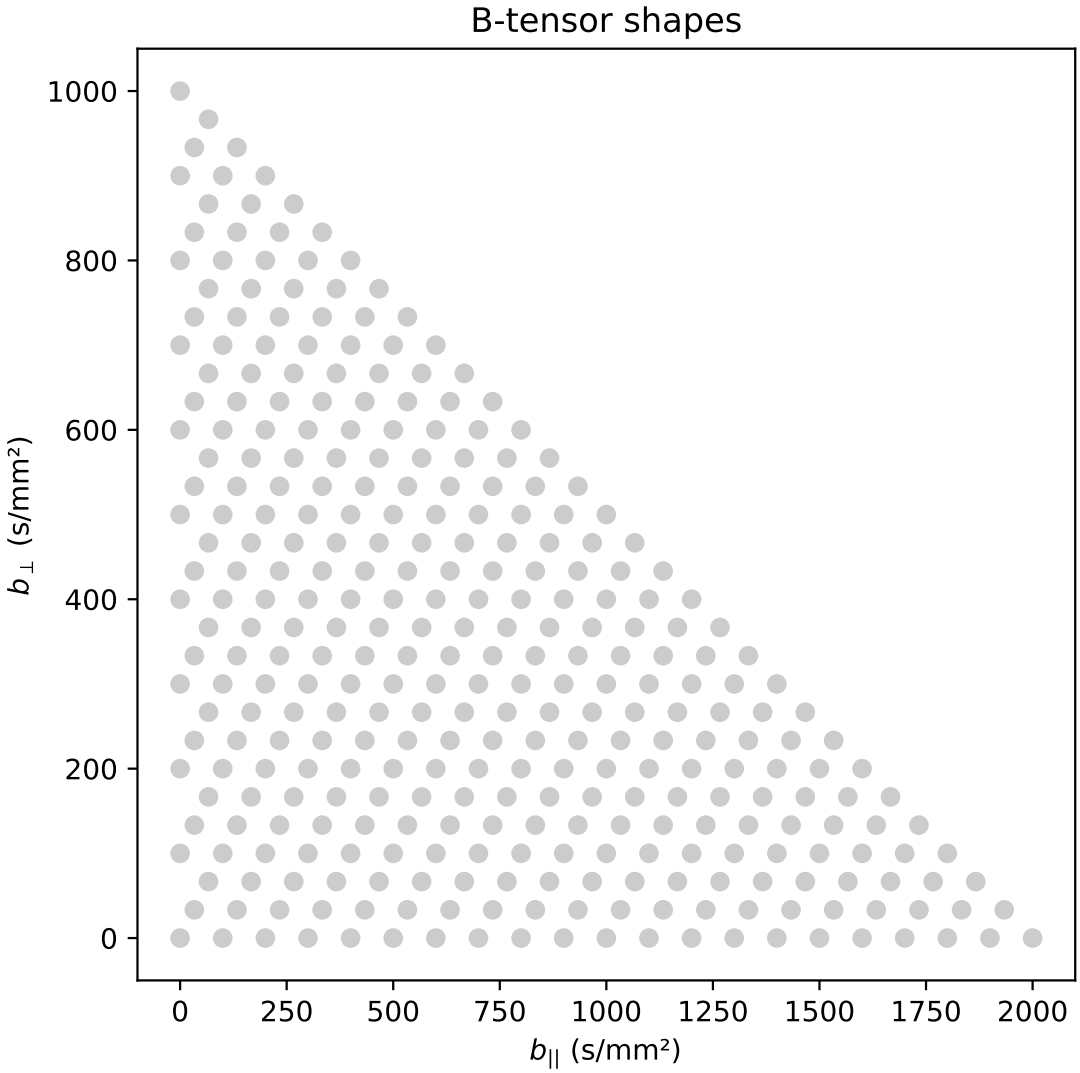

Figure 5.2 – B-tensors selected in the superset of acquisitions characterized by their two eigenvalues $b_\perp$ and $b_{||}$.

For a given acquisition scheme, $\mathcal{T} \subseteq \mathcal{S}$, we consider that two DTDs can be discriminated if

$$\max_{\mathbf{B}\in\mathcal{T}}(|s_{DTD1}(\mathbf{B}) - s_{DTD2}(\mathbf{B})|) \geq \frac{1}{SNR} \tag{5.2}$$

where $\mathbf{B}$ is a b-tensor in the acquisition scheme, $s_{DTD1}(\mathbf{B})$ (resp. $s_{DTD2}(\mathbf{B})$) is the signal predicted by DTD 1 (resp. DTD 2) for the b-tensor $\mathbf{B}$.

5.1.3 Selection of acquisition schemes

Among the superset $\mathcal{S}$, the objective is to select a small subset of k b-tensor shapes, such that the number of pairs of DTD that can be distinguished is maximized. The number of possible subsets, C_n^k, grows very quickly with n and k which renders the brute-force approach impractical.

The criterion in equation 5.2 ensures that if we take a subset $\mathcal{T} \subset \mathcal{S}$, the number of pairs of DTD that can be discriminated with $\mathcal{T}$ is at most the same as what $\mathcal{S}$ can discriminate. We can build a solution incrementally: given a subset $\mathcal{T}$, we can seek to complement it with the B-tensor shape maximizing the number of pairs of DTD that can be discriminated using $\mathcal{T}$ with this b-tensor shape on every direction considered. From this, we focused on two approaches to select the acquisition subsets: a greedy algorithm (see Algorithm 1) and a permutation algorithm (see Algorithm 2).

Input: Distance matrix, nb_shape
Output: Acquisition subset
subset ← [];
scores ← Array of size nb_shape, containing the number of pair of DTDs that can be discriminated by each shape;
for $i \leftarrow 1$ **to** *nb_shape* **do**
    best_shape ← Best shape available outside of subset;
    subset ← subset+best_shape;
    scores ← Number of new pairs that can be discriminated using each shape;
end
return subset

Algorithm 1: Greedy algorithm

We chose the number of selected b-tensor shapes so as to be comparable to the reference scheme, Q3. The scheme Q3, described in Table5.1, is optimized using the Cramér-Rao lower bound trace of the mean diffusivity, μFA, the isotropic kurtosis and the anisotropic kurtosis described in Morez et al. (2023). Since Q3 uses 120 acquisitions, we selected 4 shapes of b-tensor acquired on 30 directions each. The 30 directions were generated analytically following Koay's method (Koay 2011). The upper b-value in Q3 is 2000 $\mathrm{s\,mm^{-2}}$, which is the same as what we retained for our superset.

5.1.4 Parameter estimation

We evaluated the accuracy of the parameters of interest, using signal simulated following each of the optimized acquisition design. In order to do that, we estimated each

```
Input: Distance matrix, nb_shape, nb_rep
Output: Best acquisition subset generated
best_subset_seen ← [];
best_nb_dtds ← 0;
for i ← 1 to nb_rep do
    subset ← random selection of nb_shape shapes;
    changed ← True;
    while changed do
        weakest_shape ← Weakest shape of subset;
        nb_weakest ← number of pairs for the subset with the weakest shape;
        next_best_shape ← Best shape available outsite of the subset;
        nb_next_best ← number of pairs for the subset with the
         next_best_shape instead;
        if nb_weakest < nb_next_best then
            Switching the weakest shape with the next best one in subset;
        end
        else
            changed ← False
        end
    end
    nb_dtds_subset ← number of pairs of DTDs that can be discriminated;
    if nb_dtds_subset > best_nb_dtds then
        best_nb_dtds gets nb_dtds_subset;
        best_subset_seen ← subset;
    end
end
return best_subset_seen
```

Algorithm 2: Permutation algorithm

parameter using QTI+ constraints (Herberthson et al. 2021) and its implementation in Dipy (Garyfallidis et al. 2014).

The acquisition scheme that we use as the reference is Q3 (Morez et al. 2023). We focused more specifically on the estimation of OP and the estimation of µFA. For a given OP (resp. µFA), we generated 11 DTDs with 10000 tensors and a C_{MD} at 0.1. The 11 DTDs were generated using the full range of the varying parameter: 0 to 1 with a step of 0.1 between values.

Then, for each of these DTDs, we generated the signals from each acquisition scheme that we did or did not corrupt with Rician noise. In the case of a corruption with noise, we fixed the SNR at 30 and generated 100 signals corrupted with noise for each DTD.

5.2 Results

The hierarchical division of the parameter space yields a total of 124 cubes when we set $SNR = 25$, out of a total of $2^{3\times6} = 262144$ possible cubes, since we used 6 recursive levels. On the resulting subdivision, on Figure 5.3, we can see that the C_{MD} value has little impact on signals as only one division was made within the range. Also, we clearly have very few subdivisions in the parameter space when the µFA is small. This can be explained as it is hardly possible to find direction information within sphere-like tensors.

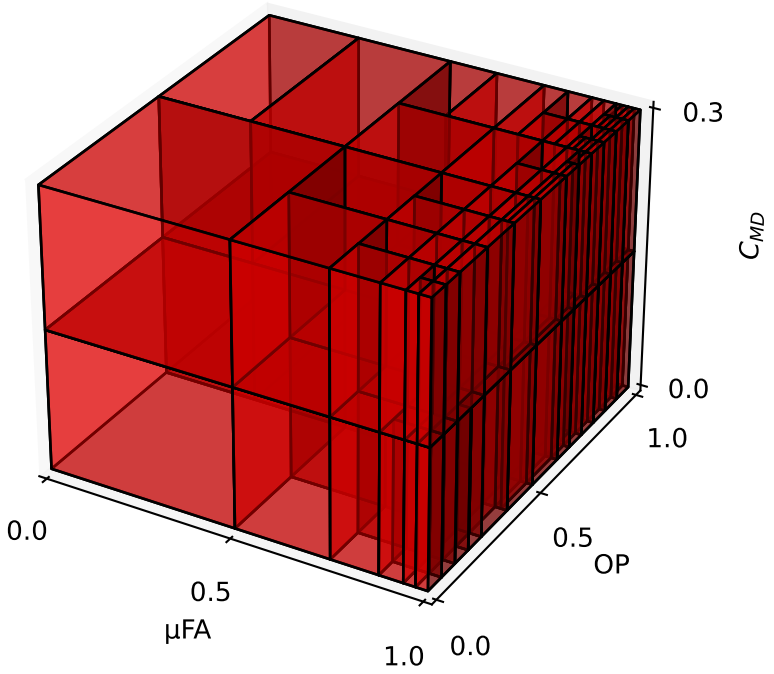

Figure 5.3 – Division of the parameter space in boxes of DTD with generated signal according to the achievable resolution.

Table 5.1 details the repartition of the b-tensor encoded acquisitions for the three acquisition schemes we compared. The first one is Q3 (Morez et al. 2023) and includes planar, spherical and linear b-tensors. The second one is the scheme optimized with the greedy algorithm. The b-values selected are between 1000 and 2000 $\mathrm{s\,mm^{-2}}$ and includes

Acquisition scheme	Q3				Greedy algorithm				Permutation algorithm			
b (s mm^{-2})	PTE	OTE	STE	LTE	PTE	OTE	STE	LTE	PTE	OTE	STE	LTE
100	7	-	-	9	-	-	-	-	-	-	-	-
800	9	-	-	50	-	-	-	-	-	-	-	-
1000	-	-	-	-	30	-	-	-	-	-	-	-
1100	-	-	-	-	-	-	-	-	-	30	-	-
1200	-	-	-	-	-	30	-	-	30	-	-	30
1300	-	-	-	-	-	-	-	30	-	-	-	30
2000	-	-	30	15	-	-	-	30	-	-	-	-

Table 5.1 – Repartition of the b-tensor encoded acquisitions. Q3 is the reference scheme, PTE corresponds to planar b-tensors, OTE to oblate b-tensors, STE to spherical b-tensors and LTE to linear b-tensors.

planar, oblate and linear b-tensors but no spherical. The last one is the scheme optimized with the permutation algorithm with 100 random initializations. Selected b-values are 1000, 1100 and 1200 s mm^{-2} with some planar, oblate and linear b-tensor selected.

Figure 5.4 shows the error on the estimation of OP over its full range for two values of µFA, without noise or with Rician noise with an SNR of 30. On the top left, we compare the estimation error for our three schemes at SNR 30 with a µFA of 0.6. In this case, similar results were achieved for the reference scheme Q3 and the scheme selected through the greedy algorithm. The permutation algorithm gives a more important error. It is interesting to note that the error is fairly high for every scheme considered here. When we look at the top right figure, we keep the same value of the noise but we increase the µFA. While the scheme from the permutation algorithm performs poorly, the scheme generated with the greedy algorithm gives an error that is decreased and better than the reference scheme. This pattern is also present in the bottom row where the signal was not corrupted with noise.

Figure 5.5 shows the error on the estimation of µFA over its full range for two values of OP, with a Rician noise at an SNR of 30 or without noise. The top row presents the estimation with Rician noise and the bottom row the estimation without noise. The first column gives the estimation for an OP of 0.4 while the second gives it for an OP of 0.8. Overall, the estimation error is smaller than it is for the estimation of OP. In all four cases, Q3 and the greedy algorithm scheme perform similarly. In presence of noise, the permutation algorithm generated the most errors. However, without noise, it generates the best results.

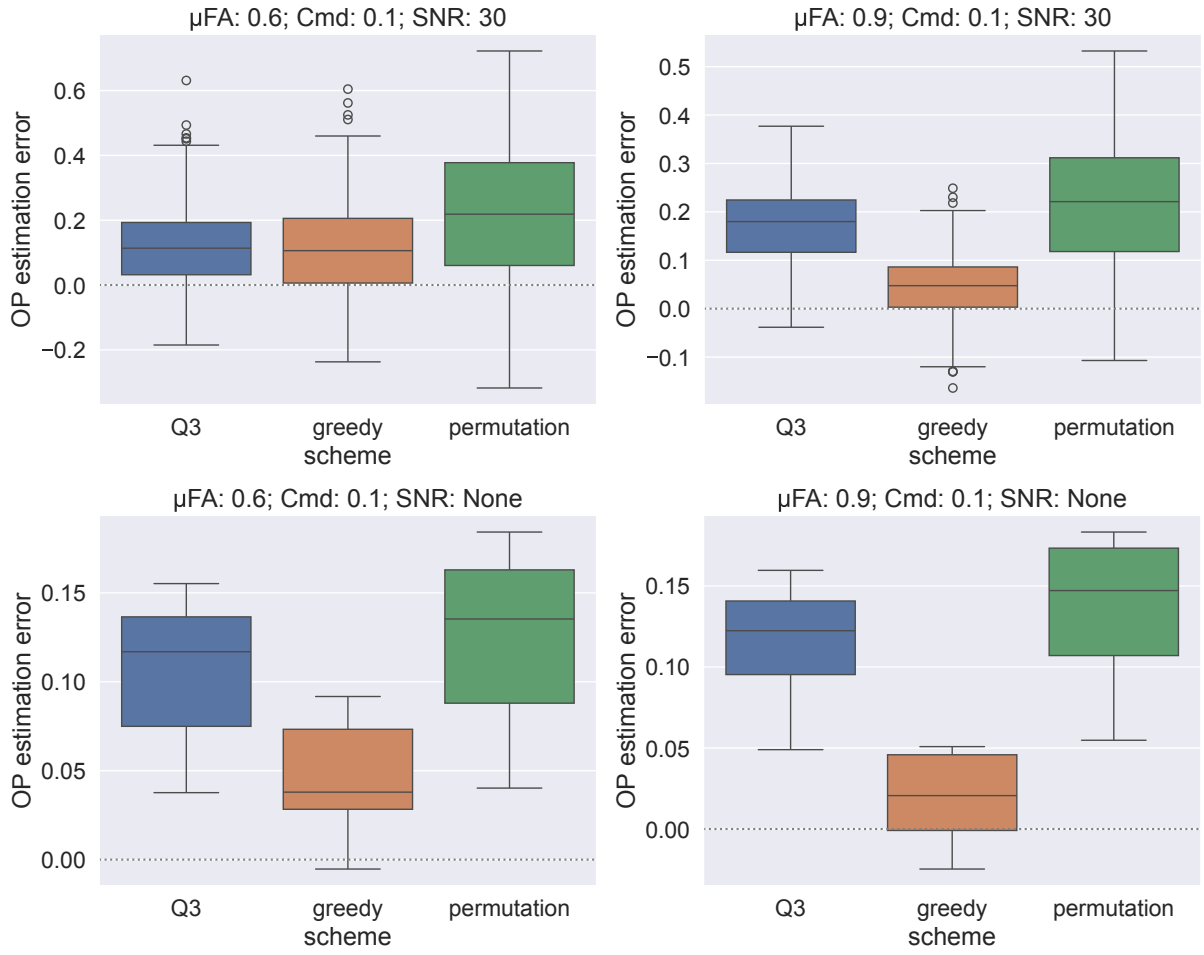

Figure 5.4 – OP estimation error on its full range. In blue, the reference scheme; in orange, the greedy algorithm result; in green, the permutation algorithm result. (top row) The signal was corrupted with a Rician noise at an SNR 30. (bottom row) The signal was not corrupted with any noise. (first column) μFA was set at a medium value. (second colomn) μFA was set at a high value.

5.3 Extensions

The proposed framework aims to improve the accuracy of DTD parameters estimation. Although this approach, which we described in Bocquillon, Corouge, and Caruyer (2025c), is promising, a number of potential improvements can be explored at several steps. First, in all our experiments, the number of directions were fixed for each b-tensor shape, irrespective of the angular resolution of the corresponding signal. We can change the superset of acquisitions to include more or fewer directions depending on the b-value and the shape of the b-tensor. That can be achieved by computing the band limit in

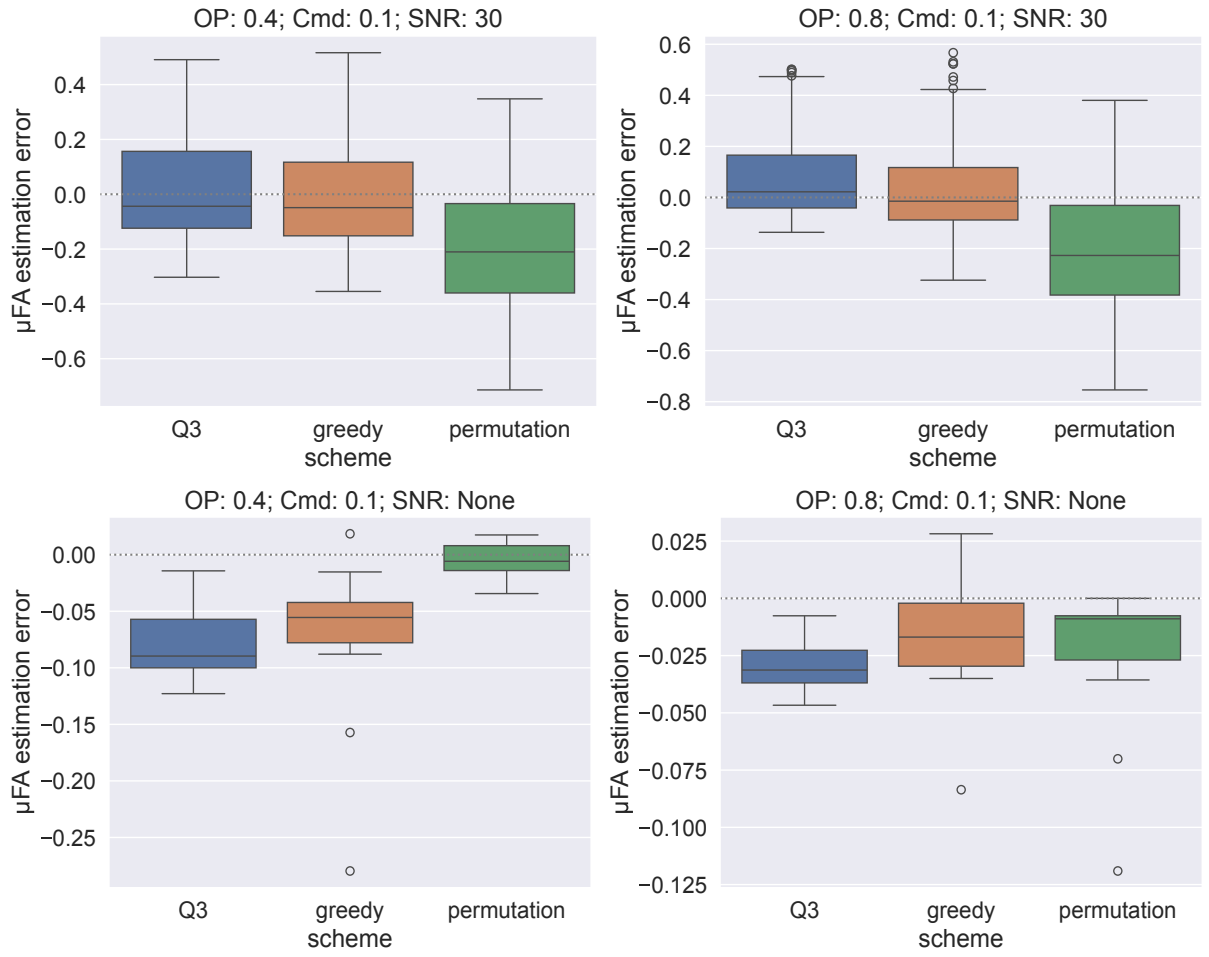

Figure 5.5 – µFA estimation error on its full range. In blue, the reference scheme; in orange, the greedy algorithm result; in green, the permutation algorithm result. (top row) The signal was corrupted with a Rician noise at an SNR 30. (bottom row) The signal was not corrupted with any noise. (first column) OP was set at a medium value. (second colomn) OP was set at a high value.

spherical harmonics for each b-tensor shape (Bates, Daducci, Sadeghi, et al. 2020). Then, we can select a number of directions based on the band-limit using e.g. spherical codes (N. J. A. Sloane et al. n.d.[b]). Another direction of improvement is to change the metric used to determine whether two DTDs can be discriminated. In this section, we explore these two improvement directions.

5.3.1 Adapting the number of directions in the superset

In diffusion MRI, the minimum number of gradient directions needed for each b-tensor (shape and b-value) is related to the orientation dependence of the diffusion signal. Each b-tensor may require different angular sampling to fully capture the orientation information, depending on its shape and b-value. For example, spherical tensors are rotationally invariant and technically require only one direction to estimate the signal, whereas a linear b-tensor is highly dependent on the direction and requires more directions to fully sample the signal.

Method

The diffusion signal for an axisymmetric b-tensor can be represented using spherical harmonics and is considered to be band-limited in that basis, as the coefficients beyond a threshold become negligible (Bates, Daducci, and Caruyer 2019; Bates, Daducci, Sadeghi, et al. 2020). The band-limit is given by a maximum harmonic order L needed to accurately approximate the signal for each b-tensor. Here, we decided to compute that band-limit L, which can be translated into a minimum number of acquisition directions for each b-tensor shape.

In order to compute the band-limit, we use a diffusion tensor distribution model with fixed parameters (OP, μFA and C_{MD}) to generate the signals. To prevent orientation bias in the evaluation of the acquisition scheme, that DTD was rotated across a number of directions distributed on the sphere using electrostatic repulsion (D. Jones, Horsfield, and A. Simmons 1999).

Then, we generated the signal for these DTD with a high number of directions for the b-tensors and used those signals as the comparison point. To determine the band-limit, we generated the signal with several sets of directions, corresponding to different band-limits L. Those directions were computed using Koay's method (Koay 2011). Finding the band-limit is to find the minimal number of directions ensuring that the absolute reconstruction error is below a selected threshold t:

$$\max\{|(\frac{S}{S_0})_R - (\frac{S}{S_0})_{GT}|\} < t \tag{5.3}$$

where $|.|$ is the absolute value, $(\frac{S}{S_0})_R$ is the reconstructed signal, $(\frac{S}{S_0})_{GT}$ is the signal generated with the high number of directions and $t = 0.01$ is the threshold we chose.

Once the number of directions is selected for each b-tensor shape, the generation of the

dictionary and the parameter estimation can be done following the method from section 5.1. As for the selection of the acquisition scheme, we used a modified version of the greedy algorithm. The goal is to keep up to a given number of measurements and no longer to a fixed number of b-tensors. The modified version of this algorithm is given in Algorithm 3. As we no longer rely on a fixed number of directions, the score for each b-tensor changes to the number of pairs that can be discriminated by that b-tensor divided by the number of directions that is required by it.

```
Input: Distance matrix, nb_measurements
Output: Acquisition subset
subset ← [];
scores ← Array of size nb_shape, containing the number of pair of DTDs that
 can be discriminated by each shape divided by the number of direction needed
 by that shape;
boolean ← True;
nb_acquisition_left ← nb_measurments;
while boolean do
    best_shape ← Best shape available outside of subset;
    nb_acquisition_needed ← Number of directions needed by best_shape;
    if nb_acquisition_needed < nb_acquisition_left then
        nb_acquisition_left ← nb_acquisition_left - nb_acquisition_needed
         subset ← subset+best_shape;
        scores ← Number of new pairs that can be discriminated using each shape
         divided by the number of direction needed;
    end
    else
        boolean ← False
    end
end
return subset
```

Algorithm 3: Weighted greedy algorithm

Results

Following this method, the band-limit was computed for a collection of b-tensors with a $b_{||}$ and a $b_{\perp}$ up to 2000 $\mathrm{s\,mm^{-2}}$ and is shown in Figure 5.6. The DTD model that was used had 10,000 tensors, and we fixed the microscopic anisotropy at 0.85, the orientation parameter at 0.85, the size variance at 0.1 and the mean diffusivity at 2.0×10^{-3} $\mathrm{mm^2\,s^{-1}}$. This DTD was rotated across 20 directions.

The ground truth signal was generated using 300 directions on the sphere. In Figure 5.6, the dark blue and the light blue corresponds to a minimum of 6 ($L = 2$) directions needed, the green corresponds to 24 ($L = 4$) directions and the yellow is where a minimum of 47 ($L = 6$) directions are needed.

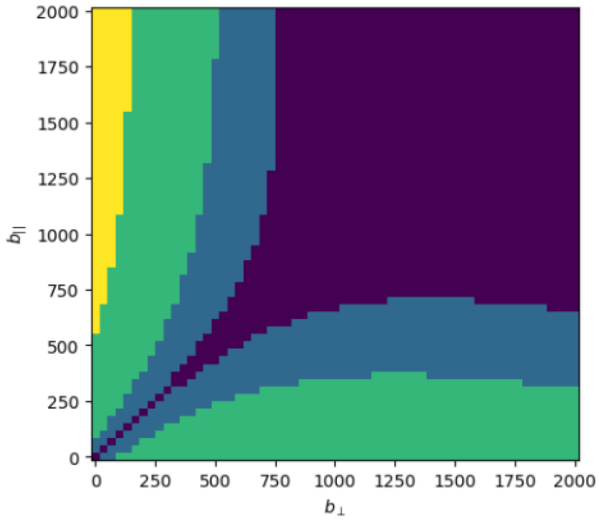

Figure 5.6 – Number of directions computed for the b-tensors of interest. Dark blue and light blue corresponds to b-tensors requiring at least 6 directions. Green corresponds to b-tensors requiring at least 24 directions. Yellow corresponds to b-tensors requiring at least 47 directions.

Using Algorithm 3, the acquisition scheme was selected and its details are in Table 5.2. It includes 113 measurements spread between two linear b-tensors, 2 prolate b-tensors, one spherical b-tensors and 4 oblate b-tensors. The b-values ranges from 300 $\mathrm{s\,mm^{-2}}$ to 1900 $\mathrm{s\,mm^{-2}}$.

The parameters were estimated and the estimation error from the newly selected acquisition schemes was compared to the reference scheme Q3 as well as the two previously computed schemes using the greedy algorithm and the permutation approach. Figure 5.7 shows the error on the estimation of OP over its full range for two values of μFA, with Rician noise with an SNR of 30 or without noise. On the top left, we have the comparison of the estimation error for our four scheme with Rician noise with an SNR of 30 and a μFA of 0.6. On this figure, we have similar result for the comparison scheme Q3 and the two greedy generated schemes. The bottom left corresponds to the same μFA without noise. In this case, the newly generated scheme has similar result to the comparison scheme but does not perform as well as the first greedy scheme. On the right, the μFA value is set

Acquisition scheme	Weighted greedy algorithm			
b ($\mathrm{s\,mm^{-2}}$)	OTE	STE	PrTe	LTE
300	6	-	-	-
500	-	-	-	24
900	-	-	6	-
1000	6	-	-	-
1100	-	6	6	-
1200	6	-	-	-
1500	6	-	-	-
1900	-	-	-	47

Table 5.2 – Repartition of the b-tensor encoded acquisitions selected using the greedy algorithm modified for b-tensors with a number of directions suited for each b-tensor. OTE to oblate b-tensors, STE to spherical b-tensors, PrTE corresponds to prolate b-tensors and LTE to linear b-tensors. This acquisition scheme is composed of 113 measurements.

higher, at 0.9, and in both cases, the first greedy scheme performs the best, the newly generated scheme is second and does a bit better than the reference scheme. In all cases, the permutation scheme is doing the worse.

Figure 5.8 shows the error on the estimation of the μFA over its full range for two values of OP, with a Rician noise at an SNR of 30 or without noise. The first column corresponds to the estimation error for an OP of 0.4, the second corresponds to an OP of 0.8. The top row is the estimation error with the noise, the bottom row is the estimation error without noise. On the top row, in both case, the weighted greedy results is similar if not slightly better than the greedy results and the reference scheme. For the bottow row, the results are quite different as the permutation results are better than the three others. With the smaller value of OP, the results are much better than at the higher value. Overall, the three other gives similar results on both cases.

5.3.2 Exploring another metric to discriminate between DTDs

Method

A second approach to attempt improving the result is to change the metric used to discriminate between models. In section 5.1, the metric used to discriminate models is given by the L_∞ norm, given in Equation 5.2. However, the L_∞ norm reflects the strongest single difference between the two signals. However, this may not be the most suitable metric for our use. For example, the use of the L_2 reflects the overall signal

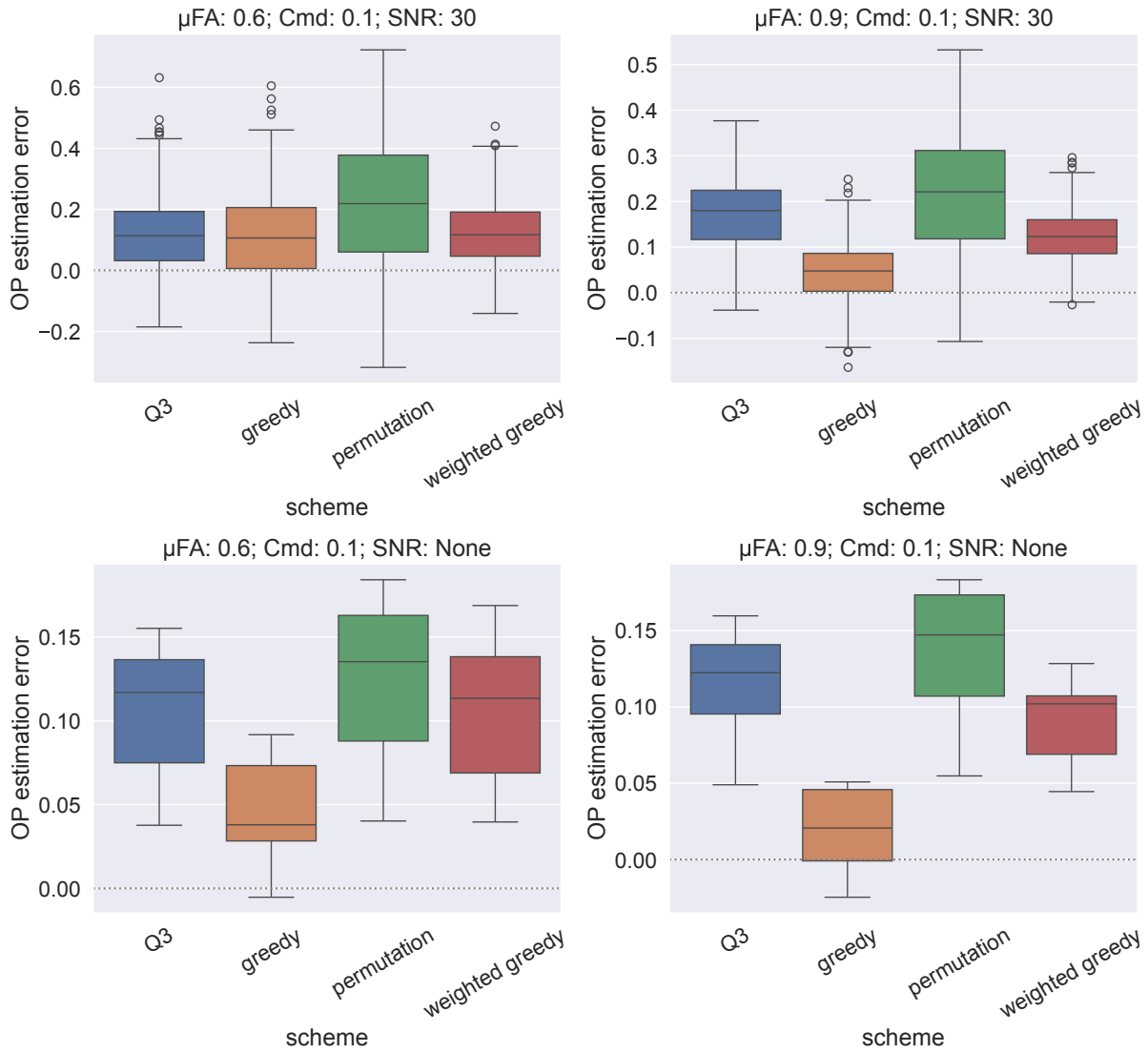

Figure 5.7 – OP estimation error on its full range. In blue, the reference scheme; in orange, the greedy algorithm result; in green, the permutation algorithm result; in red, the weighted greedy algorithm result. (top row) The signal was corrupted with a Rician noise at an SNR 30. (bottom row) The signal was not corrupted with any noise. (first column) μFA was set at a medium value. (second column) μFA was set at a high value.

difference between models and could potentially give better results.

Here, we chose to use the L_2 norm to discriminate between models. This norm is given by:

$$d = \sqrt{\sum_{\mathbf{B}\in\mathcal{T}} (s_{DTD1}(\mathbf{B}) - s_{DTD2}(\mathbf{B}))^2} \tag{5.4}$$

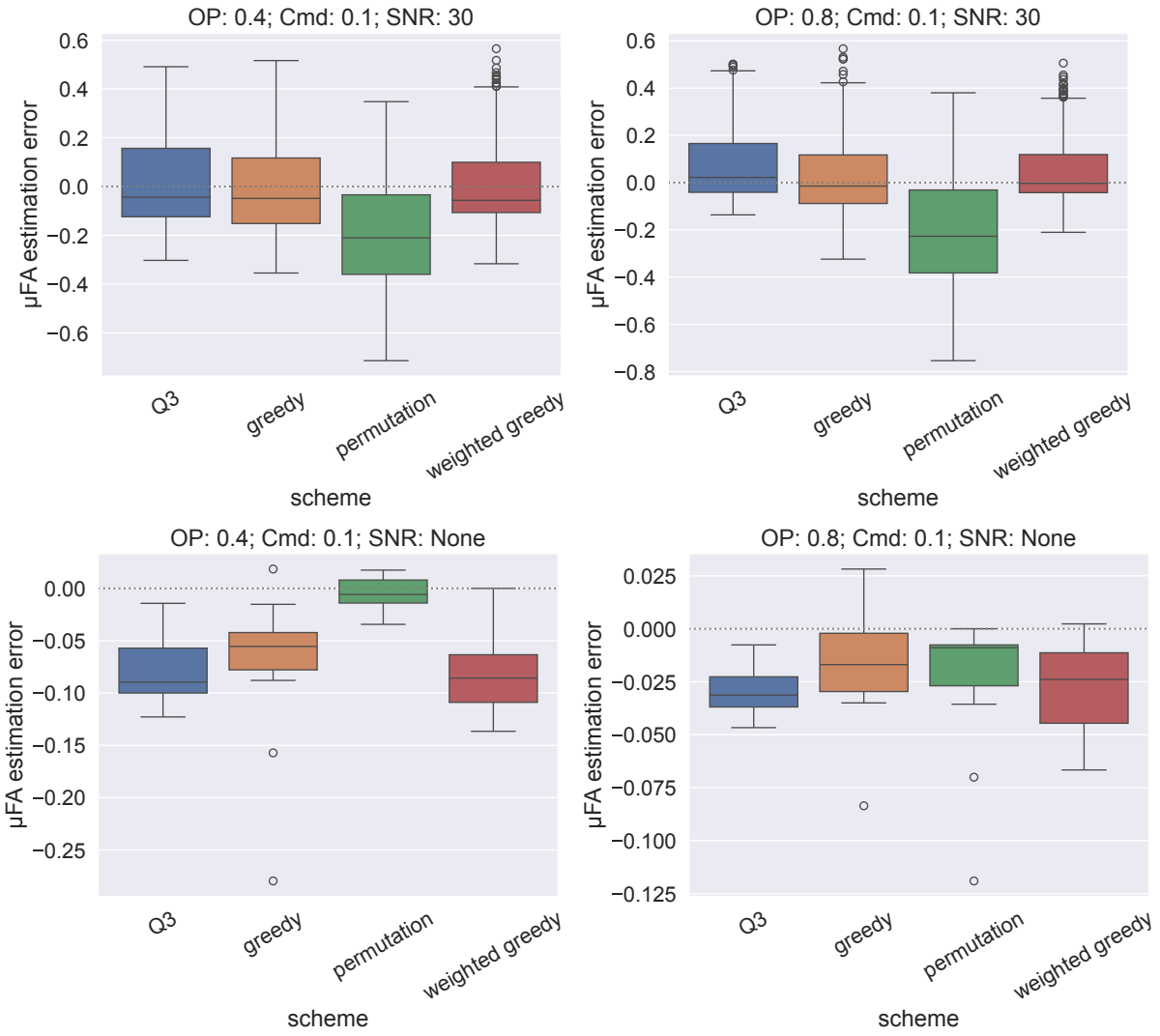

Figure 5.8 – µFA estimation error on its full range. In blue, the reference scheme; in orange, the greedy algorithm result; in green, the permutation algorithm result; in red, the weighted greedy algorithm result. (top row) The signal was corrupted with a Rician noise at an SNR 30. (bottom row) The signal was not corrupted with any noise. (first column) OP was set at a medium value. (second column) OP was set at a high value.

where d is the distance between the two models, $s_{DTD1}(\mathbf{B})$ (resp. $s_{DTD2}(\mathbf{B})$) is the signal generated from DTD 1 (resp. DTD 2) for the b-tensor $\mathbf{B}$ and $\mathcal{T}$ is the selected acquisition scheme.

To test this metric, we decided to compare the result with the reference scheme Q3 as well as the results using the L_∞ norm. We also decided to use a bruteforce algorithm to get the optimal solution, which is the solution that maximizes the number of models that

are discriminated using either of the metric.

Results

Table 5.3 shows the two acquisition schemes generated using the L_∞ norm for the greedy algorithm and the global solution. For these two, one planar b-tensor, one oblate b-tensor and two linear b-tensors were selected. The b-value were between 700 to 2000 $\mathrm{s\,mm^{-2}}$.

Acquisition scheme	LinfGr			LinfGl		
b ($\mathrm{s\,mm^{-2}}$)	PTE	OTE	LTE	PTE	OTE	LTE
700	-	-	-	-	-	30
1000	30	-	-	-	30	-
1200	-	30	-	-	-	-
1300	-	-	30	-	-	-
1400	-	-	-	30	-	-
2000	-	-	30	-	-	30

Table 5.3 – Repartition of the b-tensor encoded acquisitions with the L_∞ norm. LinfGr corresponds to the acquisition scheme generated by the greedy algorithm; LinfGl corresponds to the global solution; PTE corresponds to planar b-tensors, OTE to oblate b-tensors and LTE to linear b-tensors.

Table 5.4 shows the two acquisition schemes generated using the L_2 norm for the greedy algorithm and the global solution. For each, one spherical b-tensor and three linear b-tensors were selected. The b-values range from 1100 to 1700 $\mathrm{s\,mm^{-2}}$.

Acquisition scheme	L2Gr		L2Gl	
b ($\mathrm{s\,mm^{-2}}$)	STE	LTE	STE	LTE
1100	30	-	-	-
1200	-	30	30	-
1300	-	30	-	30
1400	-	-	-	30
1500	-	-	-	30
1700	-	30	-	-

Table 5.4 – Repartition of the b-tensor encoded acquisitions with the L_2 norm. L2Gr corresponds to the acquisition scheme generated by the greedy algorithm; L2Gl corresponds to the global solution; STE to spherical b-tensors and LTE to linear b-tensors.

Figure 5.9 shows the estimation error of OP over its full range for two values of μFA, with or without Rician noise with an SNR at 30, and with a size variance set at 0.1. The

column on the left corresponds to a μFA set at 0.6. The column on the right corresponds to a μFA set at 0.9. The top row shows the results with Rician noise with an SNR of 30. The bottom row corresponds to noiseless results. On the top left, the results for the L_∞ norm, the reference scheme and the greedy result for the L_2 norm are very similar. On the top right, the results from the greedy algorithm for both metrics perform better than the rest of the acquisition schemes. On the bottom row, the result for the greedy scheme using the L_∞ norm and both results for the L_2 norm are similar and perform better than Q3, the reference scheme. The acquisition scheme generated using the global solution with the L_∞ norm performs significantly worse than the rest.

Figure 5.10 shows the estimation error of μFA over its full range for two values of OP, a size variance set at 0.1, with or without Rician noise with an SNR set at 30. The left column corresponds to an OP at 0.4. The right column corresponds to an OP set at 0.8. The top row corresponds to the results altered by a Rician noise at an SNR of 30. The bottom row shows the results without noise corruption. On the top row, the reference scheme and the greedy result for the L_∞ norm gives the best results, closely followed by the greedy result for the L_2 norm, then the global solution for the L_2 norm. On the bottom row, the greedy results for both norm and the global solution for the L_2 norm gives very similar results, the reference scheme performs similarly too. However, the global solution for the L_∞ gives a less satisfying results.

5.4 Discussion and conclusion

The estimation of microstructure parameters is greatly influenced by the acquisition scheme. Our approach allows to generate acquisition schemes optimized towards the reconstruction of selected parameters.

We proposed a framework aiming to improve the accuracy of DTD parameters estimation. We found that the b-tensor encoded acquisition scheme generated by the greedy approach provided the best results in terms of estimation compared to the previously proposed scheme we used as a reference. While the current results can be further improved, we generated acquisition schemes with similar or better estimation errors while ensuring its feasibility on a clinical MR scanner. One unexplored potential improvement is to take into consideration the impact of the shape of a b-tensor and its b-value on the echo time (TE), directly related to the waveform (Sjölund et al. 2015). That way, we can not only select an upper bound in the number of acquisitions selected, but also guide the choice

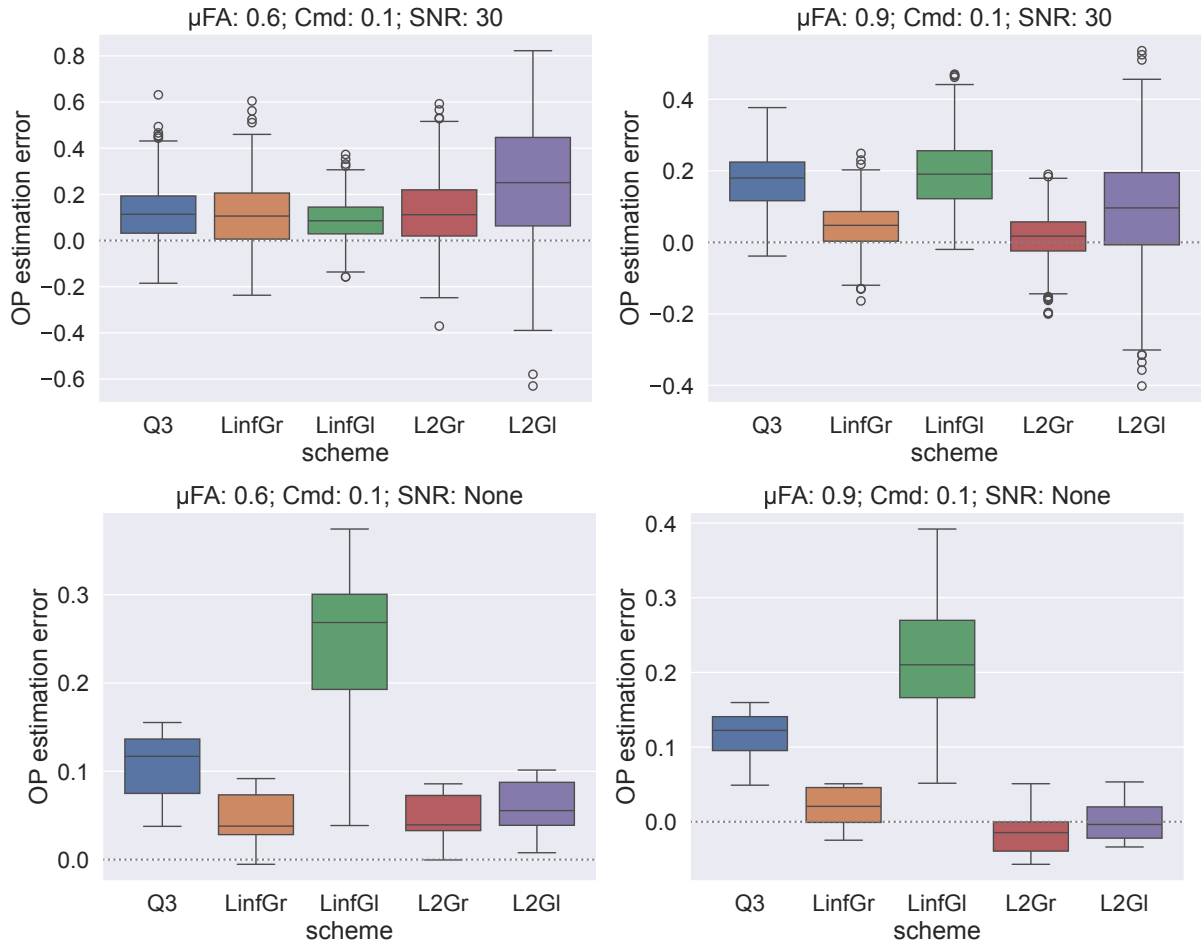

Figure 5.9 – OP estimation error on its full range. In blue, the reference scheme; in orange, the greedy algorithm result with a L_∞ norm; in green, the global solution for the L_∞ norm; in red, the greedy algorithm result with a L_2 norm; in purple, the global solution for the L_2 norm. (top row) The signal was corrupted with a Rician noise at an SNR 30. (bottom row) The signal was not corrupted with any noise. (first column) μFA was set at a medium value. (second column) μFA was set at a high value.

towards b-tensor shapes with shorter TE, leading to an overall improvement in SNR.

In this work, we focused on the DTD framework but this could easily be adapted to generate acquisition schemes tailored specifically for their reconstruction of biophysical models such as AxCaliber (Assaf, Blumenfeld-Katzir, et al. 2008), CHARMED (Assaf and P. J. Basser 2005), NODDI (Zhang et al. 2012) or SANDI (Palombo et al. 2020) as they too have a limited number of parameters of interest.

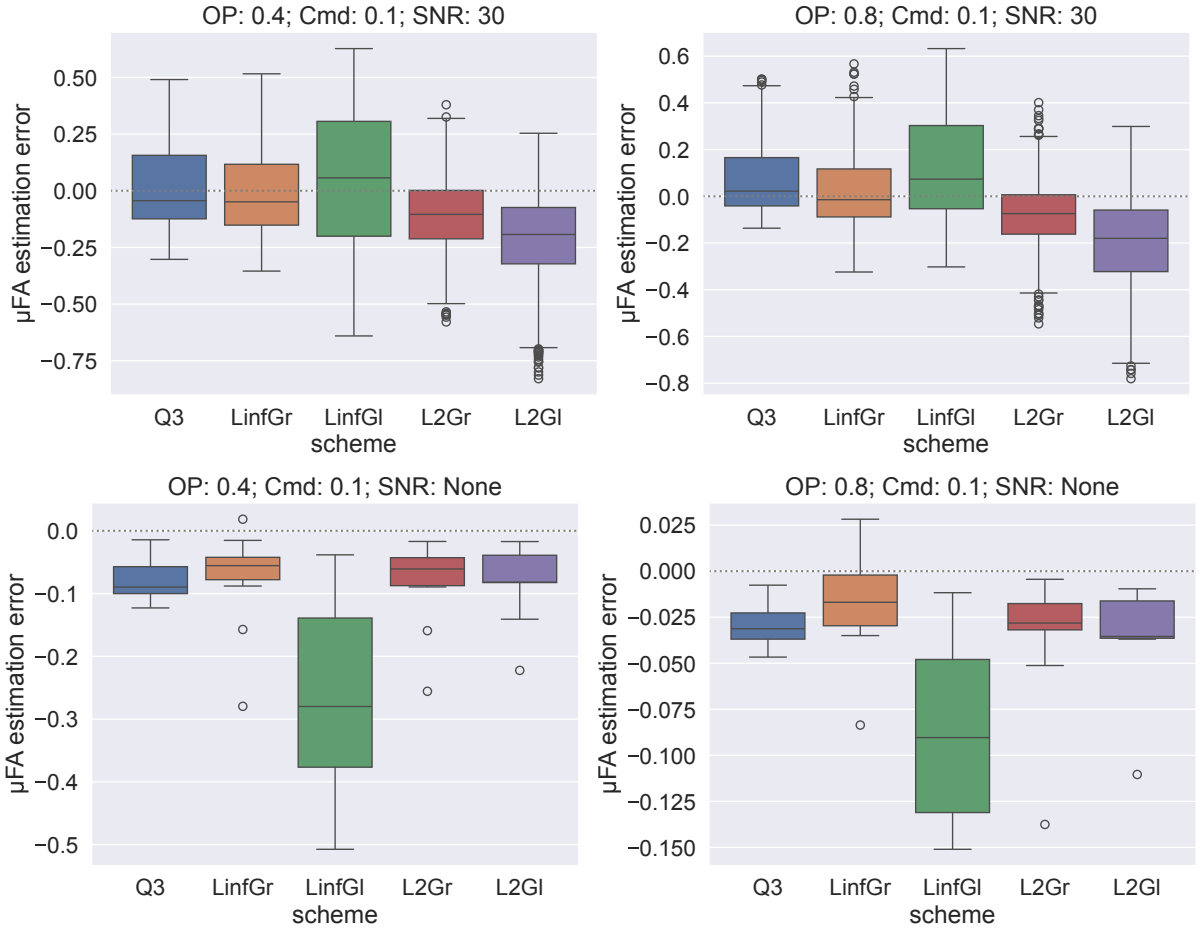

Figure 5.10 – µFA estimation error on its full range. In blue, the reference scheme; in orange, the greedy algorithm result with a L_∞ norm; in green, the global solution for the L_∞ norm; in red, the greedy algorithm result with a L_2 norm; in purple, the global solution for the L_2 norm. (top row) The signal was corrupted with a Rician noise at an SNR 30. (bottom row) The signal was not corrupted with any noise. (first column) OP was set at a medium value. (second column) OP was set at a high value.

Chapter 6

Linking Diffusion Tensor Distribution (DTD) parameters with microstructure information

Diffusion MRI provides an indirect access to tissue microstructure by probing the displacements of water molecules within complex biological substrates. In heterogeneous media, these displacements reflect a combination of microscopic environments with structural features such as fiber organization, compartment composition and local diffusivities. Accurately capturing this variability requires moving beyond single-compartment descriptions toward richer representations of the signal. Q-space trajectory imaging (QTI) (C.-F. Westin, Hans Knutsson, et al. 2016) follows this approach by modeling the signal as arising from a diffusion tensor distribution (DTD) and estimated from b-tensor encoded acquisitions.

While the DTD provides a richer representation of tissue microstructure than single-compartment models, interpreting the estimated parameters in terms of the underlying biophysical properties of the substrate remains challenging. The relationship between the estimated parameters and tissue properties is indirect, as different microstructral configurations may yield similar signals. Limitations in data acquisition and estimation further restrict what can be reliably inferred, making it essential to determine which substrate property is encoded by each model parameter.

In this work, we propose to investigate the link between the angular dispersion of fibers in a white matter substrate and the orientation parameter (OP) estimated from the diffusion tensor distribution. To do so, we generated a collection of realistic white matter numerical substrates using CACTUS (Villarreal-Haro et al. 2023) and computed the diffusion-weighted signal associated to each substrate using Monte-Carlo simulations (Rafael-Patino et al. 2020). By controlling the substrate generation, we know the ground-truth value of the fiber orientation while having the possibility to get the orientation

parameter with the diffusion-weighted signal or estimating it from the numerical substrate.

The work presented in this chapter has been developed in collaboration with researchers from the LTS5 at EPFL, in particular Dr. Juan Luis Villarreal Haro, in the context of the MMINCARAV then DECRYPT associated team. Part of the results in this chapter were presented in the form of an abstract (Bocquillon, Villarreal Haro, et al. 2024).

6.1 Methods

6.1.1 Substrate generation

We generated a collection of 11 numerical white matter substrates, each corresponding to a single fiber population with a specific angular dispersion, using CACTUS (Villarreal-Haro et al. 2023).

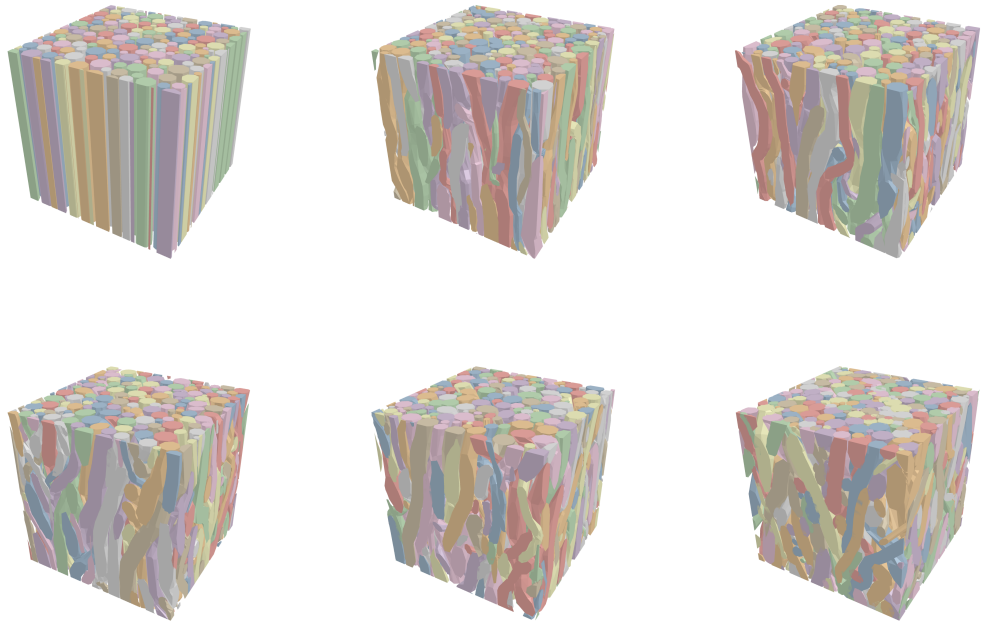

Figure 6.1 – Cropped numerical substrates generated using CACTUS (Villarreal-Haro et al. 2023). The intracellular volume fraction is set to 0.72; fibers have a gamma-distributed radius with a shape parameter $\kappa = 1$ and a mean radius of 2.5 μm. The angular dispersion is the only varying parameter. (top row) From left to right: 0°, 5° and 10°. (bottom row) From left to right: 15°, 20° and 25°.

First, the substrate is initialized using a user-defined angular dispersion, ranging from 0° to 25° with a step of 2.5°, as the increase in angular dispersion hinders the generation of the substrate and increases the computation time quickly. The endpoints of the fibers are generated by CACTUS in accordance to this angular dispersion. For all substrates, we selected fiber radii following a gamma distribution with a mean radius of 2.5 μm and a shape parameter κ of 1. The fiber endpoints are generated to satisfy these conditions until we reach a target density; in our case, we ensure a packing density of 0.72. At this stage, many collisions and overlaps may remain in the fiber trajectories. In order to obtain non-overlapping fiber structures, CACTUS performs a joint fiber optimization. This step also limits extreme curvature in the fiber trajectories by applying a regularization constraint. For this experiment, we decided against using the third optimization step (called radial growth) in CACTUS; it would have heavily increased computation time for the generation of the substrates.

Examples of the generated substrates can be seen on Figure 6.1.1. Each substrate is in a cube of side length of 200 μm.

6.1.2 Estimation of a ground truth orientation parameter from the substrate

From the substrates, we propose a method to compute a geometric orientation parameter, OP_{gt}, which will serve as a reference or "ground truth" for the orientation parameter estimated from the diffusion signal. We approximate the centerline trajectory of each fiber with a set of segments of equal length, λ. In continuation, we assimilate each segment to a unit vector, $\mathbf{u}_i$, keeping only the orientation of the segments. Last, we consider the set of rank-1 tensors $\mathbf{T}_i = \mathbf{u}_i \otimes \mathbf{u}_i = \mathbf{u}_i \mathbf{u}_i^{\mathrm{T}}$. From this collection of rank-1 tensors, we compute OP_{gt} following Eq. 2.29:

$$OP_{\text{gt}}(\lambda) = \sqrt{\frac{< \langle \mathbf{T}_i \rangle^{\otimes 2}, \mathbb{E}_{shear} >}{< \langle \mathbf{T}_i^{\otimes 2} \rangle, \mathbb{E}_{shear} >}} \tag{6.1}$$

Note that this OP_{gt} depends on the segment length, λ, as depicted on Figure 6.1.2. Intuitively, we shall select λ close to the characteristic diffusion length so that OP_{gt} is comparable to the OP estimated from the diffusion signal.

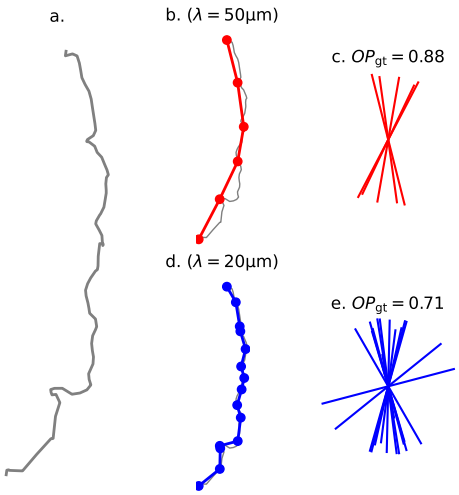

Figure 6.2 – Illustration of how the ground truth orientation parameter, OP_{gt}, is computed from the substrate. Each fiber trajectory (panel a) is cut into segments of equal length, λ (panels b and d). The population of segment directions (panels c and e) is then converted into a distribution of rank-1 tensors, from which we compute OP_{gt}. For clarity, a single fiber trajectory is depicted here, but the process is performed in general for the whole substrate.

6.1.3 Monte-Carlo simulations

Acquisition scheme

From the substrate, we can simulate the diffusion signal via Monte-Carlo simulations. We used the acquisition scheme proposed in Morez et al. (2023), corresponding to the Q3 scheme from the paper, summarized in Table 6.1. This acquisition scheme is composed of three distincts b-values ranging from 100 to 2000 s mm^{-2} and includes planar, spherical and linear b-tensors, for a total of 120 measurements.

b (s mm^{-2})	PTE	STE	LTE
100	7	-	9
800	9	-	50
2000	-	30	15

Table 6.1 – Repartition of the b-tensor encoded acquisitions in the acquisition scheme; the selected acquisition scheme is the Q3 scheme from Morez et al. (2023). PTE corresponds to planar b-tensors, STE to spherical b-tensors and LTE to linear b-tensors.

We implemented all b-tensors using the same spherical q-space trajectory template encoding a spherical b-tensor (see Figure 6.3), which was optimized using NOW (Szczepankiewicz and Sjölund 2021). We then applied a linear transform (scale and rotation) to this trajectory to generate the gradient waveform corresponding to each b-tensor. This ensures that the timing and spectral components of waveforms are similar across acquisitions.

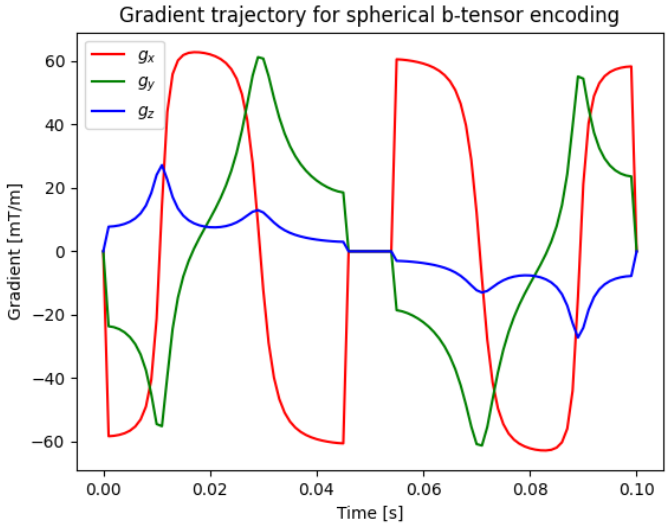

Figure 6.3 – Gradient trajectory for the spherical b-tensor used to generate the gradient trajectories for the acquisition scheme.

Signal generation

The Monte-Carlo simulation was done using the Monte Carlo Diffusion and Collision simulator (MCDC) presented in Rafael-Patino et al. (2020). For each substrate, we have generated 1,000,000 particles or spins. Those particles were initialized randomly in space, inside (respectively outside) the axons for the intra-axonal signal (respectively extra-axonal signal). Simulations for intra- and extra-axonal signal were performed separately. As the substrate is of side length of 200μm, the particles are initialized inside a cube of side length of 100μm centered around the middle of the substrate in order to ensure that particles do not diffuse outside of the substrate boundaries. The diffusion was simulated for a duration of 101ms over 1,000 time steps. The trajectories are stored in order to allow the testing of different acquisition schemes more easily, specifically to avoid the computation time for the diffusion process in MCDC that can take from hours to several days. From the trajectories, MCDC estimates the diffusion signal according to Eq. 2.56.

Estimation of the orientation parameter from the signal

Using the signal generated by the MCDC and the selected acquisition scheme, we calculate the DTD parameters and estimate the orientation parameter OP (see Equations 2.30 and 2.32). This calculation is based on the implementation of the QTI/QTI+ (Herberthson et al. 2021; C.-F. Westin, Hans Knutsson, et al. 2016) framework in the open-source library "Diffusion Imaging In Python" (DIPY) (Garyfallidis et al. 2014). For each substrate, the estimated OP is then compared with the geometric OP, OP_{gt}, considered as our reference, as described in subsection 6.1.2. The comparison is performed for four different segment lengths $\lambda \in [5\mu m, 50\mu m]$.

6.2 Results and discussion

First, we examine the relationship between the geometric orientation parameter OP_{gt} and the angular dispersion of the substrates in order to verify the quality of our ground truth. Then, we estimate the OP generated by the intra-axonal signal and compare it to the geometric orientation parameter OP_{gt} in order to estimate the bias of the estimation. Finally, we examine the relationship between the OP generated from the extra-axonal signal and compare it to the geometric orientation parameter OP_{gt}.

Assessment of geometric OP

Figure 6.4 illustrates the relation between the angular dispersion in degrees from the substrate and the geometric orientation parameter OP_{gt}. This figure shows a seemingly almost linear relation between the angular dispersion from 0 to 25° and OP_{gt} ranging from 1 to 0.5.

When estimating OP from the substrates, we need to select a segment length that is suitable for the acquisition scheme that we use. The right segment length needs to be in the same order as the typical distance water molecule diffuse over the diffusion time. This distance is called the characteristic diffusion length. It is defined in 1D as:

$$l = \sqrt{2D\tau} \tag{6.2}$$

where D is the diffusion coefficient and τ is the effective diffusion time. In the case of b-tensor encoded acquisitions, the notion of a single diffusion time, hence a single characteristic length, is no longer well-defined. Instead, it is a diffusion time spectrum,

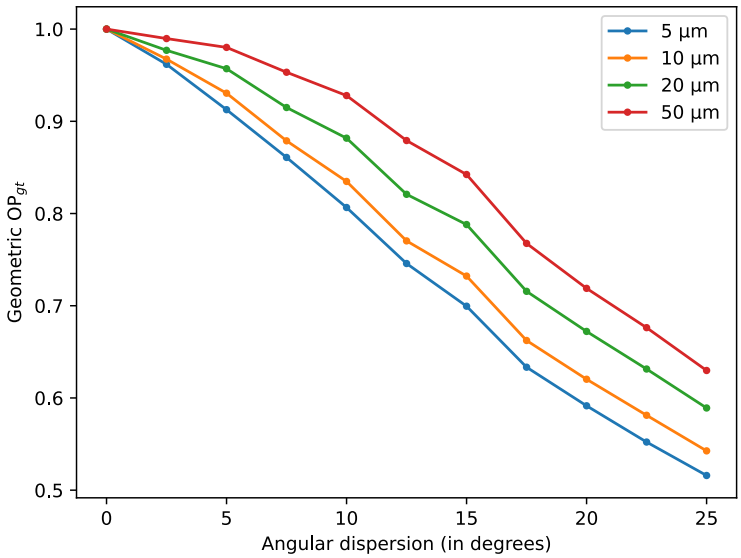

Figure 6.4 – Geometric OP_{gt}, corresponding to the estimation of the OP from the substrate, as a function of the angular dispersion in degrees from the substrate. The geometric OP is generated for four segment lengths $\lambda \in [5\mu m, 50\mu m]$.

thus a characteristic length spectrum. In our case, we estimated the effective diffusion time τ around 60 - 80 ms. This corresponds to a characteristic diffusion length of 15 - 18 µm. Hence, we generated four segment lengths, λ, ranging from 5 to 50µm in our experiments.

OP estimation for the intra-axonal compartment

In Figure 6.5 is illustrated the relation between the estimated value of the orientation parameter using the intra-axonal signal from MCDC and the ground-truth orientation parameter from the substrate. For small angular dispersions, the orientation parameter is close to 1 and does not show as much difference between the different segment lengths as larger angular dispersions.

OP estimation for the extra-axonal compartment

In Figure 6.6, the relation between the estimated value of the orientation parameter using the extra-axonal signal from MCDC and the ground-truth orientation parameter from the substrate is illustrated. The estimation of the orientation parameter is similar over several angular dispersions close to 0°. This could be explained by several reasons,

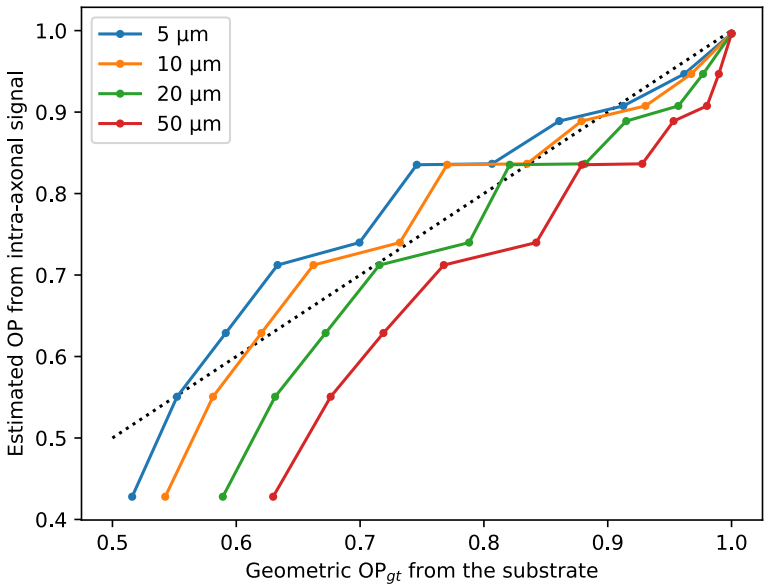

Figure 6.5 – Estimated OP from the intra-axonal signal as a function of the geometric orientation parameter OP_{gt}. The geometric OP is generated for four segment lengths, $\lambda \in \{5, 10, 20, 50\}$µm. The dotted line correspond to the function $x = y$.

for example, it could be linked with the apparition of trapped water around the axons with small displacement of the fibers. This plateau could also be more or less important due to the packing of the substrate. Overall, when the angular dispersion is sufficiently large, we observe the same general trend as that observed for the intra-axonal signal.

6.3 Conclusion

In this chapter, we explored the relation between the angular dispersion of realistic white matter numerical substrates using Monte Carlo simulations and the orientation parameter estimated with the QTI framework. Here, the results are shown for an angular dispersion from 0° to 25°. While we only focused on the relationship between angular dispersion and orientation parameter, we experimented both with the signal from the intra-axonal compartment as well as the signal from the extra-axonal compartment. In our case, we decided not add the possibility for water molecules to go from one compartment to the other. Hence, any behaviour resulting from this phenomenon cannot be seen in the experiments but could be investigated in future work. Using different substrates, we could investigate in a similar fashion the relation between other parameters from the DTD model and the substrate characteristics. For that, we could generate new substrate changing the

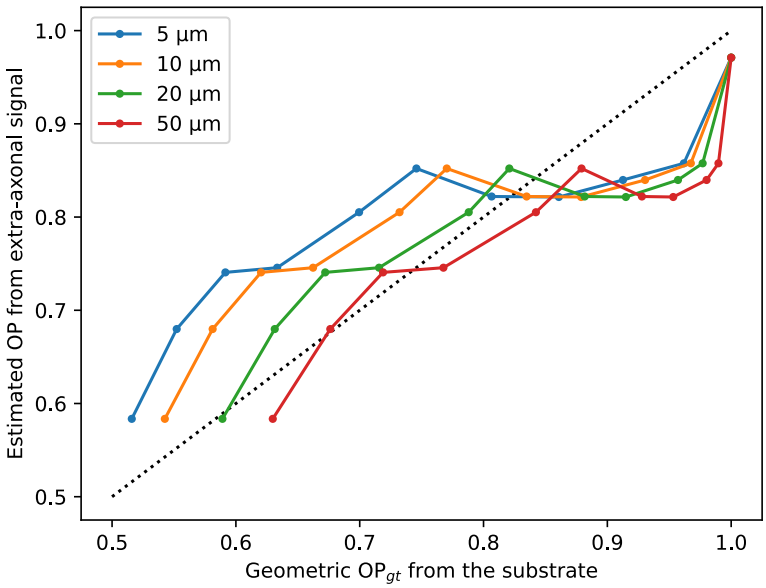

Figure 6.6 – Estimated OP from the extra-axonal signal as a function of the geometric orientation parameter OP_{gt}. The geometric OP is generated for four segment length: in blue, the segment length is set at 5µm; in orange, the segment length is set at 10µm; in green, the segment length is set at 20µm and in red, the segment length is set at 50µm. The dotted line correspond to the function $y = x$.

packing of the substrates or the radii distribution used to generate the fibers.

Chapter 7

Multidimensional dMRI on tractography

Diffusion MRI enables the reconstruction of white matter pathways through tractography, providing a powerful framework for studying brain connectivity. However, tractography algorithms are known to generate a substantial number of false-positive streamlines, which limits the anatomical specificity and reliability of the resulting tractograms. Filtering approaches have been proposed to mitigate this issue by enforcing consistency between the reconstructed streamlines and the measured diffusion signal.

Among these methods, COMMIT (Daducci, Dal Palù, et al. 2015) formulates tractogram filtering as a forward modeling problem, where the diffusion signal is expressed as a combination of contributions associated with individual streamlines and compartments. While this framework has proven effective in reducing false positives, its performances remains fundamentally tied to the expressiveness of the underlying signal model. In particular, when relying on conventional linear diffusion encoding, different streamline configurations may produce similar signal predictions, limiting the ability of the model to discriminate between plausible and implausible structures.

Compared to conventional linear encoding, b-tensor acquisitions provide additional contrasts that capture complementary aspects of the diffusion process. In particular, they increase sensitivity to features such as microscopic anisotropy and orientation dispersion, which are not fully resolved with standard encoding. This raises the question of whether such information can improve the constraint on the forward model in COMMIT and enhance the discrimination between competing streamline configurations.

In this chapter, we develop a numerical framework for substrate generation and diffusion signal simulation to explore the potential of b-tensor encoding for tractogram filtering. This framework enables controlled investigations of the effect of additional diffusion contrasts on the forward model. A preliminary analysis of their impact on tractogram filtering are also presented, with further developments to be addressed in future work.

The work presented in this chapter has been developed in collaboration with researchers from DICE lab in Verona, in particular Dr. Matteo Battochio and Dr. Alessandro Daducci, in the context of a research exchange with the opportunity to spend three months at the lab in Verona.

7.1 Generation of numerical phantoms and their associated signals: Phantomas

To investigate the relationship between microstructural properties and diffusion signals in a controlled setting, we rely on numerical substrate generation. In this work, we build upon Phantomas (Caruyer, Daducci, et al. 2014), a framework designed for the generation of synthetic white matter configurations at a scale comparable to a human brain (several centimeters) and corresponding diffusion signals. While this framework provides a flexible basis for simulation, certain assumptions limit its suitability for our study. In particular, the density of fibers is defined at the voxel level rather than at the level of individual fiber populations. This constraint can lead to inconsistencies in regions with crossing configurations, where multiple fiber bundles share the same voxel.

To address this limitation, we introduce modifications to the substrate generation process that allow density to be controlled at the level of individual fiber populations. We additionally incorporate explicit control over the radius of each fiber bundle, enabling independent adjustment of bundle size and density. The objective is to simulate fanning configurations, with consistent intra-axonal cross-sectional surface along the bundle. These modifications allow the generation of substrates with controlled geometry and density, ensuring that crossing bundles maintain realistic relative sizes and packing.

The numerical substrate is described in a JSON file. In this file, the geometry of each fiber is described by *control points* describing the trajectory of the centerline of the bundle and *radii* at each control point. The trajectory of the bundle is computed using cubic splines. The microstructure configuration within the bundle is controlled by a *max density*, corresponding to the intra-axonal density of the bundle at the position where the radius is smallest. The density is computed at every point using the maximal density and radii. An example of a simple json file and the associated phantom can be seen in Figure 7.1.

In order to compute the signal from the phantom, we first compute *fiber orientation distribution functions* (fODF) for each fiber. These are estimated from a discrete set of

```
{
  "fiber_geometries" : {
    "fiber1": {
      "control_points":
        [0, 0, -10,
         0, 0, -4,
         0, 0, 0,
         0, 0, 4,
         0, 0, 10],
      "radii": [2.5, 2.5, 4.0, 2.5, 2.5],
      "max_density": 0.6
    },
    "fiber2": {
      "control_points":
        [-10, 0, 0,
         -4, 0, 0,
         0, 0, 0,
         4, 0, 0,
         10, 0, 0],
      "radii": [2.5, 2.5, 4.0, 2.5, 2.5],
      "max_density": 0.6
    }
  }
}

```

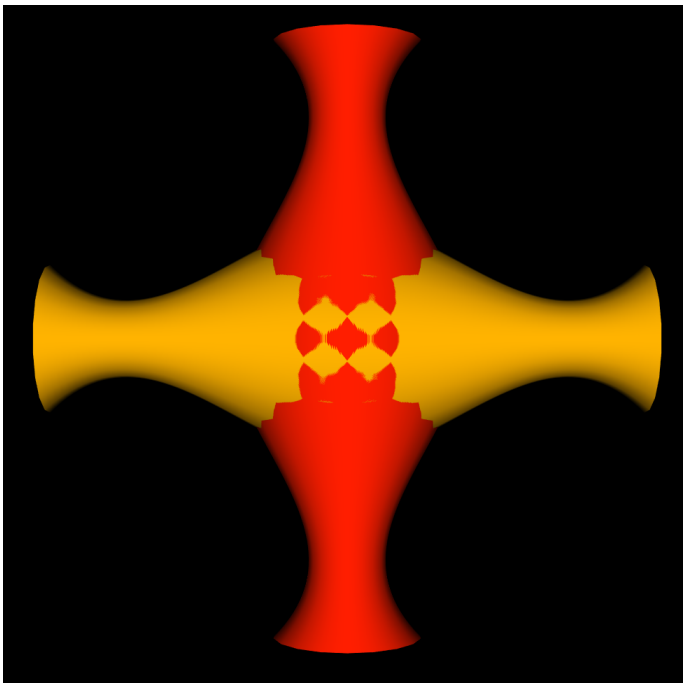

Figure 7.1 – Example of a simple phantom generated using this modified version of Phantomas. On the left, the json file with the definition of the two fibers. Lines 3 to 12 describe the first fiber corresponding to the red fiber of the right. Lines 13 to 22 corresponds to the second fiber, in yellow in the right.

weighted directions by constructing a smooth function on the sphere via a kernel density estimation, using a symmetric Von-Mises-Fisher distribution kernel. This distribution is then represented in the spherical harmonics (SH) basis.

Then, we have to generate the signal from an acquisition scheme. We allow in our code for three types of acquisition schemes. The first one corresponds to an acquisition scheme defined by a set of b-values and diffusion-weighting gradient directions, called b-vectors. The second one corresponds to the acquisition schemes using b-values, b-vectors as well as δ and Δ. Here δ corresponds to the duration of the each pulse and Δ is the time between the two gradient pulses. The last one corresponds to b-tensor encoding. We decided to only allow for b-tensors with a cylindrical symmetry. These can be characterized using the two eigenvalues $b_{||}$ corresponding to the eigenvector parallel to the main encoding direction and $b_{\perp}$ corresponding to the eigenvalue associated to the plane orthogonal to the main encoding direction. Thus, we settled on an acquisition scheme describing each acquisition using the eigenvalues, $b_{||}$ and $b_{\perp}$. The first three columns of the acquisition scheme correspond to the b-vectors, the fourth to $b_{||}$ and the fifth to $b_{\perp}$.

The diffusion-weighted signal is then computed from these fODFs in the spherical harmonics domain for each acquisition shell in the acquisition scheme, where a *shell* is defined by a unique pair of $b_{||}$ and $b_{\perp}$. Regarding the intra-axonal signal, a response function is estimated for each shell, modeling the signal arising from a single fiber population, and expressed in the SH basis. This signal may be computed using either a stick model or an impermeable cylinder model, as described in Section 2.3. The convolution between the fODF and this response function is performed in SH space as a coefficient-wise multiplication. The resulting SH coefficients are then projected onto the measurement directions using the SH basis, yielding the signal contribution for each fiber. The final diffusion signal is obtained by summing the contributions of all fiber populations across all shells.

While the convolution described above is well adapted to the intra-axonal signal, the generation of the extra-axonal signal is less straightforward and is yet to be implemented in our code. If we model the extra-axonal compartment with a zeppelin, it is generally assumed that the anisotropy of the extra-axonal compartment is related to the density, via a tortuosity model. When only one fiber population is in the voxel, we can consider that the volume fraction of the voxel attributed to the extra-axonal compartment is the volume of the voxel minus the volume from the intra-axonal compartment. However, when two or more fiber populations are in the voxel, the repartition needs to be different. We decided that we would compute the volume of all intra-axonal compartments and compute the proportion of each fiber population in that volume. That proportion would then be repercuted on the proportion for the extra-axonal volume. So if a fiber population takes 20% of the intra-axonal volume, it will also have 20% of the extra-axonal volume.

7.2 Adapting AMICO and COMMIT to b-tensor encoded acquisitions

After generating our phantoms and the intra-axonal signal, we focused on adapting COMMIT (cf. 4.4) to allow a b-tensor encoded acquisition scheme. In the COMMIT (Daducci, Dal Palù, et al. 2015) code, acquisition schemes are treated in AMICO (Daducci, Erick J. Canales-Rodríguez, et al. 2015) code, hence, our modifications were in that code. While COMMIT aims to filter the tractogram in order to determine which fibers are supported by the data, AMICO aims at explaining microstructure parameters from the data.

The first step is to allow for b-tensor acquisition schemes to be read. We decided to

allow only cylindrical b-tensors as we did for Phantomas. The format of the acquisition scheme remains the same also. The first three columns correspond to the b-vectors, the fourth column corresponds to $b_{||}$ and the last to $b_{\perp}$. One or more directions of the b-vectors may require a flip from the scheme used in Phantomas.

Once the acquisition scheme is read, the signal can be computed. In the current version, we implemented signal generation using a multi-compartment model which is derived from the diffusion tensor. This includes the stick-zeppelin-ball model (see Section 2.3.3).

7.3 Testing b-tensor encoded acquisition for tractography filtering

The generation of tractograms is a necessary step to compute results from COMMIT. The tractography could be done using b-tensor encoded acquisitions but we decided against in order to be able to compare filtered tractograms to state-of-the-art results more easily, without interference from b-tensors on this step. Two alternative strategies can be explored to generate those tractograms. The first one consists in generating tractograms for a separate acquisition scheme, independent from the one using b-tensors. The second strategy relies on generating a tractogram directly from the description of the phantom geometry. This is the one we selected in the preliminary experiment. For each fiber bundle, we generate a given number of streamlines using an hexagonal grid on the plane perpendicular to the direction of the bundle. This grid was transported along the centerline of the bundle, adjusting the distance between each streamline to follow the modification of the bundle's radius.

One of COMMIT's output is the density map of the filtered tractogram. In the initial version of Phantomas, the density was set at 0.4 for all voxels, no matter its configuration. Hence, the density map truly associated to the signal corresponded to a uniform value over the entire fiber mask. In our version, we now have the density of each voxel computed as the sum of the density of each bundle in it. This allows for a more realist density map, similarly to the one computed by COMMIT. Figure 7.2 shows the density map computed by COMMIT on our substrate in axial, sagittal and coronal views. In this figure, we can see an increase of the density in regions where the bundle has a smaller radius.

As we have access to the ground truth, verifying the connections between regions of interest (ROIs) can provide a practical way to assess the quality of both unfiltered and filtered tractograms. The connectivity analysis can ensure that major bundles are

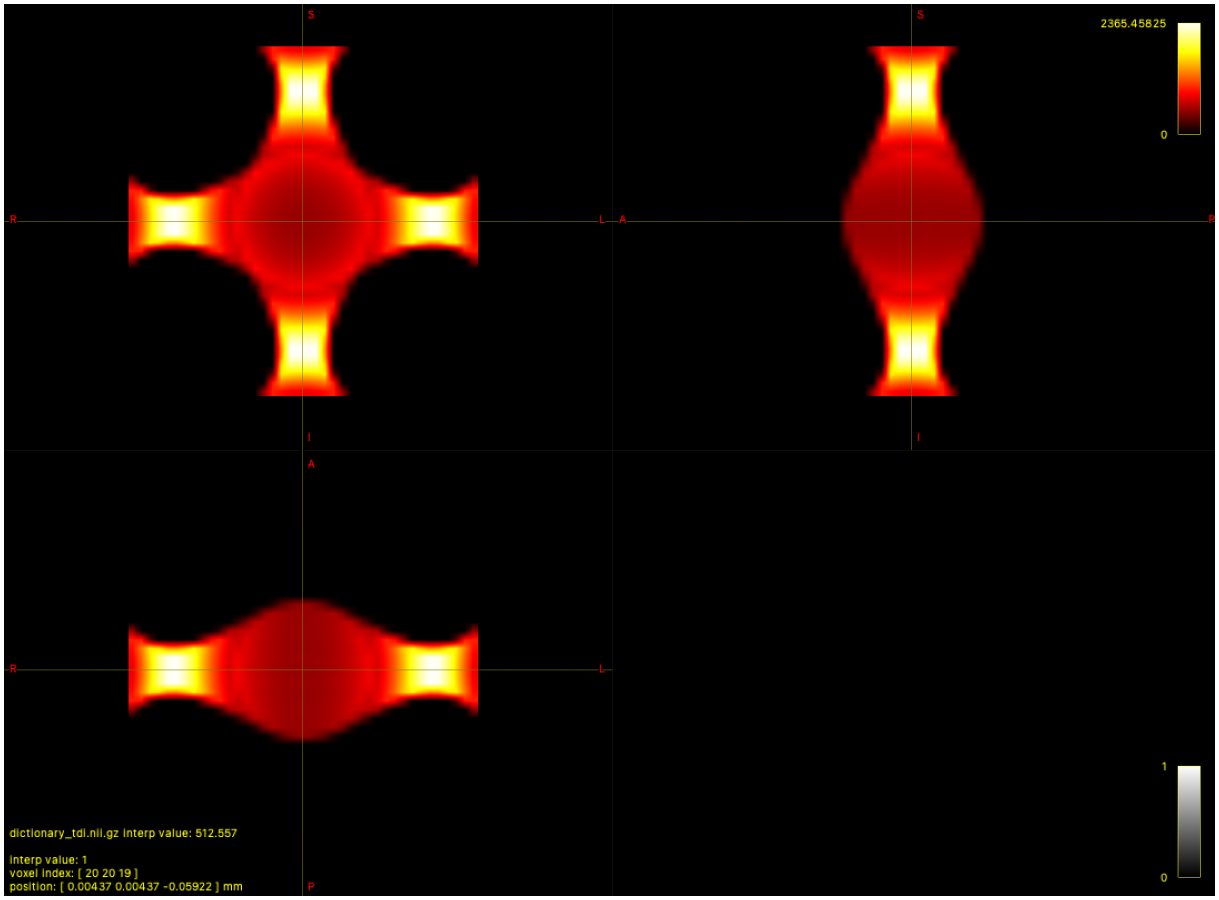

Figure 7.2 – Density map generated through COMMIT on a substrate generated using the modified Phantomas, shown in axial, sagittal and coronal views. White values corresponds to high density zones. Red corresponds to lower density zones.

correctly represented and that false-positive connections are reduced. For the phantom presented in this chapter, the filtering using b-tensors acquisitions and linear acquisition (results not reported) yield very similar results due to its simplicity.

7.4 Discussion and conclusion

In this chapter, the aim was to adapt Phantomas in order to create a more realistic digital phantom in order to evaluate the effect of b-tensor encoded acquisitions on the filtering of tractograms. We have implemented the creation of the digital phantom as well as the intra-axonal signal generated by each bundle. COMMIT was adapted in order to be able to use b-tensor encoded acquisitions when generating the resulting signal for each

bundle. However, in order to properly test the effect of such an acquisition scheme, we still need to implement the extra-axonal signal generated by the phantom. It is also important to note that the current framework only support b-tensors with a cylindrical symmetry. Although they are the most commonly used b-tensors in the literature, some groups have started exploring the use of more general b-tensors.

More complex phantoms also need to be implemented as the filtering of COMMIT already produces really good results in many cases. Such a phantom would most likely require kissing fibers, fanning in a bundle as well as several bundle crossings or important bending in a bundle. Last, it would also be of interest to include b-tensor acquisitions from the tractography step as used in K. Magdoom et al. (2021) and K. N. Magdoom et al. (2023).

Part IV

Conclusion

Conclusion

Contributions

This thesis addresses the design and analysis of diffusion MRI acquisition schemes with the objective of improving the sensitivity of the measured signal to tissue microstructure while accounting for practical constraints such as the acquisition time and signal quality. Throughout this thesis, we have explored the links between acquisition design and signal modeling in order to determine the reliability and interpretability of diffusion MRI measurements.

Our first contribution described in chapter 5, introduced a framework for the optimization of acquisition schemes tailored to the estimation of parameters of interest within a given model. We focused on the diffusion tensor distribution (DTD) model. The proposed approach relies on the construction of a signal dictionary. In order to build it, we first selected a collection of acquisition measurements, here a collection of b-tensors along with an associated set of directions. By partitioning the model parameters space according to the achievable sensitivity, we were able to define a collection of models. Using both the superset of acquisition parameters and the collection of models, we were able to generate the associated diffusion signal that would be generated for each model using each acquisition. This generates a dictionary of signals where each line corresponds to an acquisition and each column corresponds to a model. The goal then became the selection of the lines, here our acquisitions, that maximize the differences between the columns, here our models. Several methods can be used to do that selection and we were able to get similar or better results than those by acquisition schemes from the litterature for the estimation of our model parameters. We also tested several potential improvement extensions.

With this framework, we optimized the estimation for a set of parameters of interest for our model. However, translating those parameters to information about the microstructure is not as straightforward as we would like. Hence, the contribution in chapter 6. In this chapter, we decided to investigate the link between the orientation parameter of the DTD and the angular dispersion of a single fiber population substrate of white matter. We generated our substrates using CACTUS. In order to investigate the link between the

two parameters, we simulated the diffusion process in the substrate using Monte-Carlo simulation with a set of gradient waveforms corresponding to the decided b-tensors.

Until then, we only focused on the results at the voxel size. However, many studies using diffusion MRI focus on whole brain applications such as tractography. To date, b-tensor encoded acquisitions have not been thoroughly assessed when it comes to tractography and their advantages and limitations in this context remains fairly unexplored. To evaluate the effect of b-tensor encoded acquisitions on the filtering of tractography, we first decided to tackle the issue of the validation. In order to do that, we started the implementation of a tool to generate simple phantoms. This tool is an extension of Phantomas, we enriched the software with the possibility to have fiber bundles with varying radii, the possibility of creating fanning and crossing tracts or to have density maps that reflect the amount of fibers at each voxel. We implemented the possibility to generate more complex substrates in order to test b-tensor encoded acquisitions in COMMIT. Currently, only the intra-axonal signal can be generated. The generation of the extra-axonal contribution is discussed in the chapter. We also adapted COMMIT code in order to read and use b-tensor encoded acquisition schemes.

Perspectives

Several perspectives emerge from this work and open directions for future research. First, the optimization framework proposed in chapter 5 could be extended to alternative models beyond the DTD as long as the number of parameters of interest for this new model remains manageable. In a similar fashion, this framework could also be used for another type of acquisition than the one we selected: the b-tensors.

In chapter 6, we focused only on the relation between the orientation parameter of the model and the angular dispersion of the substrate. However, there are still many parameters on both end that can impact the understanding of the metrics extracted from the model. It would be interesting to study the effect of several parameters of the substrates and their effects on diverse parameters from our models. For example, it would be interesting to see how the packing of the substrate influences the microscopic anisotropy. This would allow for a more comprehensive characterization of the links between model-derived quantities and underlying microstructure.

From an acquisition standpoint, an important aspect that was not explored in this work is the fact that a given b-tensor can be implemented through multiple gradient

waveforms. These different realizations may exhibit distinct sensitivities to diffusion time, relaxation effects or hardware constraints and should therefore be taken into account when designing optimized acquisition schemes. More generally, incorporating waveform design into the optimization process represents a crucial direction.

Regarding chapter 7 and more specifically the testing of b-tensor acquisitions on filtering tractograms, the creation of a complex phantom is needed. Such a phantom would require crossing, fanning, kissing or bending that would lead to a difficult identification using linear encoded acquisitions. Another natural extension in the context of tractography would be to use b-tensor acquisitions when generating the tractogram (K. Magdoom et al. 2021; K. N. Magdoom et al. 2023).

Finally, it is important to note that different software implementations rely on distinct conventions to describe b-tensors. This can lead to complications while designing a processing pipeline, especially as some implementation allow for only part of b-tensors encoded acquisitions to be used such as only b-tensors with a cylindrical symmetry.

PUBLICATIONS

Étude de l'effet du bruit sur l'estimation de l'anisotropie microscopique en IRM de diffusion

Bocquillon, C., Lapert, M., Bannier, E., Corouge, I. & Caruyer, E. (2023, March)

In SFRMBM2023 - Sixième congrès de la Société Française de Résonance Magnétique en Biologie et Médecine.

Orientation dispersion estimated from multidimensional diffusion MRI: does it match simulated realistic microstructure?

Bocquillon, C., Villarreal Haro, J.L., Rafael-Patino, J., Thiran, J.P., Corouge, I. & Caruyer, E. (2024, October)

In ESMRMB 2024 - 40th Annual Meeting Scientific European Society for Magnetic Resonance in Medecine and Biology.

Optimization of acquisition schemes towards a better estimation of microstructure parameters in diffusion MRI

Bocquillon, C., Corouge, I. & Caruyer, E. (2025, February)

In ISMRM 2025 - Workshop on 40 years of diffusion: Past, Present & Future Perspectives

Optimisation de schémas d'acquisition pour une meilleure estimation des paramètres de microstructure en IRM de diffusion

Bocquillon, C., Corouge, I. & Caruyer, E. (2025, March)

In SFRMBM 2025 - 7ème Congrès de la Société Française de Résonance Magnétique en Biologie et Médecine.

Optimization of Acquisition Schemes Towards a Better Estimation of Microstructure Parameters in Multidimensional Diffusion MRI

Bocquillon, C., Corouge, I. & Caruyer, E. (2025)

In International Conference on Information Processing in Medical Imaging (pp. 142-153). Springer

List of Figures

1.1 Displacement of pollen particles suspended in water. Illustration extracted from (Johansen-Berg and T. E. Behrens 2009). 26
1.2 Diffusion in free water (a) and in different plausible microscopic environments over time. (e) shows an example of diffusion in tissue where membranes are permeable. Figures from (Topgaard 2020). 27
1.3 Schematic representation of a spin-echo sequence presented by Carr and Purcell. Figure from Johansen-Berg and T. E. Behrens (2009) 28
1.4 Schematic representation of a pulsed gradient spin-echo sequence presented by Stejskal and Tanner. Figure from Johansen-Berg and T. E. Behrens (2009). 29

2.1 Sections of the human brain where myelin sheaths are stained with fluorescent dye DiI, visualized with confocal laser scanning microscopy. The scale bar represent 20μm. (a) Slice of subcortical white matter. (b) Slice of lateral thalamus. Figure from D. K. Jones (2010). 36
2.2 White matter sample from the corpus callosum of a monkey brain using 3D synchrotron X-ray nano-holomography. (left) Acquired volume where blood vessels, axons, vacuole and cell clusters are highlighted. (right) Segmented axons extracted from the sample. Figure adapted from Andersson et al. (2020). 37
2.3 Diagram of a neuron. Figure from US National Cancer Institute's Surveillance, Epidemiology and End Results (SEER) Program. 37
2.4 Schema of a diffusion tensor. Here, the eigenvalues are given by λ_1, λ_2 and λ_3, their associated eigenvectors are given by v_1, v_2 and v_3. 40
2.5 Examples of diffusion tensor distributions (DTD) with different parameters. 43
2.6 Effects of the orientation parameter (A), the microscopic anisotropy (B) and the size variance (C) on diffusion tensors distributions. (A) Effect of the orientation parameter with μFA set at 0.5 and C_{MD} at 0. (B) Effect of the microscopic anisotropy with C_{MD} set at 0 and OP at 0.8. (C) Effect of the size variance on DTDs with μFA fixed at 0.5 and OP at 0.5. 49

2.7 Examples of digital phantoms describing whole-brain connectivity between regions of interest. (left) Digital phantom generated using Phantomas (Caruyer, Daducci, et al. 2014) for the 2nd HARDI reconstruction challenge at ISBI 2013. (right) Example of the FiberCup phantom generated using FiberFox in (Peter F. Neher et al. 2014). 58

2.8 Examples of digital phantoms describing complex and realistic microstructure at the size of a voxel or under. (left) Figure from (Villarreal-Haro et al. 2023) of a digital phantom generated using CACTUS. (middle) Figure from (Ginsburger et al. 2019) of one phantom generated using MEDUSA. (right) Figure from (Callaghan et al. 2020) of one phantom generated using ConFiG. 59

3.1 The top row shows an icosahedron, a dodecahedron and a truncated icosahedron. The bottom row shows how they can be combined to form a uniform distribution of points on the sphere. Figure from C. Westin, Pasternak, and H. Knutsson (2012). 66

3.2 Set of directions generated using the method presented in Caruyer, Lenglet, et al. (2013) with 30 points per shell and 3 shells. Figure from Caruyer, Lenglet, et al. (2013). 66

3.3 Schematic representation of a double diffusion encoding sequence. Figure adapted from Henriques et al. (2021). 68

3.4 Schematic representation of a triple diffusion encoding sequence. Figure adapted from Jensen and Helpern (2018). 69

3.5 Examples of three acquisitions with their gradient waveform in the first column, their trajectories in the gradient space in the second column and in q-space in the third, and their associated b-tensor in the fourth column. The first line corresponds to an acquisition using SDE. The second and third line correspond to two acquisitions using DDE. Figure from C.-F. Westin, Hans Knutsson, et al. (2016) 70

3.6 Examples of b-tensors with a cylindrical symmetry, showing an example for each of the five shapes defined by the relation between its eigenvalues. 72

3.7 Examples of gradient waveforms for each shape of b-tensor generated from an efficient isotropic diffusion encoding gradient (C). The first column shows the gradient waveforms. The second the associated gradient trajectory with color coding slew rate. The third is the associated gradient trajectory in q-space. The last one represents the associated b-tensor. On line (A) is an example of linear b-tensor, line (B) an example of a prolate b-tensor, line (C) shows an example of a spherical b-tensor, line (D) corresponds to an oblate b-tensor and finally line (E) illustrates a planar b-tensor. Figure from C.-F. Westin, Hans Knutsson, et al. (2016) 73

4.1 (left) Tractogram generated with MRtrix3 of a digital phantom created with Phantomas (Caruyer, Daducci, et al. 2014). (right) Associated connectivity matrix where each region of interest corresponds to the starting or ending point of a bundle of the digital phantom. 78

4.2 Examples of dODFs estimated with the open-source library "Diffusion Imaging In Python" (DIPY) (Garyfallidis et al. 2014). 79

4.3 Example of a tractogram of the human brain where the local streamline orientation is encoded by a color: red for left-right, green for antero-posterior and blue for superior-inferior. 81

4.4 Synthetic example to understand the principle of COMMIT using four voxels and a starting tractogram. The selected models are a stick for each streamline and a ball for each CSF compartment. y corresponds to the measured signal. Each value correspond to one voxel. A is the dictionary encoding each potential contribution for each streamline or CSF compartment. Each column corresponds to a potential contribution and each line to each voxel. x is the binary vector holding the information of which contribution is kept in the filtered tractogram. Figure from Schiavi et al. (2020) 83

4.5 Diffusion Tensor Distributions (first line) with their associated mean tensor (second line), covariance tensor (third line) and their ODF (fourth line) and μODF generated for different features of the DTD. Figure from K. Magdoom et al. (2021). 85

5.1 Overview of the different steps of the method, starting from the definition of the superset of acquisitions and the collection of DTD to the selection of the optimized acquisition set. 91

5.2 B-tensors selected in the superset of acquisitions characterized by their two eigenvalues $b_\perp$ and $b_{||}$. 92

5.3 Division of the parameter space in boxes of DTD with generated signal according to the achievable resolution. 95

5.4 OP estimation error on its full range. In blue, the reference scheme; in orange, the greedy algorithm result; in green, the permutation algorithm result. (top row) The signal was corrupted with a Rician noise at an SNR 30. (bottom row) The signal was not corrupted with any noise. (first column) µFA was set at a medium value. (second colomn) µFA was set at a high value. 97

5.5 µFA estimation error on its full range. In blue, the reference scheme; in orange, the greedy algorithm result; in green, the permutation algorithm result. (top row) The signal was corrupted with a Rician noise at an SNR 30. (bottom row) The signal was not corrupted with any noise. (first column) OP was set at a medium value. (second colomn) OP was set at a high value. 98

5.6 Number of directions computed for the b-tensors of interest. Dark blue and light blue corresponds to b-tensors requiring at least 6 directions. Green corresponds to b-tensors requiring at least 24 directions. Yellow corresponds to b-tensors requiring at least 47 directions. 101

5.7 OP estimation error on its full range. In blue, the reference scheme; in orange, the greedy algorithm result; in green, the permutation algorithm result; in red, the weighted greedy algorithm result. (top row) The signal was corrupted with a Rician noise at an SNR 30. (bottom row) The signal was not corrupted with any noise. (first column) µFA was set at a medium value. (second column) µFA was set at a high value. 103

5.8 µFA estimation error on its full range. In blue, the reference scheme; in orange, the greedy algorithm result; in green, the permutation algorithm result; in red, the weighted greedy algorithm result. (top row) The signal was corrupted with a Rician noise at an SNR 30. (bottom row) The signal was not corrupted with any noise. (first column) OP was set at a medium value. (second column) OP was set at a high value. 104

5.9 OP estimation error on its full range. In blue, the reference scheme; in orange, the greedy algorithm result with a L_∞ norm; in green, the global solution for the L_∞ norm; in red, the greedy algorithm result with a L_2 norm; in purple, the global solution for the L_2 norm. (top row) The signal was corrupted with a Rician noise at an SNR 30. (bottom row) The signal was not corrupted with any noise. (first column) µFA was set at a medium value. (second column) µFA was set at a high value. 107

5.10 µFA estimation error on its full range. In blue, the reference scheme; in orange, the greedy algorithm result with a L_∞ norm; in green, the global solution for the L_∞ norm; in red, the greedy algorithm result with a L_2 norm; in purple, the global solution for the L_2 norm. (top row) The signal was corrupted with a Rician noise at an SNR 30. (bottom row) The signal was not corrupted with any noise. (first column) OP was set at a medium value. (second column) OP was set at a high value. 108

6.1 Cropped numerical substrates generated using CACTUS (Villarreal-Haro et al. 2023). The intracellular volume fraction is set to 0.72; fibers have a gamma-distributed radius with a shape parameter $\kappa = 1$ and a mean radius of 2.5 μm. The angular dispersion is the only varying parameter. (top row) From left to right: 0°, 5° and 10°. (bottom row) From left to right: 15°, 20° and 25°. 110

6.2 Illustration of how the ground truth orientation parameter, OP_{gt}, is computed from the substrate. Each fiber trajectory (panel a) is cut into segments of equal length, λ (panels b and d). The population of segment directions (panels c and e) is then converted into a distribution of rank-1 tensors, from which we compute OP_{gt}. For clarity, a single fiber trajectory is depicted here, but the process is performed in general for the whole substrate. 112

6.3 Gradient trajectory for the spherical b-tensor used to generate the gradient trajectories for the acquisition scheme. 113

6.4 Geometric OP_{gt}, corresponding to the estimation of the OP from the substrate, as a function of the angular dispersion in degrees from the substrate. The geometric OP is generated for four segment lengths $\lambda \in [5\mu\text{m}, 50\mu\text{m}]$. . 115

6.5 Estimated OP from the intra-axonal signal as a function of the geometric orientation parameter OP_{gt}. The geometric OP is generated for four segment lengths, $\lambda \in \{5, 10, 20, 50\}$µm. The dotted line correspond to the function $x = y$. 116
6.6 Estimated OP from the extra-axonal signal as a function of the geometric orientation parameter OP_{gt}. The geometric OP is generated for four segment length: in blue, the segment length is set at 5µm; in orange, the segment length is set at 10µm; in green, the segment length is set at 20µm and in red, the segment length is set at 50µm. The dotted line correspond to the function $y = x$. 117

7.1 Example of a simple phantom generated using this modified version of Phantomas. On the left, the json file with the definition of the two fibers. Lines 3 to 12 describe the first fiber corresponding to the red fiber of the right. Lines 13 to 22 corresponds to the second fiber, in yellow in the right. 121
7.2 Density map generated through COMMIT on a substrate generated using the modified Phantomas, shown in axial, sagittal and coronal views. White values corresponds to high density zones. Red corresponds to lower density zones. 124

BIBLIOGRAPHY

Aird-Rossiter, Charlie et al. (May 2024), « Tuneable Digital Phantoms for Grey Matter Modelling », *in*: DOI: 10.58530/2024/0591.

Alexander, Daniel C. (2008), « A general framework for experiment design in diffusion MRI and its application in measuring direct tissue-microstructure features », *in*: *Magnetic Resonance in Medicine* 60.*2*, pp. 439–448, DOI: https://doi.org/10.1002/mrm.21646, eprint: https://onlinelibrary.wiley.com/doi/pdf/10.1002/mrm.21646, URL: https://onlinelibrary.wiley.com/doi/abs/10.1002/mrm.21646.

Alexander, Daniel C. et al. (2010), « Orientationally invariant indices of axon diameter and density from diffusion MRI », *in*: *NeuroImage* 52.*4*, pp. 1374–1389, ISSN: 1053-8119, DOI: https://doi.org/10.1016/j.neuroimage.2010.05.043, URL: https://www.sciencedirect.com/science/article/pii/S1053811910007755.

Andersson, Mariam et al. (Dec. 2020), « Axon morphology is modulated by the local environment and impacts the noninvasive investigation of its structure-function relationship », English, *in*: *Proceedings of the National Academy of Sciences of the United States of America* 117.*52*, pp. 33649–33659, ISSN: 0027-8424, DOI: 10.1073/pnas.2012533117.

Assaf, Yaniv and Peter J. Basser (2005), « Composite hindered and restricted model of diffusion (CHARMED) MR imaging of the human brain », *in*: *NeuroImage* 27.*1*, pp. 48–58, ISSN: 1053-8119, DOI: https://doi.org/10.1016/j.neuroimage.2005.03.042, URL: https://www.sciencedirect.com/science/article/pii/S1053811905002259.

Assaf, Yaniv, Tamar Blumenfeld-Katzir, et al. (2008), « Axcaliber: A method for measuring axon diameter distribution from diffusion MRI », *in*: *Magnetic Resonance in Medicine* 59.*6*, pp. 1347–1354, DOI: https://doi.org/10.1002/mrm.21577, eprint: https://onlinelibrary.wiley.com/doi/pdf/10.1002/mrm.21577, URL: https://onlinelibrary.wiley.com/doi/abs/10.1002/mrm.21577.

Basser, P.J., J. Mattiello, and D. LeBihan (1994), « MR diffusion tensor spectroscopy and imaging », *in*: *Biophysical Journal* 66.*1*, pp. 259–267, ISSN: 0006-3495, DOI: https:

//doi.org/10.1016/S0006-3495(94)80775-1, URL: https://www.sciencedirect.com/science/article/pii/S0006349594807751.

Basser, Peter J. and Derek K. Jones (2002), « Diffusion-tensor MRI: theory, experimental design and data analysis – a technical review », *in*: *NMR in Biomedicine* 15.*7-8*, pp. 456–467, DOI: https://doi.org/10.1002/nbm.783, eprint: https://analyticalsciencejournals.onlinelibrary.wiley.com/doi/pdf/10.1002/nbm.783, URL: https://analyticalsciencejournals.onlinelibrary.wiley.com/doi/abs/10.1002/nbm.783.

Basser, Peter J. and Sinisa Pajevic (2007), « Spectral decomposition of a 4th-order covariance tensor: Applications to diffusion tensor MRI », *in*: *Signal Processing* 87.*2*, Tensor Signal Processing, pp. 220–236, ISSN: 0165-1684, DOI: https://doi.org/10.1016/j.sigpro.2006.02.050, URL: https://www.sciencedirect.com/science/article/pii/S0165168406001678.

Basser, Peter J., Sinisa Pajevic, et al. (2000), « In vivo fiber tractography using DT-MRI data », *in*: *Magnetic Resonance in Medicine* 44.*4*, pp. 625–632.

Basser, Peter J. and Carlo Pierpaoli (1996), « Microstructural and Physiological Features of Tissues Elucidated by Quantitative-Diffusion-Tensor MRI », *in*: *Journal of Magnetic Resonance, Series B* 111.*3*, pp. 209–219, ISSN: 1064-1866, DOI: https://doi.org/10.1006/jmrb.1996.0086, URL: https://www.sciencedirect.com/science/article/pii/S1064186696900862.

Bates, Alice, Alessandro Daducci, and Emmanuel Caruyer (May 2019), « Multi-Dimensional Diffusion MRI Sampling Scheme: B-tensor Design and Accurate Signal Reconstruction », *in*: *ISMRM 2019 - 27th Annual Meeting & Exhibition*, Montréal, Canada, pp. 1–4, URL: https://inserm.hal.science/inserm-02065830.

Bates, Alice, Alessandro Daducci, Parastoo Sadeghi, et al. (June 2020), « A 4D Basis and Sampling Scheme for the Tensor Encoded Multi-Dimensional Diffusion MRI Signal », *in*: *IEEE Signal Processing Letters* 27, pp. 790–794, DOI: 10.1109/LSP.2020.2991832, URL: https://inserm.hal.science/inserm-02881980.

Behrens, T.E.J. et al. (2003), « Characterization and propagation of uncertainty in diffusion-weighted MR imaging », *in*: *Magnetic Resonance in Medicine* 50.*5*, pp. 1077–1088, DOI: https://doi.org/10.1002/mrm.10609, eprint: https://onlinelibrary.wiley.com/doi/pdf/10.1002/mrm.10609, URL: https://onlinelibrary.wiley.com/doi/abs/10.1002/mrm.10609.

Bloch, F. (Oct. 1946), « Nuclear Induction », *in*: *Phys. Rev.* 70 (7-8), pp. 460–474, DOI: 10.1103/PhysRev.70.460, URL: https://link.aps.org/doi/10.1103/PhysRev.70.460.

Bocquillon, Constance, Isabelle Corouge, and Emmanuel Caruyer (Mar. 2025a), « Optimisation de schémas d'acquisition pour une meilleure estimation des paramètres de microstructure en IRM de diffusion », *in*: *SFRMBM 2025 - 7ème Congrès de la Société Française de Résonance Magnétique en Biologie et Médecine*, Saint-Malo, France, p. 1, URL: https://hal.science/hal-05368961.

— (Feb. 2025b), *Optimization of acquisition schemes towards a better estimation of microstructure parameters in diffusion MRI*, ISMRM 2025 - Workshop on 40 years of diffusion: Past, Present & Future Perspectives, Poster, URL: https://hal.science/hal-05368999.

— (2025c), « Optimization of Acquisition Schemes Towards a Better Estimation of Microstructure Parameters in Multidimensional Diffusion MRI », *in*: *International Conference on Information Processing in Medical Imaging*, Springer, pp. 142–153.

Bocquillon, Constance, Marc Lapert, et al. (Mar. 2023), *Étude de l'effet du bruit sur l'estimation de l'anisotropie microscopique en IRM de diffusion*, SFRMBM 2023 - Sixième congrès de la Société Française de Résonance Magnétique en Biologie et Médecine, Poster, URL: https://inria.hal.science/hal-04072656.

Bocquillon, Constance, Juan Luis Villarreal Haro, et al. (Oct. 2024), « Orientation dispersion estimated from multidimensional diffusion MRI: does it match simulated realistic microstructure? », *in*: *ESMRMB 2024 - 40th Annual Meeting cientific European Society for Magnetic Resonance in Medecine and Biology*, Barcelone, Spain, pp. 1–5, URL: https://hal.science/hal-04795839.

Brown, Robert (1828), « A brief account of microscopical observations on the particles contained in the pollen of plants and the general existence of active molecules in organic and inorganic bodies. », *in*: *Edinburgh New Philosophical Journal*, pp. 358–371.

Callaghan, Ross et al. (2020), « ConFiG: Contextual Fibre Growth to generate realistic axonal packing for diffusion MRI simulation », *in*: *NeuroImage* 220, p. 117107, ISSN: 1053-8119, DOI: https://doi.org/10.1016/j.neuroimage.2020.117107, URL: https://www.sciencedirect.com/science/article/pii/S1053811920305930.

Canales-Rodríguez, Erick Jorge et al. (2010), « Deconvolution in diffusion spectrum imaging », *in*: *NeuroImage* 50.*1*, pp. 136–149, ISSN: 1053-8119, DOI: https://doi.org/

10.1016/j.neuroimage.2009.11.066, URL: https://www.sciencedirect.com/science/article/pii/S105381190901252X.

Carr, H. Y. and E. M. Purcell (May 1954), « Effects of Diffusion on Free Precession in Nuclear Magnetic Resonance Experiments », *in*: *Phys. Rev.* 94 (3), pp. 630–638, DOI: 10.1103/PhysRev.94.630, URL: https://link.aps.org/doi/10.1103/PhysRev.94.630.

Caruyer, Emmanuel, Alessandro Daducci, et al. (May 2014), « Phantomas: a flexible software library to simulate diffusion MR phantoms », *in*: *ISMRM*, Milan, Italy, URL: https://inria.hal.science/hal-00944644.

Caruyer, Emmanuel, Christophe Lenglet, et al. (Apr. 2013), « Design of multishell sampling schemes with uniform coverage in diffusion MRI », *in*: *Magnetic Resonance in Medicine* 69.*6*, pp. 1534–1540, DOI: 10.1002/mrm.24736, URL: https://inria.hal.science/hal-00821688.

Cetin Karayumak, Suheyla, Evren Özarslan, and Gozde Unal (2018), « Asymmetric Orientation Distribution Functions (AODFs) revealing intravoxel geometry in diffusion MRI », *in*: *Magnetic Resonance Imaging* 49, pp. 145–158, ISSN: 0730-725X, DOI: https://doi.org/10.1016/j.mri.2018.03.006, URL: https://www.sciencedirect.com/science/article/pii/S0730725X18300316.

Cook, P. A. et al. (2006), « Camino: Open-Source Diffusion-MRI Reconstruction and Processing », *in*: *14th Scientific Meeting of the International Society for Magnetic Resonance in Medicine*, Seattle, WA, USA.

Cory, D. G. (1990), « Measurement of translational displacement probabilities by NMR: An indicator of compartmentation », *in*: *Magnetic Resonance in Medicine* 14.*3*, pp. 435–444, DOI: https://doi.org/10.1002/mrm.1910140303, eprint: https://onlinelibrary.wiley.com/doi/pdf/10.1002/mrm.1910140303, URL: https://onlinelibrary.wiley.com/doi/abs/10.1002/mrm.1910140303.

Daducci, Alessandro, Erick J. Canales-Rodríguez, et al. (2015), « Accelerated Microstructure Imaging via Convex Optimization (AMICO) from diffusion MRI data », *in*: *NeuroImage* 105, pp. 32–44, ISSN: 1053-8119, DOI: https://doi.org/10.1016/j.neuroimage.2014.10.026, URL: https://www.sciencedirect.com/science/article/pii/S1053811914008519.

Daducci, Alessandro, Alessandro Dal Palù, et al. (2015), « COMMIT: Convex Optimization Modeling for Microstructure Informed Tractography », *in*: *IEEE Transactions on Medical Imaging* 34.*1*, pp. 246–257, DOI: 10.1109/TMI.2014.2352414.

Daducci, Alessandro and Simona Schiavi (2025), « Quantitative tractography: joys and sorrows », *in*: *Brain Structure and Function* 230, p. 88, DOI: 10.1007/s00429-025-02939-z.

Delsarte, Philippe, Jean-Marie Goethals, and Johan Jacob Seidel (1977), « Spherical codes and designs », *in*: *Geometry and Combinatorics*.

Descoteaux, Maxime, Elaine Angelino, et al. (2007), « Regularized, fast, and robust analytical Q-ball imaging », *in*: *Magnetic Resonance in Medicine* 58.*3*, pp. 497–510, DOI: https://doi.org/10.1002/mrm.21277, eprint: https://onlinelibrary.wiley.com/doi/pdf/10.1002/mrm.21277, URL: https://onlinelibrary.wiley.com/doi/abs/10.1002/mrm.21277.

Descoteaux, Maxime, Rachid Deriche, et al. (2009), « Deterministic and Probabilistic Tractography Based on Complex Fibre Orientation Distributions », *in*: *IEEE Transactions on Medical Imaging* 28.*2*, pp. 269–286, DOI: 10.1109/TMI.2008.2004424.

Desikan, Rahul S et al. (2006), « An automated labeling system for subdividing the human cerebral cortex on MRI scans into gyral based regions of interest », *in*: *Neuroimage* 31.*3*, pp. 968–980.

Destrieux, Christophe et al. (2010), « Automatic parcellation of human cortical gyri and sulci using standard anatomical nomenclature », *in*: *Neuroimage* 53.*1*, pp. 1–15.

Drobnjak, Ivana, Bernard Siow, and Daniel C. Alexander (2010), « Optimizing gradient waveforms for microstructure sensitivity in diffusion-weighted MR », *in*: *Journal of Magnetic Resonance* 206.*1*, pp. 41–51, ISSN: 1090-7807, DOI: https://doi.org/10.1016/j.jmr.2010.05.017, URL: https://www.sciencedirect.com/science/article/pii/S1090780710001606.

Durantel, Thomas et al. (2025), « A Riemannian framework for incorporating white matter bundle priors in ODF-based tractography algorithms. », *in*: *PLoS One*, pp. 1–10.

Einstein, Albert (1905), « Investigations on the theory of the Brownian movement », *in*.

Eriksson, Stefanie et al. (Mar. 2015), « NMR diffusion-encoding with axial symmetry and variable anisotropy: Distinguishing between prolate and oblate microscopic diffusion tensors with unknown orientation distribution », *in*: *The Journal of Chemical Physics* 142.*10*, p. 104201, ISSN: 0021-9606, DOI: 10.1063/1.4913502, URL: https://doi.org/10.1063/1.4913502.

Fick, Rutger H.J. et al. (2016), « MAPL: Tissue microstructure estimation using Laplacian-regularized MAP-MRI and its application to HCP data », *in*: *NeuroImage* 134, pp. 365–

385, ISSN: 1053-8119, DOI: https://doi.org/10.1016/j.neuroimage.2016.03.046, URL: https://www.sciencedirect.com/science/article/pii/S1053811916002512.

Garyfallidis, Eleftherios et al. (2014), « Dipy, a library for the analysis of diffusion MRI data », *in*: *Frontiers in Neuroinformatics* Volume 8 - 2014, ISSN: 1662-5196, DOI: 10.3389/fninf.2014.00008, URL: https://www.frontiersin.org/journals/neuroinformatics/articles/10.3389/fninf.2014.00008.

Gibbs, J. Willard (1898), « Fourier's Series », *in*: *Nature* 59.*200*.

Ginsburger, Kévin et al. (2019), « MEDUSA: A GPU-based tool to create realistic phantoms of the brain microstructure using tiny spheres », *in*: *NeuroImage* 193, pp. 10–24, ISSN: 1053-8119, DOI: https://doi.org/10.1016/j.neuroimage.2019.02.055, URL: https://www.sciencedirect.com/science/article/pii/S105381191930151X.

Gudbjartsson, HáKon and Samuel Patz (1995), « The rician distribution of noisy mri data », *in*: *Magnetic Resonance in Medicine* 34.*6*, pp. 910–914, DOI: https://doi.org/10.1002/mrm.1910340618, eprint: https://onlinelibrary.wiley.com/doi/pdf/10.1002/mrm.1910340618, URL: https://onlinelibrary.wiley.com/doi/abs/10.1002/mrm.1910340618.

Hahn, E. L. (Nov. 1950), « Spin Echoes », *in*: *Phys. Rev.* 80 (4), pp. 580–594, DOI: 10.1103/PhysRev.80.580, URL: https://link.aps.org/doi/10.1103/PhysRev.80.580.

Hansen, Brian et al. (2013), « Experimentally and computationally fast method for estimation of a mean kurtosis », *in*: *Magnetic Resonance in Medicine* 69.*6*, pp. 1754–1760, DOI: https://doi.org/10.1002/mrm.24743, eprint: https://onlinelibrary.wiley.com/doi/pdf/10.1002/mrm.24743, URL: https://onlinelibrary.wiley.com/doi/abs/10.1002/mrm.24743.

Hardin, R. and N. Sloane (July 2002), « McLaren's Improved Snub Cube and Other New Spherical Designs in Three Dimensions », *in*: *Discrete and Computational Geometry* 15, pp. 429–441, DOI: 10.1007/BF02711518.

Henriques, Rafael N. et al. (2021), « Double diffusion encoding and applications for biomedical imaging », *in*: *Journal of Neuroscience Methods* 348, p. 108989, ISSN: 0165-0270, DOI: https://doi.org/10.1016/j.jneumeth.2020.108989, URL: https://www.sciencedirect.com/science/article/pii/S016502702030412X.

Herberthson, Magnus et al. (2021), « Q-space trajectory imaging with positivity constraints (QTI+) », *in*: *NeuroImage* 238, p. 118198, ISSN: 1053-8119, DOI: https://

doi.org/10.1016/j.neuroimage.2021.118198, URL: https://www.sciencedirect.com/science/article/pii/S1053811921004754.

Jelescu, Ileana O. and Matthew D. Budde (2017), « Design and Validation of Diffusion MRI Models of White Matter », *in*: *Frontiers in Physics* Volume 5 - 2017, ISSN: 2296-424X, DOI: 10.3389/fphy.2017.00061, URL: https://www.frontiersin.org/journals/physics/articles/10.3389/fphy.2017.00061.

Jelescu, Ileana O., Alexandre de Skowronski, et al. (2022), « Neurite Exchange Imaging (NEXI): A minimal model of diffusion in gray matter with inter-compartment water exchange », *in*: *NeuroImage* 256, p. 119277, ISSN: 1053-8119, DOI: https://doi.org/10.1016/j.neuroimage.2022.119277, URL: https://www.sciencedirect.com/science/article/pii/S1053811922003986.

Jelescu, Ileana O., Marco Palombo, et al. (2020), « Challenges for biophysical modeling of microstructure », *in*: *Journal of Neuroscience Methods* 344, p. 108861, ISSN: 0165-0270, DOI: https://doi.org/10.1016/j.jneumeth.2020.108861, URL: https://www.sciencedirect.com/science/article/pii/S0165027020302843.

Jensen, Jens H. and Joseph A. Helpern (2018), « Characterizing intra-axonal water diffusion with direction-averaged triple diffusion encoding MRI », *in*: *NMR in Biomedicine* 31.*7*, e3930 NBM-17-0275.R2, e3930, DOI: https://doi.org/10.1002/nbm.3930, eprint: https://analyticalsciencejournals.onlinelibrary.wiley.com/doi/pdf/10.1002/nbm.3930, URL: https://analyticalsciencejournals.onlinelibrary.wiley.com/doi/abs/10.1002/nbm.3930.

Jensen, Jens H., Joseph A. Helpern, et al. (2005), « Diffusional kurtosis imaging: The quantification of non-gaussian water diffusion by means of magnetic resonance imaging », *in*: *Magnetic Resonance in Medicine* 53.*6*, pp. 1432–1440, DOI: https://doi.org/10.1002/mrm.20508, eprint: https://onlinelibrary.wiley.com/doi/pdf/10.1002/mrm.20508, URL: https://onlinelibrary.wiley.com/doi/abs/10.1002/mrm.20508.

Jeurissen, Ben et al. (2014), « Multi-tissue constrained spherical deconvolution for improved analysis of multi-shell diffusion MRI data », *in*: *NeuroImage* 103, pp. 411–426, ISSN: 1053-8119, DOI: https://doi.org/10.1016/j.neuroimage.2014.07.061, URL: https://www.sciencedirect.com/science/article/pii/S1053811914006442.

Jian, Bing et al. (2007), « A novel tensor distribution model for the diffusion-weighted MR signal », *in*: *NeuroImage* 37.*1*, pp. 164–176, ISSN: 1053-8119, URL: https://www.sciencedirect.com/science/article/pii/S105381190700273X.

Johansen-Berg, Heidi and Timothy E.J. Behrens (2009), *Diffusion MRI, From Quantitative Measurement to In vivo Neuroanatomy*, Elsevier, ISBN: 978-0-12-374709-9, DOI: https://doi.org/10.1016/B978-0-12-374709-9.X0001-6.

Jones, D.K., M.A. Horsfield, and A. Simmons (1999), « Optimal strategies for measuring diffusion in anisotropic systems by magnetic resonance imaging », *in*: *Magnetic Resonance in Medicine* 42.*3*, pp. 515–525, DOI: https://doi.org/10.1002/(SICI)1522-2594(199909)42:3<515::AID-MRM14>3.0.CO;2-Q, eprint: https://onlinelibrary.wiley.com/doi/pdf/10.1002/%28SICI%291522-2594%28199909%2942%3A3%3C515%3A%3AAID-MRM14%3E3.0.CO%3B2-Q, URL: https://onlinelibrary.wiley.com/doi/abs/10.1002/%28SICI%291522-2594%28199909%2942%3A3%3C515%3A%3AAID-MRM14%3E3.0.CO%3B2-Q.

Jones, Derek K. (Nov. 2010), *Diffusion MRI: Theory, Methods, and Applications*, Oxford University Press, ISBN: 9780195369779, DOI: 10.1093/med/9780195369779.001.0001, URL: https://doi.org/10.1093/med/9780195369779.001.0001.

Jones, Derek K. and Peter J. Basser (2004), « "Squashing peanuts and smashing pumpkins": How noise distorts diffusion-weighted MR data », *in*: *Magnetic Resonance in Medicine* 52.*5*, pp. 979–993, DOI: https://doi.org/10.1002/mrm.20283, eprint: https://onlinelibrary.wiley.com/doi/pdf/10.1002/mrm.20283, URL: https://onlinelibrary.wiley.com/doi/abs/10.1002/mrm.20283.

Jones, Derek K., Andrew Simmons, et al. (1999), « Non-invasive assessment of axonal fiber connectivity in the human brain via diffusion tensor MRI », *in*: *Magnetic Resonance in Medicine* 42.*1*, pp. 37–41.

Koay, Cheng Guan (2011), « A simple scheme for generating nearly uniform distribution of antipodally symmetric points on the unit sphere », *in*: *Journal of Computational Science* 2.*4*, pp. 377–381, ISSN: 1877-7503, DOI: https://doi.org/10.1016/j.jocs.2011.06.007, URL: https://www.sciencedirect.com/science/article/pii/S1877750311000615.

Koay, Cheng Guan and Peter J. Basser (2006), « Analytically exact correction scheme for signal extraction from noisy magnitude MR signals », *in*: *Journal of Magnetic Resonance* 179.*2*, pp. 317–322, ISSN: 1090-7807, DOI: https://doi.org/10.1016/j.jmr.2006.01.016, URL: https://www.sciencedirect.com/science/article/pii/S109078070600019X.

Lasič, Samo et al. (2014), « Microanisotropy imaging: quantification of microscopic diffusion anisotropy and orientational order parameter by diffusion MRI with magic-

angle spinning of the q-vector », *in*: *Frontiers in Physics* 2, ISSN: 2296-424X, DOI: 10.3389/fphy.2014.00011, URL: https://www.frontiersin.org/journals/physics/articles/10.3389/fphy.2014.00011.

Le Bihan, Denis and E. Breton (Dec. 1985), « Imagerie de diffusion in-vivo par résonance magnétique nucléaire », *in*: *Comptes-Rendus de l'Académie des Sciences* 93.*5*, pp. 27–34, URL: https://hal.science/hal-00350090.

Li, Jing-Rebecca et al. (2019), « SpinDoctor: A MATLAB toolbox for diffusion MRI simulation », *in*: *NeuroImage* 202, p. 116120, ISSN: 1053-8119, DOI: https://doi.org/10.1016/j.neuroimage.2019.116120, URL: https://www.sciencedirect.com/science/article/pii/S1053811919307116.

Magdoom, Kulam et al. (Feb. 2021), « A new framework for MR diffusion tensor distribution », *in*: *Scientific Reports* 11, DOI: 10.1038/s41598-021-81264-x.

Magdoom, Kulam Najmudeen et al. (2023), « A novel framework for in-vivo diffusion tensor distribution MRI of the human brain », *in*: *NeuroImage* 271, p. 120003, ISSN: 1053-8119, DOI: https://doi.org/10.1016/j.neuroimage.2023.120003, URL: https://www.sciencedirect.com/science/article/pii/S1053811923001490.

Maier-Hein, Klaus H et al. (2017), « The challenge of mapping the human connectome based on diffusion tractography », *in*: *Nature communications* 8.*1*, p. 1349.

Merboldt, Klaus-Dietmar, Wolfgang Hanicke, and Jens Frahm (1985), « Self-diffusion NMR imaging using stimulated echoes », *in*: *Journal of Magnetic Resonance (1969)* 64.*3*, pp. 479–486, ISSN: 0022-2364, DOI: https://doi.org/10.1016/0022-2364(85)90111-8, URL: https://www.sciencedirect.com/science/article/pii/0022236485901118.

Morez, Jan et al. (2023), « Optimal experimental design and estimation for q-space trajectory imaging », *in*: *Human Brain Mapping* 44.*4*, pp. 1793–1809, DOI: https://doi.org/10.1002/hbm.26175, eprint: https://onlinelibrary.wiley.com/doi/pdf/10.1002/hbm.26175, URL: https://onlinelibrary.wiley.com/doi/abs/10.1002/hbm.26175.

N. J. A. Sloane with the collaboration of R. H. Hardin, W. D. Smith et al. (n.d.[a]), « Tables of Spherical Codes », *in*: *published electronically at NeilSloane.com/packings/* ().

— (n.d.[b]), *Tables of Spherical Codes*, URL: NeilSloane.com/packings/.

Neher, Peter F. et al. (2014), « Fiberfox: Facilitating the creation of realistic white matter software phantoms », *in*: *Magnetic Resonance in Medicine* 72.*5*, pp. 1460–1470, DOI: https://doi.org/10.1002/mrm.25045, eprint: https://onlinelibrary.wiley.

com/doi/pdf/10.1002/mrm.25045, URL: https://onlinelibrary.wiley.com/doi/abs/10.1002/mrm.25045.

Özarslan, Evren et al. (2013), « Mean apparent propagator (MAP) MRI: A novel diffusion imaging method for mapping tissue microstructure », *in*: *NeuroImage* 78, pp. 16–32, ISSN: 1053-8119, DOI: https://doi.org/10.1016/j.neuroimage.2013.04.016, URL: https://www.sciencedirect.com/science/article/pii/S1053811913003431.

Palombo, Marco et al. (2020), « SANDI: A compartment-based model for non-invasive apparent soma and neurite imaging by diffusion MRI », *in*: *NeuroImage* 215, p. 116835, ISSN: 1053-8119, DOI: https://doi.org/10.1016/j.neuroimage.2020.116835, URL: https://www.sciencedirect.com/science/article/pii/S1053811920303220.

Panagiotaki, Eleftheria et al. (2012), « Compartment models of the diffusion MR signal in brain white matter: A taxonomy and comparison », *in*: *NeuroImage* 59.*3*, pp. 2241–2254, ISSN: 1053-8119, DOI: https://doi.org/10.1016/j.neuroimage.2011.09.081, URL: https://www.sciencedirect.com/science/article/pii/S1053811911011566.

Parker, Geoffrey J.M., Hamied A. Haroon, and Claudia A.M. Wheeler-Kingshott (2003), « A framework for a streamline-based probabilistic index of connectivity (PICo) using a structural interpretation of MRI diffusion measurements », *in*: *Journal of Magnetic Resonance Imaging* 18.*2*, pp. 242–254, DOI: https://doi.org/10.1002/jmri.10350, eprint: https://onlinelibrary.wiley.com/doi/pdf/10.1002/jmri.10350, URL: https://onlinelibrary.wiley.com/doi/abs/10.1002/jmri.10350.

Pestilli, Franco et al. (Aug. 2014), « LiFE: Linear Fascicle Evaluation a new technology to study visual connectomes », *in*: vol. 14, pp. 1122–1122, DOI: 10.1167/14.10.1122.

Pizzolato, Marco et al. (2020), « Acquiring and Predicting Multidimensional Diffusion (MUDI) Data: An Open Challenge », *in*: *Computational Diffusion MRI*, ed. by Elisenda Bonet-Carne et al., Cham: Springer International Publishing, pp. 195–208, ISBN: 978-3-030-52893-5.

Planchuelo-Gómez, Álvaro et al. (2024), « Optimisation of quantitative brain diffusion-relaxation MRI acquisition protocols with physics-informed machine learning », *in*: *Medical Image Analysis* 94, p. 103134, ISSN: 1361-8415, DOI: https://doi.org/10.1016/j.media.2024.103134, URL: https://www.sciencedirect.com/science/article/pii/S1361841524000598.

Poirier, Charles and Maxime Descoteaux (2024), « A unified filtering method for estimating asymmetric orientation distribution functions », *in*: *NeuroImage* 287, p. 120516,

ISSN: 1053-8119, DOI: https://doi.org/10.1016/j.neuroimage.2024.120516, URL: https://www.sciencedirect.com/science/article/pii/S1053811924000119.

Poupon, C. et al. (2001), « Towards inference of human brain connectivity from MR diffusion tensor data », *in*: *Medical Image Analysis* 5.*1*, pp. 1–15, ISSN: 1361-8415, DOI: https://doi.org/10.1016/S1361-8415(00)00030-X, URL: https://www.sciencedirect.com/science/article/pii/S136184150000030X.

Rafael-Patino, Jonathan et al. (2020), « Robust Monte-Carlo Simulations in Diffusion-MRI: Effect of the Substrate Complexity and Parameter Choice on the Reproducibility of Results », *in*: *Frontiers in Neuroinformatics* Volume 14 - 2020, ISSN: 1662-5196, DOI: 10.3389/fninf.2020.00008, URL: https://www.frontiersin.org/journals/neuroinformatics/articles/10.3389/fninf.2020.00008.

Rensonnet, Gaëtan et al. (2019), « Towards microstructure fingerprinting: Estimation of tissue properties from a dictionary of Monte Carlo diffusion MRI simulations », *in*: *NeuroImage* 184, pp. 964–980, ISSN: 1053-8119, DOI: https://doi.org/10.1016/j.neuroimage.2018.09.076, URL: https://www.sciencedirect.com/science/article/pii/S1053811918319487.

Rheault, Francois et al. (2019), « Bundle-specific tractography with incorporated anatomical and orientational priors », *in*: *Neuroimage* 186, pp. 382–398.

Scherrer, Benoit et al. (2016), « Characterizing brain tissue by assessment of the distribution of anisotropic microstructural environments in diffusion-compartment imaging (DIAMOND) », *in*: *Magnetic Resonance in Medicine* 76.*3*, pp. 963–977, DOI: https://doi.org/10.1002/mrm.25912, eprint: https://onlinelibrary.wiley.com/doi/pdf/10.1002/mrm.25912, URL: https://onlinelibrary.wiley.com/doi/abs/10.1002/mrm.25912.

Schiavi, Simona et al. (2020), « A new method for accurate in vivo mapping of human brain connections using microstructural and anatomical information », *in*: *Science Advances* 6.*31*, eaba8245, DOI: 10.1126/sciadv.aba8245, eprint: https://www.science.org/doi/pdf/10.1126/sciadv.aba8245, URL: https://www.science.org/doi/abs/10.1126/sciadv.aba8245.

Sjölund, Jens et al. (2015), « Constrained optimization of gradient waveforms for generalized diffusion encoding », *in*: *Journal of Magnetic Resonance* 261, pp. 157–168, ISSN: 1090-7807, DOI: https://doi.org/10.1016/j.jmr.2015.10.012, URL: https://www.sciencedirect.com/science/article/pii/S1090780715002451.

Smith, Robert E. et al. (2013), « SIFT: Spherical-deconvolution informed filtering of tractograms », *in*: *NeuroImage* 67, pp. 298–312, ISSN: 1053-8119, DOI: https://doi.org/10.1016/j.neuroimage.2012.11.049, URL: https://www.sciencedirect.com/science/article/pii/S1053811912011615.

— (2015), « SIFT2: Enabling dense quantitative assessment of brain white matter connectivity using streamlines tractography », *in*: *NeuroImage* 119, pp. 338–351, ISSN: 1053-8119, DOI: https://doi.org/10.1016/j.neuroimage.2015.06.092, URL: https://www.sciencedirect.com/science/article/pii/S1053811915005972.

Stejskal, E. O. and J. E. Tanner (Jan. 1965), « Spin Diffusion Measurements: Spin Echoes in the Presence of a Time-Dependent Field Gradient », *in*: *The Journal of Chemical Physics* 42.*1*, pp. 288–292, ISSN: 0021-9606, DOI: 10.1063/1.1695690, eprint: https://pubs.aip.org/aip/jcp/article-pdf/42/1/288/18837047/288_1_online.pdf, URL: https://doi.org/10.1063/1.1695690.

Szczepankiewicz, Filip, Samo Lasič, et al. (2015), « Quantification of microscopic diffusion anisotropy disentangles effects of orientation dispersion from microstructure: Applications in healthy volunteers and in brain tumors », *in*: *NeuroImage* 104, pp. 241–252, ISSN: 1053-8119, DOI: https://doi.org/10.1016/j.neuroimage.2014.09.057, URL: https://www.sciencedirect.com/science/article/pii/S105381191400799X.

Szczepankiewicz, Filip and Jens Sjölund (2021), « Cross-term-compensated gradient waveform design for tensor-valued diffusion MRI », *in*: *Journal of Magnetic Resonance* 328, p. 106991, ISSN: 1090-7807, DOI: https://doi.org/10.1016/j.jmr.2021.106991, URL: https://www.sciencedirect.com/science/article/pii/S109078072100080X.

Tax, Chantal M. W. et al. (July 2014), « Evaluating Contextual Processing in Diffusion MRI: Application to Optic Radiation Reconstruction for Epilepsy Surgery », *in*: *PLOS ONE* 9.*7*, pp. 1–19, DOI: 10.1371/journal.pone.0101524, URL: https://doi.org/10.1371/journal.pone.0101524.

Tax, Chantal M.W. et al. (2022), « What's new and what's next in diffusion MRI preprocessing », *in*: *NeuroImage* 249, p. 118830, ISSN: 1053-8119, DOI: https://doi.org/10.1016/j.neuroimage.2021.118830, URL: https://www.sciencedirect.com/science/article/pii/S1053811921011010.

Topgaard, Daniel (2017), « Multidimensional diffusion MRI », *in*: *Journal of Magnetic Resonance* 275, pp. 98–113, ISSN: 1090-7807, DOI: https://doi.org/10.1016/j.jmr.2016.12.007, URL: https://www.sciencedirect.com/science/article/pii/S1090780716302701.

— (Aug. 2020), *Advanced Diffusion Encoding Methods in MRI*, The Royal Society of Chemistry, ISBN: 978-1-78801-726-8, DOI: 10.1039/9781788019910, URL: https://doi.org/10.1039/9781788019910.

Torrey, H. C. (Nov. 1956), « Bloch Equations with Diffusion Terms », *in*: *Phys. Rev.* 104 (3), pp. 563–565, DOI: 10.1103/PhysRev.104.563, URL: https://link.aps.org/doi/10.1103/PhysRev.104.563.

Tournier, J-Donald, Fernando Calamante, and Alan Connelly (2007), « Robust determination of the fibre orientation distribution in diffusion MRI: Non-negativity constrained super-resolved spherical deconvolution », *in*: *NeuroImage* 35.*4*, pp. 1459–1472, ISSN: 1053-8119, DOI: https://doi.org/10.1016/j.neuroimage.2007.02.016, URL: https://www.sciencedirect.com/science/article/pii/S1053811907001243.

Truffet, Raphaël, Christian Barillot, and Emmanuel Caruyer (May 2019), « Optimal selection of diffusion-weighting gradient waveforms using compressed sensing and dictionary learning », *in*: *ISMRM 2019 - 27th Annual Meeting & Exhibition*, Montréal, Canada, pp. 1–3, URL: https://inserm.hal.science/inserm-02015394.

Truffet, Raphaël, Jonathan Rafael-Patino, et al. (Oct. 2020), « An evolutionary framework for microstructure-sensitive generalized diffusion gradient waveforms », *in*: *MICCAI 2020 - 23rd International Conference on Medical Image Computing and Computer Assisted Intervention*.

Tuch, David S. (2004), « Q-ball imaging », *in*: *Magnetic Resonance in Medicine* 52.*6*, pp. 1358–1372, DOI: https://doi.org/10.1002/mrm.20279, eprint: https://onlinelibrary.wiley.com/doi/pdf/10.1002/mrm.20279, URL: https://onlinelibrary.wiley.com/doi/abs/10.1002/mrm.20279.

Tuch, David S. et al. (2003), « Diffusion MRI of Complex Neural Architecture », *in*: *Neuron* 40.*5*, pp. 885–895, ISSN: 0896-6273, DOI: https://doi.org/10.1016/S0896-6273(03)00758-X, URL: https://www.sciencedirect.com/science/article/pii/S089662730300758X.

Villarreal-Haro, Juan Luis et al. (2023), « CACTUS: a computational framework for generating realistic white matter microstructure substrates », *in*: *Frontiers in Neuroinformatics* Volume 17 - 2023, ISSN: 1662-5196, DOI: 10.3389/fninf.2023.1208073, URL: https://www.frontiersin.org/journals/neuroinformatics/articles/10.3389/fninf.2023.1208073.

Wasserthal, Jakob, Peter F Neher, and Klaus H Maier-Hein (2018), « Tract orientation mapping for bundle-specific tractography », *in*: *International conference on medical image computing and computer-assisted intervention*, Springer, pp. 36–44.

Wedeen, Van J. et al. (2005), « Mapping complex tissue architecture with diffusion spectrum magnetic resonance imaging », *in*: *Magnetic Resonance in Medicine* 54.*6*, pp. 1377–1386, DOI: https://doi.org/10.1002/mrm.20642, eprint: https://onlinelibrary.wiley.com/doi/pdf/10.1002/mrm.20642, URL: https://onlinelibrary.wiley.com/doi/abs/10.1002/mrm.20642.

Westin, C.F., O. Pasternak, and H. Knutsson (2012), « Rotationally invariant gradient schemes for diffusion MRI. », *in*: *Proceedings of the ISMRM Annual Meeting (ISMRM 12')*.

Westin, Carl-Fredrik, Hans Knutsson, et al. (2016), « Q-space trajectory imaging for multidimensional diffusion MRI of the human brain », *in*: *NeuroImage* 135, pp. 345–362, ISSN: 1053-8119, DOI: https://doi.org/10.1016/j.neuroimage.2016.02.039, URL: https://www.sciencedirect.com/science/article/pii/S1053811916001488.

Westin, Carl-Fredrik, Filip Szczepankiewicz, et al. (2014), « Measurement Tensors in Diffusion MRI: Generalizing the Concept of Diffusion Encoding », *in*: *Medical Image Computing and Computer-Assisted Intervention – MICCAI 2014*, ed. by Polina Golland et al., Cham: Springer International Publishing, pp. 209–216, ISBN: 978-3-319-10443-0.

Willis, Thomas (1664), *Cerebri anatome: cui accessit nervorum descriptio et usus*.

Zhang, Hui et al. (2012), « NODDI: Practical in vivo neurite orientation dispersion and density imaging of the human brain », *in*: *NeuroImage* 61.*4*, pp. 1000–1016, ISSN: 1053-8119, DOI: https://doi.org/10.1016/j.neuroimage.2012.03.072, URL: https://www.sciencedirect.com/science/article/pii/S1053811912003539.

COLLEGE DOCTORAL BRETAGNE
MATHS, TELECOMS
INFORMATIQUE, SIGNAL
SYSTEMES, ELECTRONIQUE

Université de Rennes

Titre : Optimisation des paramètres d'acquisition en IRM de diffusion pour la reconstruction de la connectivité cérébrale

Mot clés : IRM de diffusion, Microstructure, Acquisition, Optimisation, Matière blanche, Tractographie

Résumé : L'IRM de diffusion est une méthode non invasive pour sonder la microstructure des tissus, en mesurant le déplacement des molécules d'eau. Toutefois, les informations extraites du signal dépendent fortement du schéma d'acquisition. Ce dernier doit trouver un équilibre entre la sensibilité aux caractéristiques de la microstructure et les contraintes pratiques telles que le temps d'acquisition et la qualité du signal. Cette thèse porte sur l'optimisation du protocole d'acquisition en IRM de diffusion, plus précisément dans le cadre d'acquisitions multidimensionnelles, où l'acquisition est encodée à l'aide de b-tenseurs. La principale contribution de ce travail est le développement d'un cadre adapté à la conception de protocoles d'acquisition maximisant la sensibilité aux paramètres d'intérêt. Une seconde contribution vise à comprendre la signification physique pour la microstructure d'un paramètre d'intérêt du modèle. Enfin, la génération de fantômes plus adaptés à l'estimation des effets de l'acquisition par b-tenseurs sur la tractographie par filtrage a été initiée.

Title: Optimization of diffusion MRI acquisition parameters for brain connectivity reconstruction

Keywords: Diffusion MRI, Microstructure, Acquisition, Optimization, White matter, Tractography

Abstract: Diffusion MRI is a non-invasive method for probing tissue microstructure by measuring the displacement of water molecules. However, the information extracted from the signal strongly depends on the acquisition scheme. The latter must strike a balance between sensitivity to microstructural features and practical constraints such as acquisition time and signal quality. This thesis focuses on optimizing the acquisition protocol in diffusion MRI, more specifically within the framework of multidimensional acquisitions, where encoding is performed using b-tensors. The main contribution of this work is the development of a framework tailored to designing acquisition protocols that maximize sensitivity to parameters of interest. A second contribution aims to better understand the physical meaning, in terms of microstructure, of one of the model's parameters of interest. Finally, the generation of phantoms better suited to estimating the effects of b-tensor encoding on tractography filtering has been initiated.